Politecnico di Milano

Facoltà di Ingegneria Industriale
Corso di Laurea Magistrale in Ingegneria Aeronautica

Direct numerical simulation of turbulent channel flow over porous walls

Relatore: Prof. Maurizio Quadrio
Correlatore: Prof. Luca Cortelezzi

Tesi di laurea di:
Marco Edoardo Rosti
Matr. 765760

Anno Accademico 2011 - 2012

Ringraziamenti

Desidero ringraziare profondamente il mio relatore Prof. Maurizio Quadrio e il mio correlatore Prof. Luca Cortelezzi, per avermi seguito in questa tesi e per la loro disponibilità e cordialità. Inoltre ringrazio la McGill University che, su richiesta del Prof. Luca Cortelezzi, mi ha fornito le risorse di calcolo necessarie per svolgere questa ricerca.

Un ringraziamento speciale va a tutta la mia famiglia. A mia mamma, che mi ha sempre consigliato e supportato fin da piccolo, a mio papà, per avermi dato un modello di rigore da seguire, a mia sorella Cristina, con cui ho condiviso tutta la mia vita fino a questo momento.

Un ringraziamento va poi a tutti i miei amici, a Giorgio, Riccardo e Lorenzo, che conosco dai tempi del liceo, e a Luca, che frequento da qualche anno. Infine ringrazio i miei compagni di università, con cui ho condiviso questa percorso, in particolare Michele, Davide, Federico, Leonardo, Luca, Domenico, Luca P. e Daniele.

Contents

List of Figures

List of Tables

Abstract

We perform a direct numerical simulation (DNS) of a turbulent channel flow over porous walls. In the fluid region the flow is governed by the Navier-Stokes equations, while in the porous layers is governed by the Volume-Averaged Navier-Stokes equations derived by Whitaker [54, 55, 56]. The latter equations are obtained by volume-averaging the microscopic flow field over a small volume, in order to model a macroscopic, or volume-averaged, flow field. The volume-averaging technique allows to treat the porous medium as a continuum. To formulate numerically this problem, we derive and implement the v-η formulation of the Navier-Stokes and Volume-Averaged Navier-Stokes equations. At the interface between the porous layers and the fluid region, we impose the momentum transfer conditions proposed by Ochoa-Tapia and Whitaker [31, 32, 33]. The DNS solver used to integrate the coupled evolution equations is a substantial extension of an existing solver [26]. Our solver uses a Fourier discretization in the streamwise and spanwise directions, and a compact, explicit high-order, finite difference discretization in the wall-normal direction. Time integration is performed using a semi-implicit method, where the nonlinear terms are advanced with a third-order Runge-Kutta scheme, whereas the other terms are advanced using an implicit second-order Crank-Nicholson scheme. We perform extensive DNSs at two Reynolds numbers: a very low Reynolds number, $\mathrm{Re}_\tau = 65$ and an intermediate one, $\mathrm{Re}_\tau = 200$. For both turbulent flows we analyze the turbulence statistics and the flow fields. For the intermediate case, at $\mathrm{Re}_\tau = 200$, we perform a parametric study, where we vary the height of the porous layers and the coefficient of the momentum transfer conditions. The results are compared with the DNS of a turbulent channel flow over impermeable walls. For the very low Reynolds number, $\mathrm{Re}_\tau = 200$, we investigate if the porous wall can sustain turbulent flows.

Key Words

Direct Numerical Simulation - Turbulence - Porosity - Permeability - Volume-Averaged Navier-Stokes equations

Sommario

Svolgiamo una simulazione numerica diretta (DNS) di un flusso turbolento in un canale piano con pareti porose. Nella regione di fluido il flusso è governato dalle equazioni di Navier-Stokes, mentre negli strati porosi è governato dalle equazioni di Navier-Stokes mediate sul volume, derivate da Whitaker [54, 55, 56]. Queste equazioni sono ottenute mediando il campo di moto microscopico su un piccolo volume, in modo da modellare il campo di moto macroscopico, o mediato sul volume. Questa tecnica permette inoltre di poter considerare il mezzo poroso come un continuo. Per formulare numericamente il problema, deriviamo e implementiamo la formulazione v-η delle equazioni di Navier-Stokes e delle equazioni di Navier-Stokes mediate sul volume. All'interfaccia tra lo strato poroso e la regione di fluido, imponiamo delle condizioni che accoppiano i due flussi e che assicurano che gli scambi di massa e quantità di moto siano corretti [31, 32, 33]. Il solutore DNS usato per integrare le equazioni è un ampliamento sostanziale di un solutore già esistente [26]. Questo usa una discretizzazione di Fourier nelle direzioni assiale e trasversale, e una discretizzazione con differenze finite compatte di alto ordine in direzione normale alla parete. L'integrazione nel tempo è effettuata con uno schema semi-implicito, in cui i termini non lineari sono avanzati con lo schema di Runge-Kutta del terzo ordine, mentre gli altri termini sono avanzati con lo schema implicito di Cranck-Nicholson. Simuliamo flussi a due differenti numeri di Reynolds: uno molto basso $\mathrm{Re}_\tau = 65$ e uno intermedio $\mathrm{Re}_\tau = 200$. Per il caso a $\mathrm{Re}_\tau = 200$ svolgiamo uno studio parametrico in cui variamo l'altezza dello strato poroso e il coefficiente che regola gli scambi di quantità di moto all'interfaccia. I risultati sono confrontati con quelli di una DNS di un flusso turbolento su pareti impermeabili. Per il caso a $\mathrm{Re}_\tau = 65$ vogliamo scoprire se la parete porosa sia in grado di sostenere un flusso turbolento.

Parole chiave

Simulazione numerica diretta - Turbolenza - Porosità - Permeabilità -
Equazione di Navier-Stokes mediate sul volume

Estratto della tesi in lingua italiana

Questa ricerca è motivata dalle molte applicazioni presenti e future che coinvolgono flussi attraverso o su materiali porosi, permeabili e traspiranti. Esempi di applicazioni ingegneristiche in cui sono sfruttati i materiali porosi sono l'estrazione di petrolio dai giacimenti e il filtraggio di inquinanti attraverso le falde acquifere. A livello industriale i materiali porosi sono usati nei sistemi di raffreddamento, in cui viene sfruttata la porosità per aumetare gli scambi termici, nei processi di filtraggio, in cui si vogliono separare particelle solide dai fluidi. Inoltre pareti traspiranti sono spesso usate nei sistemi di controllo di flussi turbolenti. Nel campo bio-medico troviamo coinvolti i materiali porosi nei meccanismi di scambio tra sangue, aria e tessuti in diversi organi, come i reni e i polmoni.

Si è soliti pensare che un flusso su pareti porose senta una resistenza e intensità del livello di turbolenza vicino alla parete maggiori rispetto allo stesso flusso su una superficie impermeabile. Tilton e Cortelezzi [49, 50] hanno studiato la stabilità lineare di un flusso piano su pareti porose e hanno mostrato l'effetto destabilizzante della permeabilità, che abbassa il numero di Reynolds critico. Il loro risultato ha ulteriormente ribadito il potenziale di tali materiali in applicazioni che coinvolgono la stabilità del flusso e la sua transizione al regime turbolento, sui meccanismi utilizzati per ridurre od aumentare la resistenza e sui sistemi che controllano le proprietà di mescolamento del flusso.

In questa tesi vogliamo studiare numericamente il flusso turbolento in un canale delimitato da strati porosi piani, omogenei e isotropi. Lo simulazione accurata di flussi turbolenti è complicata dal grande numero di scale temporali e spaziali coinvolte. Nel corso degli anni per simulare numericamente questi flussi sono state sviluppate diverse tecniche, con diversi livelli di approssimazione. La tecnica che noi utilizziamo è la DNS (Direct Numerical Simulation), utilizzata per la prima volta da Kim, Moin and Moser [19]. Nelle DNS si risolvono direttamente le equazioni di Navier-Stokes, con condizioni iniziali e condizioni al contorno appropriate, risolvendo tutte le scale della turbolenza. Questo approccio è stato impraticabile per molti anni perchè richiede ingenti risorse di calcolo. Oggi le DNS sono diventate uno strumento molto utile per lo studio di flussi turbolenti [28], anche se si è in grado di effetuarle solo su geometrie semplici, come i flussi in canali piani, flussi in condotti a sezione circolare e strati limiti.

La DNS di flussi turbolenti su pareti porose è stata effettuata raramente a causa della difficoltà di modellare la parete porosa. Nel corso degli anni sono stati usati diversi modelli. Un primo modo è stato quello di ridurre tutto l'effetto dello strato poroso ad una opportuna condizione al contorno, con lo scopo di non dover simulare il flusso all'interno dello strato poroso. Questa tecnica è stata utilizzata da Hahn, Je e Choi [15] e da Wagner e Friedrich [53]. Tuttavia per poter studiare con più precisione gli scambi di massa e quantità di moto tra lo strato poroso e la regione di fluido, bisogna modellare anche il flusso in tutto lo strato poroso.

Si può pensare di risolvere le equazioni di Navier-Stokes in tutto il campo di moto, applicando le condizioni al contorno di non penetrabilità e di non slittamento su tutte le superfici solide. Però i materiali porosi hanno una struttura interna molto complessa e che spesso non è nemmeno nota, quindi l'imposizione delle condizioni al contorno risulta molto ardua. Tale tecnica si può usare per materiali porosi che hanno una geometria molto semplice, come cilindri o sfere impachettate. Ad esempio Prosperetti *et al.* ha modellato lo strato poroso con dei cilindri [59] e con delle sfere [25], mentre Breugem, Boersma *et al.* [6, 7, 8, 9] lo hanno modellato con dei cubi. I loro risultati hanno mostrato che la permeabilità causa un considerevole aumento della resistenza e della produzione degli sforzi di Reynolds.

Per riuscire a descrivere il flusso attraverso materiali porosi più complessi, si è spesso costretti a utilizzare una tecnica in cui il materiale poroso viene trattato come un continuo. In questo metodo si risolvono le equazioni di Navier-Stokes nella regione di fluido e le equazioni di Navier-Stokes mediate sul volume (Volume-Averaged Navier-Stokes equations), derivate da Whitaker [54, 55, 56], nello strato poroso. Queste equazioni sono ottenute mediando il campo di moto microscopico su un piccolo volume, in modo da modellare il campo di moto macroscopico, o mediato sul volume. A seguito del processo di media sul volume queste equazioni contengono nuovi termini, quali il termine di Darcy, che rappresenta una resistenza viscosa, e il termine di Forchheimer, che coinvolge un tensore del secondo ordine ed esprime la resistenza dovuta ad effetti inerziali. Questo tensore dipende dalla struttura interna del mezzo poroso. In una piccola regione di transizione vicina all'interfaccia con lo strato di fluido, l'uso delle equazioni di Navier-Stokes mediate sul volumo non è corretto, ma l'errore si può rimuovere tramite l'utilizzo di condizioni che assicurano il giusto scambio di quantità di moto. Se si trascurano gli effetti inerziali, queste condizioni assumono una forma piuttosto semplice ed inoltre il termine di Forhheimer delle equazioni si può trascurare. Ciò vale per materiali porosi con piccola permeabilità, in cui le velocità nello strato porose sono piccole rispetto a quelle caratteristiche del canale. Esempi di lavori che hanno usato questo approccio sono [45, 58, 10, 11].

In questa tesi effettuiamo una DNS di flusso turbolento in un canale piano su pareti porose. Le equazioni di Navier-Stokes sono risolte nella regione di fluido, mentre la loro versione mediata sul volume viene risolta negli strati porosi. Alle interfaccie accoppiamo i flussi con le condizioni al contorno di trasferimento di quantità di moto. Il solutore DNS è un'estensione di uno esistente per flussi su pareti impermeabili [26] e usa una discretizzazione di Fourier nelle direzioni assiale e trasversale, che sono direzioni omogenee, e delle differenze finite in direzione normale alla parete. L'integrazione nel tempo viene effettuato con un metodo semi implicito, in cui i termini non lineari delle equazioni sono avanzati con lo schema Runge-Kutta del terzo ordine, mentre gli altri termini sono avanzati con lo schema di Cranck-Nicholson.

Abbiamo analizzato due casi a numeri di Reynolds differenti, pari a $\mathrm{Re}_\tau = 200$ e $\mathrm{Re}_\tau = 65$. Il primo numero di Reynolds è scelto con lo scopo di studiare come lo strato poroso modifichi il flusso turbolento in un canale piano, mentre con il secondo numero di Reynolds vogliamo scoprire se la parete porosa sia in grado di sostenere un flusso turbolento. Dalla simulazione a $\mathrm{Re}_\tau = 200$ osserviamo che lo strato poroso modifica le statistiche del flusso turbolento. In particolare la velocità media viene modificata dalla presenza di una velocità di slittamento e dall'aumento della derivata del profilo medio all'interfaccia, causando anche un aumento della velocità d'attrito. Anche gli sforzi di Reynolds e le velocità rms vengono modificate, specialmente all'interfaccia dove non sono nulle; all'interno del canale le loro componenti trasversali e normali alla parete sono incrementate, mentre quelle in direzione assiale vengono ridotte. Tramite uno studio parametrico in cui variamo l'altezza degli strati porosi e il coefficiente della condizione al contorno che domina gli scambi di quantità di moto, vogliamo vedere se questi parametri hanno effetto sul flusso turbolento. Mentre le differenze al variare dell'altezza degli strati porosi sono limitate, al variare del coefficiente all'interfaccia si ottengono grandi variazioni. A $\mathrm{Re}_\tau = 65$ si riesce a ottenere un flusso turbolento e si scopre che la parete porosa è in grado di sostenerlo. Il profilo medio di tale flusso sembra non avere una regione logaritmica, mentre le velocità rms sono profondamente differenti, specialmente quelle in direzione trasversale e normale alla parete.

In questa ricerca abbiamo considerato flussi turbolenti su pareti porose con bassa permeabilità, scoprendo che queste modificano le statistiche del flusso turbolento. Questi risultati possono avere implicazioni sulla ricerca che si occupa di sistemi di controllo del flusso tramite pareti traspiranti. Infatti il modello di materiale poroso usato può essere impiegato come primo passo per un modello più realistico di parete traspirante, usato ad esempio per inibire la transizione alla turbolenza negli strati limiti asintotici. Questi vengono generalemente simulati sperimentalmente usando fori discreti o materiali porosi. Mentre i primi hanno il vantaggio che la superficie può svolgere ancora dei compiti strutturali, i secondi sono di più facile realizzazione e inoltre non generano effetti tridimensionali che possono accelerare la transizione.

Dopo la nostra simulazione a numero di Reynolds molto basso, lavori futuri dovrebbero investigare meglio i meccanismi che sono in grado di sostenere un flusso turbolento a questi numeri di Reynolds, cercando inoltre di scoprire eventuali flussi in cui si alternano il regime turbolento e laminare.

Nel nostro lavoro abbiamo usato una versione semplificata delle equazioni di

Navier-Stokes mediate sul volume e della condizione di interfaccia, in cui non abbiamo tenuto conto degli effetti inerziali. Infatti quando questi sono trascurabili, il termine di resistenza di Forchheimer viene trascuarato. Mentre la resistenza di Forchheimer è spesso trascurabile all'interno dello strato poroso, gli effetti inerziali potrebbero essere ancora importanti all'interfaccia. L'ipotesi di trascurare gli effetti inerziali limita il valore di permeabilità che si può considerare. Un possibile sviluppo futuro, può quindi essere quello di provare a modificare le equazioni e le condizioni all'interfaccia per tenere conto di questi effetti.

Chapter 1

Introduction

This work is the result of a collaboration between myself Mr. Marco Rosti, Mr. Davide Scarselli, Professor Maurizio Quadrio of the Politecnico di Milano and Professor Luca Cortelezzi of McGill University, who visited the Politecnico di Milano during a sabbatical leave.

This research is motivated by the many present and future engineering applications which involve fluid flows over or through porous materials, which are permeable and transpirating. Examples in nature are flows through sedimentary rocks, such as sandstones, conglomerates and shales, and water flows over seabeds and riverbeds. Extraction of oil from ground reservoirs, management of water ground basins and filtration of pollutants through aquifers, are examples of engineering applications which involves porous media and the fluid motion through them. Moreover, industrial applications which use porous media are, for example, transpiration cooling, in which the porosity is used to enhance the heat exchange capability of the material; filtration processes used to separate solid particles from fluids; use of wall transpiration for flow control and transition delay. In bio-mechanics, porous media are involved in fluid and mass transfer at the walls of many organic tissues, such as blood vessels, lungs and kidneys.

In general, it is assumed that a flow over a porous wall experiences higher drag and turbulent intensities near the wall than the same flow over a flat impermeable surface. Tilton and Cortelezzi [49, 50] investigated the stability of channel flows over porous walls, and they showed that wall permeability has a destabilizing effect, lowering the critical Reynolds number. This result indicates the potential of porous materials in applications involving transition and turbulence, such as flow control, drag reduction and enhancement, transition triggering and delaying, and amplifying mixing properties of turbulent flows.

In this thesis, we study numerically the turbulent flow of an incompressible fluid through a channel delimited by flat, homogeneous, isotropic porous layers. First, we investigate how a porous layer affects the turbulence statistics of a channel flow at moderate Reynolds numbers. Then, we characterize the effects of varying the height of the porous layer and of the momentum transfer coefficient on the turbulent flow. Finally, leveraging the destabilizing effect of wall permeability, we obtain and study a turbulent channel flow at very low Reynolds numbers.

The accurate simulation of turbulent flows is challenging because involves resolving a wide range of lengths and time scales, and predicting its chaotic behaviour. Over the years, different techniques with different levels of approximation have been developed to study turbulent flows. For example, Reynolds Averaged Navier-Stokes (RANS) solve the evolution of the average turbulent flow, while Large Eddy Simulations (LES) compute only the large scales of the turbulent flow. On the one hand, these methods suffer from the lack of closure because the evolution equations contain terms that require modeling [35, 57, 23], on the other hand, RANS and LES allow the simulation of turbulent flows in the complex geometries of interest to industry. It is possible, however, to simulate accurately turbulent flows in simple geometries using a recent technique called Direct Numerical Simulations (DNS). DNSs solve the Navier-Stokes equations, with appropriate initial and boundary conditions, resolving all the scales of motion.

DNSs were infeasible until computers of sufficient power became available. Kim, Moin and Moser [19] performed one of the first DNS, for a fully developed, turbulent, channel flow at moderate Reynolds numbers. They proposed to use the v-η formulation of the Navier-Stokes equations. Many DNS of turbulent flows in planar geometries employ this formulation. Nowadays, the DNS for incompressible, low Reynolds number, turbulent flows with geometrically simple boundaries has become a valuable tool for fundamental turbulence research [28]. Currently, DNS are used to study turbulent plane channel flows, pipe flows, boundary layers and flows in ducts with anular cross-section.

The DNS of turbulent channel flows over porous walls has been rarely attempted because of the difficulty of modeling the porous walls. A few models have been implemented over the years. In the first method, the effects of a porous wall are simulated using a suitable boundary condition at the interface between the porous layer and the fluid region. The advantage of this method is that the flow inside the porous layers is not needed. Hahn *et al.* [15] performed a DNS of a turbulent channel flow using this approach. At the porous wall, they use a boundary condition which is an extension of the condition proposed by Beavers and Joseph [3]. The condition allows slip velocities for the wall-tangent components of the velocity, and a zero wall-normal velocity component. Wagner and Friedrich [53] simulated a turbulent pipe flow over permeable walls using a different boundary conditions. They imposed a permeability condition for the radial velocity component, and the no-slip condition for the other two velocity components.

In order to describe more accurately the mass and momentum transfer between the porous layer and the fluid region, we have to model the flow through the entire porous medium. In general, porous media have a very complex structure, which is not known in full details. Inside the porous layers, one can envision to solve directly the Navier-Stokes equations, imposing the no-slip and no-penetration conditions at each solid surface. However, this is hard to implement in general because of the complexity of the geometry of the boundaries. Therefore, this approach can be used for porous materials of very simple geometry, such as packed cylinders or spheres. For example, Prosperetti *et al.* modelled the porous media with cylinders [59] and with spheres [25]. They solved the Stokes layers near the solid surfaces of the cylinders and spheres that compose the porous material, and the Navier-Stokes equations everywhere else, and they studied the lift, drag and torque applied to a cylindrical and spherical particle by the flow. Breugem and Boersma [6, 7], and Breugem *et al.* [8, 9], have performed DNSs of channel flow over porous walls, modelling the porous layers with a grid of cubes. They showed that wall permeability causes a considerable increase in the total drag and in the production of all the Reynolds stresses. This approach is computationally costly, and it is limited by the scarce applicability of these types of porous materials.

Flows through porous media with a complex structure can be studied by treating the porous medium as a continuum. In this method, the Navier-Stokes equations are solved in the fluid region, and the Volume-Averaged Navier-Stokes, first derived by Whitaker *et al.* [54, 55, 56], are solved in the porous layers. The latter equations are obtained by volume-averaging the microscopic flow field over a small volume, in order to obtain a macroscopic, or volume-averaged, flow field. The volume-averged equations contain new terms, such as the Darcy term, which represents a volume-averaged viscous drag, and the Forchheimer term, which involves a second-order tensor accounting for the drag due to inertial effects. The exact form of this tensor depends on the geometrical structure of the porous medium.

The flow at the interface between the fluid region and the porous material is especially difficult to model. In fact, in a small transition layer adjacent to the interface with the channel region, the Brinkman layer [3], the structure of a porous medium undergoes rapid changes and the use of the Volume-Averaged Navier-Stokes equations is incorrect. Ochoa-Tapia and Whitaker [31, 32, 33] have derived a momentum transfer condition, which correct the error by introducing a jump in the shear stresses at the interface. When inertial effects can be neglected in the porous regions, the interface conditions become simpler and the convective and Forcheimer terms drop from the evolution equations governing the flow in the porous layer. This assumption is valid for porous media of small permeability in which the flow velocities in the porous layer are small with respect to the characteristic velocity in the channel region. Examples of numerical simulations which use this approach are [45, 58, 10, 11].

In this thesis, we perform a DNS of a turbulent channel flow over permeable walls. We solve the Navier-Stokes equations in the the fluid region coupled with the Volume-Averaged Navier-Stokes in the porous layers. At the interface between the fluid region and the porous layer we impose the momentum transfer conditions. Since we neglect the inertial effects in the porous layers, we thus limit our study to permeabilities for which the velocity at the interface is much smaller ($\approx 5\%$) than the mean flow. To solve numerically this problem, we substantially extended an existing DNS solver [26]. We use a Fourier discretization in the streamwise and spanwise directions, and a compact, explicit high-order, finite difference discretization in the wall-normal direction. Time integration is performed using a semi-implicit method.

The outline of the thesis is as follows. In Chapter 2 we review the theory of flow through porous media. We present the main models that have been developed to describe such a complex flow. We also describe the conditions to be imposed at the interface between the fluid region and the porous medium. Chapter 3 presents the mathematical model of the flow over porous media. We make the problem non-dimensional and transform it in a more suitable form. In Chapter 4, we discuss the numerical discretization of the problem. Finally, in Chapter 5, we present some results of our simulations. In particular, we present two main cases: one at very low Reynolds number and one at intermediate Reynolds number.

As a consequence of the collaboration with Mr. Scarselli, my thesis shares two chapters with his thesis. In particular, the review of flow through porous media, performed in Chapter 2, and the definition of the mathematical model of the flow over porous media, presented in Chapter 3, are in common.

Chapter 2

Flow through porous media

This chapter succinctly reviews the theory of flow through porous media. The flow of an incompressible viscous fluid within the pore-like structure of a porous medium is governed by the Navier-Stokes equations

$$\frac{\partial \boldsymbol{u}}{\partial t} + \boldsymbol{\nabla} \cdot (\boldsymbol{u} \otimes \boldsymbol{u}) = -\frac{1}{\rho} \boldsymbol{\nabla} p + \nu \nabla^2 \boldsymbol{u}, \tag{2.1}$$

$$\boldsymbol{\nabla} \cdot \boldsymbol{u} = 0, \tag{2.2}$$

with no-slip and no-penetration boundary conditions on the solid surfaces and an appropriate initial condition, where $\boldsymbol{u}$ is the velocity, p the pressure, ρ the density and ν the kinematic viscosity of the fluid, respectively.

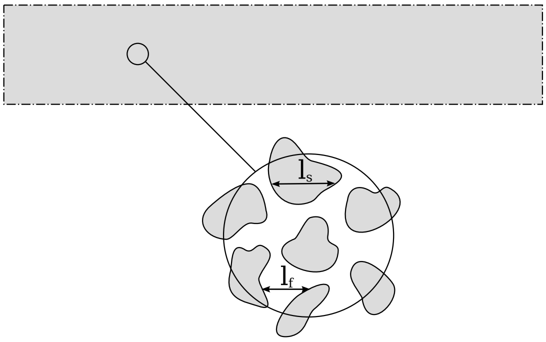

FIGURE 2.1: Sketch of a porous medium with a wide range of length scales. l_f and l_s are the pore and particle diameters of the pore-like structures.

In general, porous media have very complex structure which is not known in full details. Therefore, in most cases, the boundary conditions are nearly impossible to impose. Secondly, the flow inside a porous medium is characterized by a wide range of length scales, see figure 2.1. Porous media can be sponge-like porous foams and porous layers of packed particles. The smallest scales, l_f and l_s, represent the pore and particle diameters of the pore-like structures, while the largest scale is the characteristic macroscopic porous length L. These aspects make prohibitively difficult and costly a direct numerical simulation of flows in porous medium. Consequently, in order to study these kind of flows, different techniques have been proposed so far.

2.1 Darcy's law

One of the first studies on flow through porous media was published by Darcy in 1856 [12]; he investigated the flow of water filtering through a layer of sand, in connection with the fountains of the city of Dijon in France, as illustrated in figure 2.2. He concluded that, for creeping flows, the average flow rate passing through a layer of sand is proportional to the pressure gradient across the layer. Based on the result of his experiments, he proposed the following relation

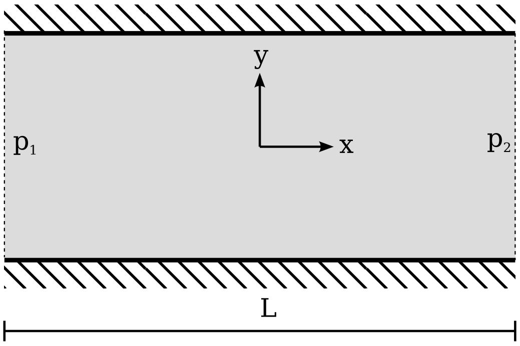

FIGURE 2.2: Filtration of water through a layer of sand.

$$Q = -kA\frac{p_2 - p_1}{\rho g L}, \tag{2.3}$$

where Q is the volumetric flow rate through the layer, A is the cross sectional area normal to the flow, g the gravitational acceleration, p_1 and p_2 the measured pressures, L the length of the sand layer over which the pressure difference is measured and k is the hydraulic conductivity. The previous equation was originally written as

$$Q = -kA\frac{\Delta H}{L}, \tag{2.4}$$

where ΔH is the hydraulic head. Figure 2.3 shows the Darcy velocity $u_D = Q/A$ versus $\Delta H/L$. Darcy's data clearly show the linearity between the average discharge rate of fluid and the pressure gradient.

The hydraulic conductivity depends on the kinematic viscosity ν [2]

$$k = \frac{gK}{\nu}, \tag{2.5}$$

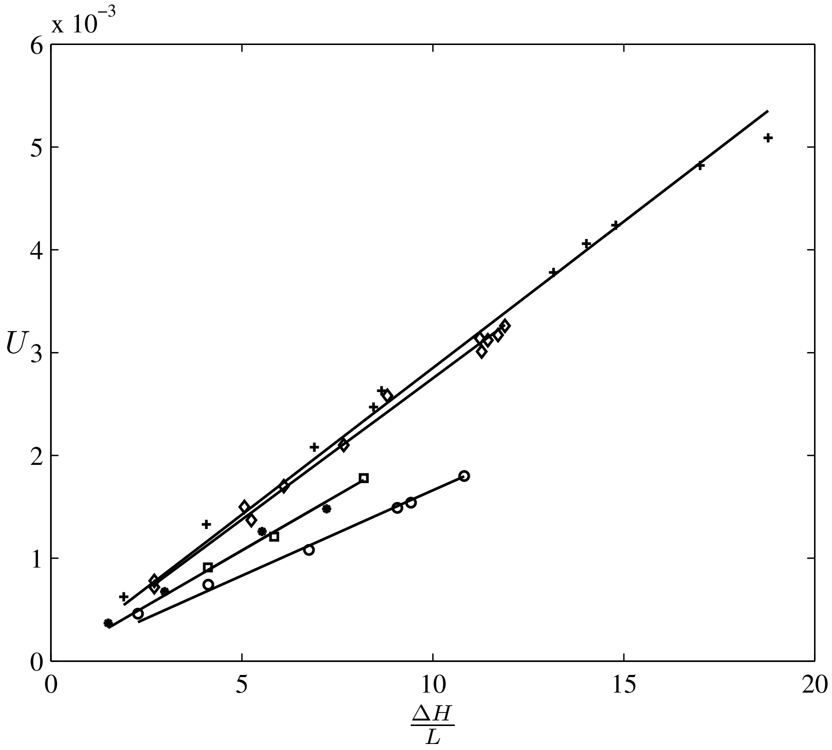

FIGURE 2.3: Darcy's experiment data. The solid line are the fit of the experimental data.

where K is the permeability. So Darcy's law becomes

$$Q = -\frac{KA}{\mu}\frac{p_2 - p_1}{L}, \tag{2.6}$$

where μ is the dynamic fluid viscosity.

Permeability represents the ease with which fluid passes through a porous material, and is a property of the material. Typical values are reported in table 2.1. We can now define a Reynolds number characteristic of the porous flow as

$$\mathrm{Re}_p = \frac{\sqrt{K}u_D}{\nu}. \tag{2.7}$$

For the flow illustrated in figure 2.4, equation (2.6) can be written for the Darcy velocity, or filtering velocity, in a differential form as:

$$u_D = \frac{Q}{A} = -\frac{K}{\mu}\frac{dp}{dx}. \tag{2.8}$$

Writing Darcy's law as

$$\frac{dp}{dx} + \frac{\mu}{K}u_D = 0, \tag{2.9}$$

Material	$-\log_{10} K$
Clean gravel	$7 \div 9$
Clean sand	$9 \div 12$
Very fine sand	$12 \div 16$
Peat	$11 \div 13$
Stratified clay	$13 \div 15$
Unweathered clay	$16 \div 20$
Oil rocks	$11 \div 14$
Sandstone	$14 \div 16$
Dolomite	$16 \div 18$
Granite	$18 \div 20$

TABLE 2.1: Some typical values of permeability taken from [2].

FIGURE 2.4: Sketch of a porous layer.

the second term can be interpreted as an average drag felt by the fluid as it passes through the porous medium, which is balanced by the pressure gradient [54, 18]. For the low porous Reynolds number for which Darcy's law hold $\mathrm{Re}_p \ll 1$, the flow is governed by Stokes' equation

$$\boldsymbol{\nabla} p - \mu \nabla^2 \boldsymbol{u} = 0. \tag{2.10}$$

Therefore, the viscous term in Stokes' equation is responsible for the Darcy drag.

As Re increases we observe a deviation from the linear relationship. To the best of our knowledge, Forchheimer was the first to suggest a nonlinear relationship, adding a quadratic drag term which provides a better fit with experimental data. The new equation is called Forchheimer equation and reads

$$\frac{dp}{dx} + \frac{\mu}{K} u_D + C u_D^2 = 0, \tag{2.11}$$

where C is a coefficient which depends both on the fluid and material properties. Recent studies have confirmed that this term is due to inertial effects in the flow within the pores [18, 54, 55, 56, 14, 21]. When the flow is no more governed by the Stokes equation the quadratic drag term is due to the convective term, $(\boldsymbol{u} \cdot \boldsymbol{\nabla})\, \boldsymbol{u}$, in the Navier-Stokes equations.

Subsequently, Brinkman [21] suggested to extend Darcy's law to high permeable materials, adding a sort of viscous term in the Stokes' equation. This results in the following equation

$$\boldsymbol{\nabla} p + \frac{\mu}{K} \boldsymbol{u_D} - \mu_e \nabla^2 \boldsymbol{u_D} = 0, \tag{2.12}$$

where μ_e is the effective Brinkman viscosity, which must be determined experimentally, and $\boldsymbol{u_D}$ is the multidimensional Darcy velocity a sort of locally averaged quantity.

From an historical point of view Darcy's law was born by experiments, but theoretical support for its validity has been obtained quite recently by Whitaker [55] by means of the method of Volume Averaging [54]. The procedure consists in averaging the microscopic flow field over a small spatial volume to obtain the macroscopic or volume-averaged flow field. Whitaker showed that Darcy's law can be deduced applying the volume averaging technique to the Stokes' equation.

2.2 Volume Averaged Navies-Stokes

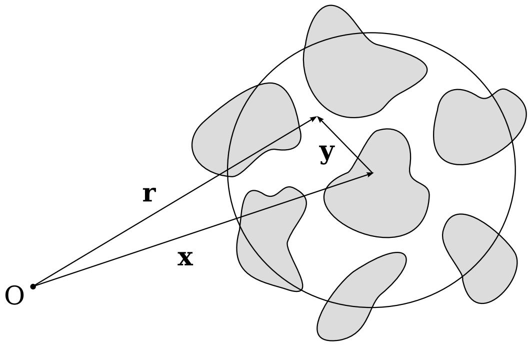

FIGURE 2.5: Sketch of porous medium with position vectors.

The method of volume averaging have been formally derived by Whitaker [54, 55, 56]. The technique considers only the large scale behaviour of the flow, i.e. , the macroscopic behaviour. This is obtained by averaging the governing equations over a small volume V of radius $r \ll L_p$, and solving for the volume averaged unknowns. A general assumption is that the length scales are well separated, $l_s \sim l_f \ll r \ll L_p$. The radius r should be large enough so that volume-averaged quantities result in smooth functions and are free of small scale fluctuations. The method involves to treat the porous medium as a continuum, so fluid quantities are defined in every point, notwithstanding it corresponds to fluid or solid phase.

Following [55, 56, 6], the first step in the derivation of the Volume Averaged Navies-Stokes (VANS) equations is the introduction of the averages. For an arbitrary quantity ϕ, the *superficial volume average* is defined as [56, 38]

$$\langle\phi\rangle|_{\boldsymbol{x}}^{s} = \frac{1}{V}\int_{V_f(\boldsymbol{x})} \phi\left(\boldsymbol{x}+\boldsymbol{y}\right) dV_f, \tag{2.13}$$

where $V_f < V$ is the volume of fluid contained within the averaging volume V, the subscript $\boldsymbol{x}$ means that $\langle\phi\rangle^s$ is evaluated at the centroid $\boldsymbol{x}$ of the averaging volume V, and $\boldsymbol{y} = \boldsymbol{r} - \boldsymbol{x}$ is the relative position vector. The position vectors used in (2.13) are identified in figure 2.5.

We can define another volume average, the *intrinsic volume average*, as

$$\langle\phi\rangle|_{\boldsymbol{x}}^{f} = \frac{1}{V_f}\int_{V_f(\boldsymbol{x})} \phi\left(\boldsymbol{x}+\boldsymbol{y}\right) dV_f, \tag{2.14}$$

The difference between the two averages is that the superficial average (2.13) is averaged over the entire averaging volume V, while the intrinsic average (2.14) is averaged over only the volume of fluid V_f. The two averages are related by

$$\langle\phi\rangle^{s} = \frac{V_f}{V}\langle\phi\rangle^{f} = \varepsilon\langle\phi\rangle^{f}, \tag{2.15}$$

where $\varepsilon = V_f/V$ is the porosity, or volume-fraction of the fluid and it is generally a function of position $\boldsymbol{x}$ in a heterogeneous porous media.

To derive the volume averaged form of the Navier-Stokes equations it is necessary to find the relations between the volume average of a derivative and the derivative of the volume average, both for time and spatial derivatives. The relationship for the volume average of a time derivative is known as *general transport theorem* [43, 38]

$$\langle\frac{\partial\phi}{\partial t}\rangle^{s} = \frac{\partial\langle\phi\rangle^{s}}{\partial t} - \frac{1}{V}\int_{A}\boldsymbol{n}\cdot\boldsymbol{w}\,\phi\,dA, \tag{2.16}$$

where A is the interface area between the fluid and the solid phase inside the averaging volume V, $\boldsymbol{n}$ is the unit normal at A that points from the fluid into the solid phase, and $\boldsymbol{n}\cdot\boldsymbol{w}$ is the local speed of displacement of the surface A. Since we restrict ourselves to rigid porous media, it holds that $\boldsymbol{w} = \boldsymbol{0}$. Consequently, for rigid porous media, the volume average of a time derivative is equal to the time derivative of the volume average. The relation for the volume average of spatial derivatives is known as the *spatial averaging theorem* [57, 37]

$$\langle\boldsymbol{\nabla}\phi\rangle^{s} = \boldsymbol{\nabla}\langle\phi\rangle^{s} + \frac{1}{V}\int_{A}\boldsymbol{n}\,\phi\,dA, \tag{2.17}$$

A useful relation for the porosity's spatial derivatives is obtained from the substitution of $\phi = 1$ in equation (2.17)

$$0 = \boldsymbol{\nabla}\langle 1\rangle^{s} + \frac{1}{V}\int_{A}\boldsymbol{n}\,dA = \boldsymbol{\nabla}\left(\varepsilon\langle 1\rangle^{f}\right) + \frac{1}{V}\int_{A}\boldsymbol{n}\,dA \implies \boldsymbol{\nabla}\varepsilon = -\frac{1}{V}\int_{A}\boldsymbol{n}\,dA. \tag{2.18}$$

A generalization of equation (2.17) is [38]

$$\boldsymbol{\nabla}\langle\boldsymbol{M}\rangle^{s} = -\frac{1}{V}\int_{A}\boldsymbol{n}\,\boldsymbol{M}\,dA, \tag{2.19}$$

where $\boldsymbol{M}$ is a tensor of n^{th} order rank.

In order to obtain the VANS we apply the volume-averaging operator $\langle \ldots \rangle^s$ to the Navier-Stokes equations, (2.1) and (2.2), for an incompressible, Newtonian fluid

$$\langle \frac{\partial \boldsymbol{u}}{\partial t} \rangle^s + \langle \boldsymbol{\nabla} \cdot (\boldsymbol{u} \otimes \boldsymbol{u}) \rangle^s = \langle -\frac{1}{\rho} \boldsymbol{\nabla} p \rangle^s + \langle \nu \nabla^2 \boldsymbol{u} \rangle^s, \tag{2.20}$$

$$\langle \boldsymbol{\nabla} \cdot \boldsymbol{u} \rangle^s = 0. \tag{2.21}$$

Application of the general transport theorem (2.16) yields

$$\langle \frac{\partial \boldsymbol{u}}{\partial t} \rangle^s = \frac{\partial \langle \boldsymbol{u} \rangle^s}{\partial t} - \frac{1}{V} \int_A \boldsymbol{n} \cdot \boldsymbol{w}\, \boldsymbol{u} \, dA = \frac{\partial \langle \boldsymbol{u} \rangle^s}{\partial t}, \tag{2.22}$$

where we have used that $\boldsymbol{w} = 0$ for rigid porous media, while the application of the spatial averaging theorem (2.17) yields

$$\langle \boldsymbol{\nabla} \cdot \boldsymbol{u} \otimes \boldsymbol{u} \rangle^s = \boldsymbol{\nabla} \cdot \langle \boldsymbol{u} \otimes \boldsymbol{u} \rangle^s + \frac{1}{V} \int_A \boldsymbol{n} \cdot \boldsymbol{u} \otimes \boldsymbol{u} \, dA = \boldsymbol{\nabla} \cdot \langle \boldsymbol{u} \otimes \boldsymbol{u} \rangle^s, \tag{2.23}$$

$$\langle -\frac{1}{\rho} \boldsymbol{\nabla} p \rangle^s = -\frac{1}{\rho} \boldsymbol{\nabla} \langle p \rangle^s - \frac{1}{V} \int_A \boldsymbol{n} \frac{p}{\rho} \, dA, \tag{2.24}$$

$$\begin{aligned} \langle \nu \nabla^2 \boldsymbol{u} \rangle^s &= \nu \boldsymbol{\nabla} \cdot \langle \boldsymbol{\nabla} \boldsymbol{u} \rangle^s + \nu \frac{1}{V} \int_A \boldsymbol{n} \cdot \boldsymbol{\nabla} \boldsymbol{u} \, dA = \\ = \nu \nabla^2 \langle \boldsymbol{u} \rangle^s + \nu \frac{1}{V} \int_A \boldsymbol{n} \cdot \boldsymbol{\nabla} \boldsymbol{u} \, dA &+ \nu \boldsymbol{\nabla} \cdot \frac{1}{V} \int_A \boldsymbol{n} \otimes \boldsymbol{u} \, dA = \\ &= \nu \nabla^2 \langle \boldsymbol{u} \rangle^s + \nu \frac{1}{V} \int_A \boldsymbol{n} \cdot \boldsymbol{\nabla} \boldsymbol{u} \, dA, \end{aligned} \tag{2.25}$$

$$\langle \boldsymbol{\nabla} \cdot \boldsymbol{u} \rangle^s = \boldsymbol{\nabla} \cdot \langle \boldsymbol{u} \rangle^s + \frac{1}{V} \int_A \boldsymbol{n} \cdot \boldsymbol{u} \, dA = \boldsymbol{\nabla} \cdot \langle \boldsymbol{u} \rangle^s, \tag{2.26}$$

where some integrals vanish since $\boldsymbol{u} = \boldsymbol{0}$ at the interface area A. The continuity equation (2.26) underlines the difference between the superficial and intrinsic volume averages; in fact in case of spatially varying porosity, only the superficial velocity is divergence free. So, we obtain

$$\begin{aligned} \frac{\partial \langle \boldsymbol{u} \rangle^s}{\partial t} + \boldsymbol{\nabla} \cdot \langle \boldsymbol{u} \otimes \boldsymbol{u} \rangle^s &= -\frac{1}{\rho} \boldsymbol{\nabla} \langle p \rangle^s + \nu \nabla^2 \langle \boldsymbol{u} \rangle^s + \\ &+ \frac{1}{V} \int_A \boldsymbol{n} \cdot \left(-\frac{p}{\rho} \boldsymbol{I} + \nu \boldsymbol{\nabla} \boldsymbol{u} \right) dA, \end{aligned} \tag{2.27}$$

$$\boldsymbol{\nabla} \cdot \langle \boldsymbol{u} \rangle^s = 0. \tag{2.28}$$

The problem defined by equations (2.27) and (2.28) lack of closure because the convective and integral terms involve not averaged quantities. The system can be written more generally as

$$\frac{\partial \langle \boldsymbol{u} \rangle^s}{\partial t} + \boldsymbol{\nabla} \cdot \left[\frac{\langle \boldsymbol{u} \rangle^s \otimes \langle \boldsymbol{u} \rangle^s}{\varepsilon} \right] + \boldsymbol{\nabla} \cdot \boldsymbol{\tau} = -\frac{1}{\rho} \boldsymbol{\nabla} \langle p \rangle^s + \nu \nabla^2 \langle \boldsymbol{u} \rangle^s + \boldsymbol{f}, \tag{2.29}$$

$$\boldsymbol{\nabla} \cdot \langle \boldsymbol{u} \rangle^s = 0, \tag{2.30}$$

where $\boldsymbol{\tau}$ is the subfilter-scale stress and $\boldsymbol{f}$ is the drag force that the solid phase exerts on the fluid phase. The definition for $\boldsymbol{\tau}$ and $\boldsymbol{f}$ are

$$\boldsymbol{\tau} \equiv \langle \boldsymbol{u} \otimes \boldsymbol{u} \rangle^s - \frac{\langle \boldsymbol{u} \rangle^s \langle \boldsymbol{u} \rangle^s}{\varepsilon}, \tag{2.31}$$

$$\boldsymbol{f} \equiv \frac{1}{V} \int_A \boldsymbol{n} \cdot \left(-\frac{p}{\rho} \boldsymbol{I} + \nu \boldsymbol{\nabla} \boldsymbol{u} \right) dA. \tag{2.32}$$

Performing the following decomposition:

$$p = \langle p \rangle^f + \tilde{p} = \frac{1}{\varepsilon} \langle p \rangle^s + \tilde{p}, \tag{2.33}$$

$$\boldsymbol{u} = \langle \boldsymbol{u} \rangle^f + \tilde{\boldsymbol{u}} = \frac{1}{\varepsilon} \langle \boldsymbol{u} \rangle^s + \tilde{\boldsymbol{u}}, \tag{2.34}$$

the integral term can be developed further

$$\begin{aligned} \boldsymbol{f} &= \frac{1}{V} \int_A \boldsymbol{n} \cdot \left(-\frac{p}{\rho} \boldsymbol{I} + \nu \boldsymbol{\nabla} \boldsymbol{u} \right) dA = \\ &= \frac{1}{V} \int_A \boldsymbol{n} \cdot \left[-\frac{\left(\langle p \rangle^f + \tilde{p} \right)}{\rho} \boldsymbol{I} + \nu \boldsymbol{\nabla} \left(\langle \boldsymbol{u} \rangle^f + \tilde{\boldsymbol{u}} \right) \right] dA = \\ &= \frac{1}{V} \int_A \boldsymbol{n} \cdot \left(-\frac{\langle p \rangle^f}{\rho} \boldsymbol{I} + \nu \boldsymbol{\nabla} \langle \boldsymbol{u} \rangle^f \right) dA + \frac{1}{V} \int_A \boldsymbol{n} \cdot \left(-\frac{\tilde{p}}{\rho} \boldsymbol{I} + \nu \boldsymbol{\nabla} \tilde{\boldsymbol{u}} \right) dA = \\ &= -\boldsymbol{\nabla} \varepsilon \cdot \left(-\frac{\langle p \rangle^f}{\rho} \boldsymbol{I} + \nu \boldsymbol{\nabla} \langle \boldsymbol{u} \rangle^f \right) dA + \frac{1}{V} \int_A \boldsymbol{n} \cdot \left(-\frac{\tilde{p}}{\rho} \boldsymbol{I} + \nu \boldsymbol{\nabla} \tilde{\boldsymbol{u}} \right) dA. \end{aligned} \tag{2.35}$$

Exploiting (2.35) and

$$-\frac{1}{\rho} \boldsymbol{\nabla} \langle p \rangle^s = -\frac{1}{\rho} \boldsymbol{\nabla} \left(\langle p \rangle^f \varepsilon \right) = -\frac{\varepsilon}{\rho} \boldsymbol{\nabla} \langle p \rangle^f - \frac{1}{\rho} \langle p \rangle^f \boldsymbol{\nabla} \varepsilon, \tag{2.36}$$

the Volume Averaged Navier-Stokes (VANS) equations become

$$\begin{aligned} \frac{\partial \langle \boldsymbol{u} \rangle^s}{\partial t} + \boldsymbol{\nabla} \cdot \left[\frac{\langle \boldsymbol{u} \rangle^s \otimes \langle \boldsymbol{u} \rangle^s}{\varepsilon} \right] + \boldsymbol{\nabla} \cdot \boldsymbol{\tau} = -\frac{\varepsilon}{\rho} \boldsymbol{\nabla} \langle p \rangle^f + \nu \nabla^2 \langle \boldsymbol{u} \rangle^s + \\ -\nu \boldsymbol{\nabla} \varepsilon \cdot \boldsymbol{\nabla} \langle \boldsymbol{u} \rangle^s + \frac{1}{V} \int_A \boldsymbol{n} \cdot \left(-\frac{\tilde{p}}{\rho} \boldsymbol{I} + \nu \boldsymbol{\nabla} \tilde{\boldsymbol{u}} \right) dA, \end{aligned} \tag{2.37}$$

$$\boldsymbol{\nabla} \cdot \langle \boldsymbol{u} \rangle^s = 0. \tag{2.38}$$

The first viscous term $\nu \nabla^2 \langle \boldsymbol{u} \rangle^s$ is the Brinkman correction and it is often included in the analysis of flow in the boundary region between a porous medium and a homogeneous fluid. In such regions the second viscous term $\nu \boldsymbol{\nabla} \varepsilon \cdot \boldsymbol{\nabla} \langle \boldsymbol{u} \rangle^s$ has the same order of magnitude as the Brinkman correction, and, generally, it can not be neglected. The latter is referred to as the second Brinkman correction. A key point about equations (2.37) and (2.38) is that they are valid everywhere since no length scale constraints have been imposed.

It has been shown [55] that the integral term

$$\frac{1}{V_f}\int_A \boldsymbol{n}\cdot\left(-\tilde{p}\boldsymbol{I}+\mu\boldsymbol{\nabla}\tilde{\boldsymbol{u}}\right)dA=-\mu\boldsymbol{\phi}, \tag{2.39}$$

has an especially simple form in a homogeneous porous medium $\boldsymbol{\nabla}\varepsilon = 0$, where it can be written as

$$-\mu\boldsymbol{\phi}=-\mu\boldsymbol{K}^{-1}\cdot\langle\boldsymbol{u}\rangle^s-\mu\boldsymbol{K}^{-1}\cdot\boldsymbol{F}\cdot\langle\boldsymbol{u}\rangle^s, \tag{2.40}$$

where $\boldsymbol{K}$ is the second-order permeability tensor. The first term is called Darcy drag, while the second is the Forchheimer term. $\boldsymbol{F}$ is a second-order tensor whose exact form depends on the structure of the porous medium. Experimentally, it is usually found to be a linear function of the volume averaged velocity $\langle\boldsymbol{u}\rangle^s$, producing a Forchheimer term that is quadratic [5, 18, 56, 14]. Moreover, Whitaker [56] found that the convective terms generated by the nonlinear part of the Navier-Stokes equations are of the same order of magnitude and are both usually negligible in comparison with the dominant Forchheimer term. The latter is negligible when the inertial effects are small.

In the homogeneous region, where $\boldsymbol{\nabla}\varepsilon = 0$, and for an isotropic porous material with small inertial effects, the VANS equations become

$$\frac{\partial\langle\boldsymbol{u}\rangle^s}{\partial t}=-\frac{\varepsilon}{\rho}\boldsymbol{\nabla}\langle p\rangle^f+\nu\nabla^2\langle\boldsymbol{u}\rangle^s-\frac{\nu}{K}\varepsilon\langle\boldsymbol{u}\rangle^s, \tag{2.41}$$

$$\boldsymbol{\nabla}\cdot\langle\boldsymbol{u}\rangle^s=0. \tag{2.42}$$

So far we have adopted the convention of preferring the superficial volume-averaged velocity $\langle\boldsymbol{u}\rangle$ and the intrinsic volume averaged pressure $\langle p\rangle^f$. When dealing with VANS equations, the superficial volume-averaged velocity $\langle\boldsymbol{u}\rangle$ is the preferred representation of the velocity since it is always solenoidal, while the intrinsic volume-averaged velocity $\langle\boldsymbol{u}\rangle^f$ is only solenoidal in the case of constant porosity. However for the pressure the intrinsic volume average $\langle p\rangle^f$ is preferred, because it is the one measured by a probe in an experimental apparatus.

2.2.1 Darcy's law

Whitaker [55] and Ochoa-Tapia and Whitaker [31] have shown that volume averaging the Stokes' equations for a stationary, incompressible, viscous flow through a rigid homogeneous porous medium (2.10) produces Darcy's law with the Brinkman term

$$-\boldsymbol{\nabla}\langle p\rangle^f+\frac{\mu}{\varepsilon}\nabla^2\langle\boldsymbol{u}\rangle-\mu\boldsymbol{K}^{-1}\cdot\langle\boldsymbol{u}\rangle=0. \tag{2.43}$$

Note that volume averaging produces a Brinkman term, $\mu/\varepsilon\nabla^2\langle\boldsymbol{u}\rangle$, without an effective viscosity. Ochoa-Tapia and Whitaker [31] found also that the Brinkman term is usually negligible in comparison with the dominant pressure and Darcy terms. The exception is near the interface between a porous region and a purely fluid region.

2.2.2 LES analogy

The VANS procedure can be considered as a generalization of the LES procedure. The volume-averaging operator (2.13) acts as a filter which passes only information on the large scale structures of the flow field. It can be generalized defining a filter operator analogous to the one used in Large Eddy Simulations [37, 38, 23, 6] as it follows

$$\langle\phi\rangle|_{\boldsymbol{x}}^{s} = \int_V m\left(\boldsymbol{y}\right)\gamma\left(\boldsymbol{r}\right)\phi\left(\boldsymbol{r}\right)dV, \tag{2.44}$$

where γ is the phase-indicator function and m is a weighting function. γ equals unity when $\boldsymbol{r}$ points in the fluid phase and zero when $\boldsymbol{r}$ points in the solid phase. The weighting function must satisfy the following normalization condition

$$\int_V m\left(\boldsymbol{y}\right)dV = 1. \tag{2.45}$$

The LES equations can be obtained from the VANS equations (2.29) and (2.30) for a purely homogeneous fluid region, where $\varepsilon = 1$, and observing that, because of the absence of a solid phase the drag force is zero $\boldsymbol{f} = 0$

$$\frac{\partial\langle\boldsymbol{u}\rangle^s}{\partial t} + \boldsymbol{\nabla}\cdot\left(\langle\boldsymbol{u}\rangle^s\otimes\langle\boldsymbol{u}\rangle^s\right) + \boldsymbol{\nabla}\cdot\boldsymbol{\tau} = -\frac{1}{\rho}\boldsymbol{\nabla}\langle p\rangle^s + \nu\nabla^2\langle\boldsymbol{u}\rangle^s, \tag{2.46}$$

$$\boldsymbol{\nabla}\cdot\langle\boldsymbol{u}\rangle^s = 0. \tag{2.47}$$

2.3 Interface conditions

The problem of momentum transport at the boundary between a porous medium and a homogeneous fluid, see figure 2.6, occurs in a wide variety of technological applications, and has been the object of a great deal of study in the porous flow community. In order to study the problem, we consider a flat channel delimited by an upper impermeable wall and a lower, semi-infinite porous wall, as illustrated in figure 2.7(a). In particular, porous layers are fluid saturated, rigid, homogeneous and isotropic. A uniform longitudinal pressure gradient dp/dx drives a steady fully developed laminar flow in both the channel and porous region.

At the interface, the fluid velocity must decrease from its interface value to the Darcy velocity. This is achieved in the so called Brinkman layer. This small region is where mass and momentum transfer take place.

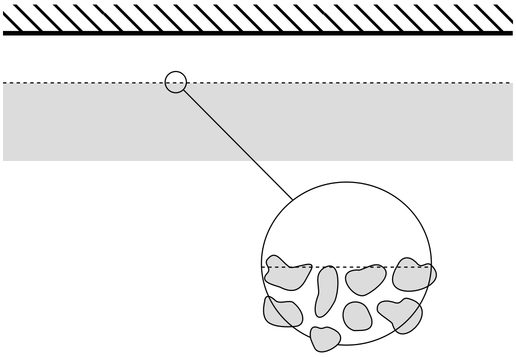

Figure 2.6: Interface between a porous region and a purely fluid region.

The interface can be treated mainly in two ways, as smooth (within a single-domain model) or sharp (within a two-domain model). In the single-domain approach, the composite region is considered as a continuum and one set of general governing equations is applied for the whole domain. All averaged flow variables are continuous and the change in flow physics is simulated by varying porosity. In the two-domain approach, two sets of governing equations are applied to describe the flow in the two regions and additional boundary conditions are applied at the interface to close the two sets of equations. The interface region is replaced with an interface of zero height, and both the free-fluid and porous regions are extrapolated over the interface region, resulting in step change of some flow variables across the interface. This method is more reliable, since it tries to simulate the flow behaviour at the interface and it will be used in this work.

For a systematic analysis of the variance among different boundary conditions see Alazmi and Vafai [1]. In this work, the authors concluded that, in most of

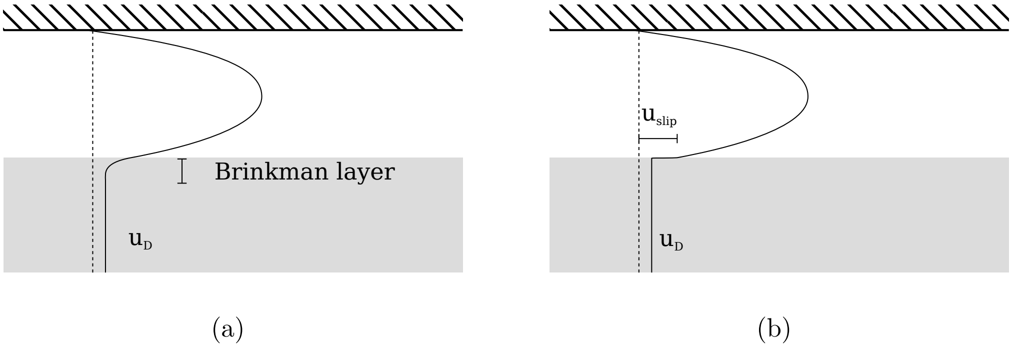

Figure 2.7: Velocity profiles of the flow through a porous medium, not to scale. Figure (b) shows the velocity profile obtained with the Beavers and Joseph condition.

the cases, the variances between the different models have negligible effect on the results.

2.3.1 The Beavers and Joseph condition

To the best of our knowledge, Beavers and Joseph [3] were the first to prove that when a viscous fluid flows at the interface of a porous medium, the effects of viscous shear will penetrate beneath the permeable surface, to form what is effectively a boundary layer, the Brinkman layer. They performed a series of experiments and they observed that the slip velocity at the interface differs from the Darcy velocity u_D. In fact Darcy's law is not compatible with the existence of a boundary layer region, because no macroscopic shear term is associated with this equation. They proposed to model the effects of the Brinkamn layer on the external flow by introducing a discontinuous slip velocity, u_{slip}, as shown in figure 2.7(b). They postulated that this slip velocity is proportional to the shear rate, du/dy, at the permeable boundary

Material	10^{-5}**K** $[in^2]$	α	τ
Foametal A	1.5	0.78	0.70
Foametal B	6.1	1.45	0.00
Foametal C	12.7	4.00	-1.00
Aloxite	0.1	0.10	1.47

TABLE 2.2: Some typical values of permeability together with the coefficient α_{BJ} determined experimentally by Beavers and Joseph [3], and the momentum transfer coefficient τ determined by Ochoa-Tapia and Whitaker [32] assuming $\varepsilon = 0.4$.

$$\frac{du}{dy} = \frac{\alpha_{BJ}}{\sqrt{K}} (u_{slip} - u_D) \tag{2.48}$$

where α_{BJ} is a dimensionless coefficient which depends on the structure of the porous material in the boundary region, and that must be determined by experiments. Beavers and Joseph calculated it for the materials reported in table 2.2.

Beavers, Sparrow and Magnuson [4] confirmed the Beavers and Joseph condition experimentally, while Saffman [40] further justified it theoretically. Saffman also found that, as the permeability tends to small but finite values, the Darcy velocity in the Beavers and Joseph interface condition may be ignored.

Taylor [46] and Richardson [39] collaborated in order to perform an experiment with a particular porous material for which both K and α could be calculated analytically, and they compared the results of calculation with experiments.

The geometry of the porous media is called Taylor brush configuration, and it has been further studied by other authors, as in [42].

Other authors determined the values of the slip coefficient α_{BJ} for other materials and other geometries. Liu, Chen and Wang [24] performed an experimental and numerical estimation of slip coefficient in a partially porous cavity. Their paper reported an experimental investigation of natural convection flow in a two-dimensional cavity, partially filled with a vertical porous layer.

2.3.2 The Brinkman condition

The Beavers and Joseph condition does not provide information on the structure of the Brinkman layer within the porous region. Neale and Nader [30] reconsidered the channel problem and modelled the flow in the porous region using the Brinkman equation

$$\frac{dp}{dx} = -\frac{\mu}{K} u_D + \mu_e \frac{d^2 u_d}{dy^2}. \tag{2.49}$$

Thanks to the macroscopic shear term, the Brinkman equation is fully compatible with the presence of a boundary layer region within the porous medium; outside the Brinkman layer, the Brinkman term is very small, indicating that Darcy's law is valid everywhere except at the boundaries.

In order to couple the flow through the porous material and through the fluid region, they imposed continuity of velocity and its derivative at the interface, using the following interface conditions

$$u = u_D \qquad \mu \frac{du}{dy} = \mu_e \frac{du_D}{dy}. \tag{2.50}$$

While these conditions where first proposed by Neale and Nader, they are also commonly referred to as Brinkman interface conditions.

Neale and Nader discovered that their conditions (2.50) produce the same interface velocity as the slip velocity predicted by the Beavers and Joseph condition (2.50), provided that

$$\mu_e = \mu \alpha_{BJ}^2. \tag{2.51}$$

It is useful to define the Brinkman layer thickness δ_B as the distance measured from the interface into the porous region at which the fluid velocity first approaches within 1 of the Darcy velocity; the Brinkman conditions also predict that the Brinkman layer thickness δ_B is of the order of the square root of the permeability, $\delta_B \sim \sqrt{k}$.

We have observed that in order to agree with the experimental data of Beaver and Joseph, the effective viscosity must satisfy relation (2.51). However, in order to agree with Whitaker's derivation of VANS, it must satisfy

$$\mu_e = \frac{\mu}{\varepsilon}, \tag{2.52}$$

see equations (2.12) and (2.43). Generally, it is not possible to satisfy all these relationships simultaneously.

2.3.3 The momentum transfer conditions of Ochoa-Tapia and Whitaker

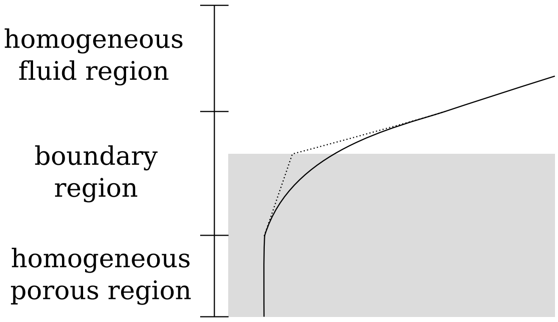

FIGURE 2.8: Fluid velocity profile at the interface between a porous region and a purely fluid region.

Figure 2.8 illustrates a hypotetical fluid velocity profile at the interface between a porous region and a purely fluid region. In this region the flow is governed by equations (2.37) and (2.38),

$$\begin{aligned} &\frac{\partial\langle \boldsymbol{u}\rangle^s}{\partial t} + \boldsymbol{\nabla}\cdot\left[\frac{\langle \boldsymbol{u}\rangle^s \otimes \langle \boldsymbol{u}\rangle^s}{\varepsilon}\right] + \boldsymbol{\nabla}\cdot\boldsymbol{\tau} = -\frac{\varepsilon}{\rho}\boldsymbol{\nabla}\langle p\rangle^f + \nu\nabla^2\langle \boldsymbol{u}\rangle^s + \\ &\qquad -\nu\boldsymbol{\nabla}\varepsilon\cdot\boldsymbol{\nabla}\langle \boldsymbol{u}\rangle^s - \nu\varepsilon\boldsymbol{K}^{-1}\cdot\langle \boldsymbol{u}\rangle^s - \nu\varepsilon\boldsymbol{K}^{-1}\cdot\boldsymbol{F}\cdot\langle \boldsymbol{u}\rangle^s, \end{aligned} \tag{2.53}$$

$$\boldsymbol{\nabla}\cdot\langle \boldsymbol{u}\rangle^s = 0, \tag{2.54}$$

which have been obtained without imposing any length scale constraints. Solution of the problem requires the knowledge of the variation of porosity within the transition region; moreover, suitable models are necessary to evaluate nonlinear terms and Forchheimer tensor. For recent developments on this approach, we refer the reader to Valdes, Goycau and Ochoa-Tapia [52] and Breugem [6]. Usually, the variation of the porosity in the transition region is not known in advance, so the problem requires closure. Providing a suitable profile for ε is difficult even experimentally. This problem can be avoided if an acceptable jump condition is constructed.

In a region sufficiently below the interface, we assume the porous material is homogeneous and the flow is governed by the VANS and continuity equations

(2.41) and (2.42),

$$\frac{\partial \langle \boldsymbol{u} \rangle^s}{\partial t} = -\frac{\varepsilon}{\rho} \boldsymbol{\nabla} \langle p \rangle^f + \nu \nabla^2 \langle \boldsymbol{u} \rangle^s - \frac{\nu}{K} \varepsilon \langle \boldsymbol{u} \rangle^s, \tag{2.55}$$

$$\boldsymbol{\nabla} \cdot \langle \boldsymbol{u} \rangle^s = 0. \tag{2.56}$$

This region is called the homogeneous porous region. Previous equations are not valid in a small heterogenous transition layer adjacent to the interface, where the structure of the porous material undergoes rapid changes. For example, the porosity increase rapidly from its value in the homogeneous porous region ε to unity slightly above the interface.

We extend validity of equations (2.55) and (2.56) to the interface, even if the porous material is heterogeneous. As consequence, this assumption produces an error in the local averaged velocity $\langle \boldsymbol{v} \rangle^s$ and pressure $\langle \boldsymbol{p} \rangle^f$. However, the error will be corrected by means of an additional condition, the so-called jump condition, which ensures that equations (2.53) and (2.54) are satisfied on average in the boundary region.

The conditions created by Ochoa-Tapia and Whitaker couple the Navier-Stokes equations (2.1) and (2.2) directly to the Volume Averaged Navier-Stokes equations (2.55) and (2.55). The velocity and the pressure are forced to be continuous at the interface and generally produce a discontinuity in the shear stress. In figure 2.8 the dashed line illustrates a hypotetical velocity profile generated by the interface conditions of Ochoa-Tapia and Whitaker; note that the conditions may not predict the profile of the Brinkman layer as accurately as equations (2.53) and (2.54).

When the porous region is homogeneous and isotropic, and the permeability is sufficiently small to neglect inertial effects, the momentum transfer conditions are [31]

$$u = \langle u \rangle^s, \tag{2.57a}$$

$$v = \langle v \rangle^s, \tag{2.57b}$$

$$w = \langle w \rangle^s, \tag{2.57c}$$

$$p = \langle p \rangle, \tag{2.57d}$$

$$\frac{1}{\varepsilon} \frac{\partial \langle u \rangle^s}{\partial y} - \frac{\partial u}{\partial y} = \pm \frac{\tau}{\sqrt{K}} u, \tag{2.57e}$$

$$\frac{1}{\varepsilon} \frac{\partial \langle w \rangle^s}{\partial y} - \frac{\partial w}{\partial y} = \pm \frac{\tau}{\sqrt{K}} w. \tag{2.57f}$$

In equations (2.57) positive sign is used when the purely fluid region is above a porous interface, while the negative sign denotes the converse. Symbol τ has been introduced as constant coefficient which accounts for the distribution of momentum at the interface and depends on the manner in which a porous material's structure varies in the transition layer. While there is work on determining τ

theoretically [52], it must usually be determined experimentally. Analytically, Ochoa-Tapia and Whitaker [31] estimated that τ is of the order of one and may be either positive or negative.

Ochoa-Tapia and Whitaker [32] found that conditions (2.57) showed good agreement with the experimental data of Beavers and Joseph [3]. The results for τ are summarized in table 2.2.

When inertial effects are significant in the porous region the jump condition is more complicated. Ochoa-Tapia and Whitaker [33] extended the stress condition to include inertial effects

$$\frac{1}{\varepsilon}\frac{\partial\langle u\rangle^s}{\partial y} - \frac{\partial u}{\partial y} = \pm\frac{\tau}{\sqrt{K}}u \pm \frac{\gamma}{\nu}u^2, \tag{2.58}$$

where γ, which accounts for the effects of inertia in the momentum transfer process, is a dimensionless coefficient of order one that must be determined experimentally; anyway there are currently no published experimental data for it.

The stress jump boundary conditions (2.57) has been studied and used by many researchers.

Kuznetsov [20] investigated the dependence of the velocity on the adjustable coefficient in the stress jump boundary condition. He obtained analytical solutions for three different types of channels partially filled with a porous medium and the stress jump boundary condition is utilized at the interface. He showed that accounting for a jump in the shear stress at the interface essentially influences velocity profiles.

Tan and Pillai [45] considered the interface between a porous medium and a clear fluid. Their results have shown that, when the porosity of the porous media is high, the stress jump condition yields a result significantly different from the one provided by the stress-continuity condition. It is also shown that when the porosity of the porous medium is high, the stress continuity condition results in a much larger boundary layer as compared to the stress jump condition. However, the two interface conditions tend to yield similar results as the porosity decreases.

Yu, Lee, Zeng and Low [58] and Chen, Yu, Winoto and Low [10] developed a numerical method for flows involving an interface between a homogeneous fluid and a porous medium. The Brinkman-Forcheimmer extended model was used to govern the flow in the porous medium region. At its interface, the flow boundary condition imposed is a shear stress jump, which includes the inertial effect, together with a continuity of normal stress.

Costa, Oliveira and Baliga [11] implemented the stress jump condition simulating laminar coupled flows in adjacent open and porous domains.

Chapter 3

Problem definition

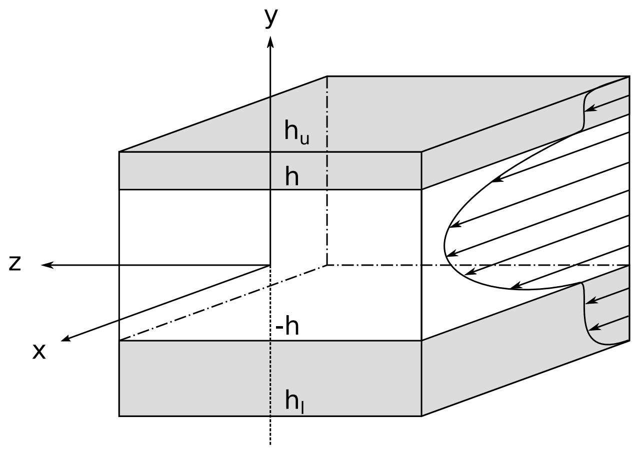

FIGURE 3.1: Sketch of the channel geometry.

We consider the flow of an incompressible viscous fluid through a channel with flat porous walls, as sketched in fig 3.1. We assume the porous layers to be fluid saturated, rigid, homogeneous and isotropic. We model the fluid flow through the porous medium using the Volume Averaged Navier-Stokes equations (2.41) and (2.42). The momentum transfer at each interface between the purely fluid region and porous layer is described by the conditions derived by Ochoa-Tapia and Whitaker (2.57). At the walls, we impose the no-penetration and no-slip conditions. The fully developed turbulent channel flow is homogeneous in the streamwise and spanwise directions, and periodic boundary conditions are used in these directions.

We consider the cartesian coordinate system shown in figure 3.1, where x, y and z denote the streamwise, wall-normal and spanwise coordinates, while u, v and w denote the respective components of the velocity vector field. The lower and upper interface are located at $y = -h$ and $y = h$, respectively, while the lower and upper impermeable walls are located at $y = h_l = -h - 2hh_{p_1}$ and $y = h_u = h + 2hh_{p_2}$, respectively. In the above relationships, h_{p_1} and h_{p_2} are the non-dimensional half-heights of the lower and upper porous layers, respectively.

3.1 Non-dimensional equations

We formulate the mathematical problem and make it dimensionless. Note that non-dimensional quantities are identified by the superscript "$^-$".

We define as a characteristic length one-half the height of the central purely fluid layer

$$L^\star = h, \tag{3.1}$$

and as characteristic velocity $U^\star$

$$U^\star = U_b = \frac{1}{h_u - h_l} \int_{h_l}^{h_u} U dy, \tag{3.2}$$

where $U(y)$ can be either the laminar or turbulent mean velocity profile. Therefore, the Reynolds number is defined as

$$\mathrm{Re} = \frac{U^\star L^\star}{\nu}. \tag{3.3}$$

3.1.1 Navier-Stokes equations

To make the Navier-Stokes equations (2.1) and (2.2) nondimensional, we use the reference length $L^\star$, the reference velocity $U^\star$ and define as reference time $T^\star = L^\star / U^\star$. Then, writing $u = U^\star \bar{u}$ and $p = \rho {U^\star}^2 \bar{p}$ and dividing the two equations respectively by ${U^\star}^2 / L^\star$ and $U^\star / L^\star$, we obtain the non-dimenional Navier-Stokes equations

$$\frac{\partial \bar{\boldsymbol{u}}}{\partial \bar{t}} + \boldsymbol{\nabla} \cdot (\bar{\boldsymbol{u}} \otimes \bar{\boldsymbol{u}}) = -\boldsymbol{\nabla} \bar{p} + \frac{1}{\mathrm{Re}} \nabla^2 \bar{\boldsymbol{u}}, \tag{3.4}$$

$$\boldsymbol{\nabla} \cdot \bar{\boldsymbol{u}} = 0. \tag{3.5}$$

3.1.2 Volume Averaged Navier-Stokes equations

In this study we model the flow through the porous media with equations (2.41) and (2.42), that we report here for convenience

$$\begin{aligned} \frac{\partial \langle \boldsymbol{u} \rangle^s}{\partial t} &= -\frac{\varepsilon}{\rho} \boldsymbol{\nabla} \langle p \rangle^f + \nu \nabla^2 \langle \boldsymbol{u} \rangle^s - \frac{\nu}{K} \varepsilon \langle \boldsymbol{u} \rangle^s, \\ \boldsymbol{\nabla} \cdot \langle \boldsymbol{u} \rangle^s &= 0. \end{aligned}$$

To make the above equations nondimensional, we use the reference length $L^\star$, the reference velocity $U^\star$ and define as reference time $T^\star = L^\star / U^\star$. Then, writing $u =$

$U^\star \bar{u}$ and $p = \rho {U^\star}^2 \bar{p}$ and dividing the two equations respectively by ${U^\star}^2/L^\star$ and $U^\star/L^\star$, we obtain the non-dimensional Volume-Averaged Navier-Stokes equations

$$\frac{\partial \langle \bar{\boldsymbol{u}} \rangle^s}{\partial t} = -\varepsilon \boldsymbol{\nabla} \langle \bar{p} \rangle^f + \frac{1}{\mathrm{Re}} \nabla^2 \langle \bar{\boldsymbol{u}} \rangle^s - \frac{\varepsilon}{\sigma^2 \mathrm{Re}} \langle \bar{\boldsymbol{u}} \rangle^s, \tag{3.6}$$

$$\boldsymbol{\nabla} \cdot \langle \bar{\boldsymbol{u}} \rangle^s = 0, \tag{3.7}$$

where $\sigma = \dfrac{\sqrt{K}}{L^\star}$ is the non-dimensional permeability.

3.1.3 Boundary and interface momentum transfer conditions

At the solid walls, no-slip and no-penetration conditions hold. These boundary conditions written in non-dimensional form are

$$\langle \bar{u} \rangle^s = 0, \tag{3.8a}$$

$$\langle \bar{v} \rangle^s = 0, \tag{3.8b}$$

$$\langle \bar{w} \rangle^s = 0. \tag{3.8c}$$

When the porous region is homogeneous and isotropic, and the permeability is sufficiently small to neglect inertial effects, the momentum transfer conditions at the interface with the fluid region are (2.57). Their non-dimensional form is

$$\bar{u} = \langle \bar{u} \rangle^s, \tag{3.9a}$$

$$\bar{v} = \langle \bar{v} \rangle^s, \tag{3.9b}$$

$$\bar{w} = \langle \bar{w} \rangle^s, \tag{3.9c}$$

$$\bar{p} = \langle \bar{p} \rangle, \tag{3.9d}$$

$$\frac{\sigma}{\varepsilon} \frac{\partial \langle \bar{u} \rangle^s}{\partial \bar{y}} - \sigma \frac{\partial \bar{u}}{\partial \bar{y}} = \pm \tau \bar{u}, \tag{3.9e}$$

$$\frac{\sigma}{\varepsilon} \frac{\partial \langle \bar{w} \rangle^s}{\partial \bar{y}} - \sigma \frac{\partial \bar{w}}{\partial \bar{y}} = \pm \tau \bar{w}. \tag{3.9f}$$

where we use the ± symbol with the positive sign to refer to an interface below the purely fluid region, and with the negative sign to refer to an interface above the purely fluid region. From now on, we will consider only non-dimensional quantities and we will omit, for simplicity, the superscript "$^-$".

3.2 v-η formulation

In this section, we rewrite the two pairs of equations (3.4) and (3.5), and (3.6) and (3.7) in the primitive variables $\boldsymbol{u}$ and p with another set of equations, where pressure formally disappears and is replaced by the normal component of vorticity η.

3.2.1 Navier-Stokes equations

The wall-normal component of the vorticity vector η is defined as

$$\eta = \frac{\partial u}{\partial z} - \frac{\partial w}{\partial x}, \tag{3.10}$$

A one-dimensional, second-order, evolution equation for η can be obtained subtracting the x-derivative of the z-component of momentum equation from the z-derivative of the x-component of the same equation. We have

$$\frac{\partial^2 u}{\partial z \partial t} - \frac{\partial^2 w}{\partial x \partial t} = \frac{\partial^2 p}{\partial z \partial x} - \frac{\partial^2 p}{\partial x \partial z} + \frac{1}{\mathrm{Re}} \frac{\partial \nabla^2 u}{\partial z} - \frac{1}{\mathrm{Re}} \frac{\partial \nabla^2 w}{\partial x} + \frac{\partial HU}{\partial z} - \frac{\partial HW}{\partial x}, \tag{3.11}$$

where

$$HU = -\frac{\partial (uu)}{\partial x} - \frac{\partial (uv)}{\partial y} - \frac{\partial (uw)}{\partial z}, \tag{3.12}$$

$$HW = -\frac{\partial (wu)}{\partial x} - \frac{\partial (wv)}{\partial y} - \frac{\partial (ww)}{\partial z}. \tag{3.13}$$

Using the definition (3.10), the equation for the normal vorticity (3.11) can be rewritten as

$$\frac{\partial \eta}{\partial t} = \frac{\partial HU}{\partial z} - \frac{\partial HW}{\partial x} + \frac{1}{\mathrm{Re}} \nabla^2 \eta. \tag{3.14}$$

To obtain an equation for the wall-normal velocity component v free of pressure, we take the laplacian of the y-component of momentum equation (3.4)

$$\frac{\partial \nabla^2 v}{\partial t} = -\frac{\partial \nabla^2 p}{\partial y} + \frac{1}{\mathrm{Re}} \nabla^2 \nabla^2 v + \nabla^2 HV, \tag{3.15}$$

where

$$HV = -\frac{\partial (vu)}{\partial x} - \frac{\partial (vv)}{\partial y} - \frac{\partial (vw)}{\partial z}. \tag{3.16}$$

In order to eliminate the pressure term in (3.15), we use the Poisson equation obtained by taking the divergence of the momentum equation (3.4)

$$\nabla^2 p = \frac{\partial HU}{\partial x} + \frac{\partial HV}{\partial y} + \frac{\partial HW}{\partial z}. \tag{3.17}$$

Therefore, we obtain

$$\frac{\partial \nabla^2 v}{\partial t} = -\frac{\partial^2 HU}{\partial y \partial x} - \frac{\partial^2 HW}{\partial y \partial z} + \frac{\partial^2 HV}{\partial x^2} + \frac{\partial^2 HV}{\partial z^2} + \frac{1}{\mathrm{Re}} \nabla^2 \nabla^2 v. \tag{3.18}$$

Finally, continuity equation (3.5)

$$\frac{\partial u}{\partial x} + \frac{\partial w}{\partial z} = -\frac{\partial v}{\partial y}, \tag{3.19}$$

and the definition of η (3.10)

$$\frac{\partial u}{\partial z} - \frac{\partial w}{\partial x} = \eta, \tag{3.20}$$

form a 4×4 system with equations (3.14) and (3.18) in the unknowns u, v, w and η.

3.2.2 Volume Averaged Navier-Stokes equations

Analogously to the definition (3.10), the wall-normal component of the volume averaged vorticity $\langle \eta \rangle^s$ is defined as

$$\langle \eta \rangle^s = \frac{\partial \langle u \rangle^s}{\partial z} - \frac{\partial \langle w \rangle^s}{\partial x}. \tag{3.21}$$

We apply the same procedure described in sub-section (3.2.1). We subtract the x-derivative of the z-component of momentum equation (3.6) from the z-derivative of the x-component of the same equation. We obtain

$$\frac{\partial^2 \langle u \rangle^s}{\partial z \partial t} - \frac{\partial^2 \langle w \rangle^s}{\partial x \partial t} = \frac{1}{\mathrm{Re}} \left(\frac{\partial \nabla^2 \langle u \rangle^s}{\partial z} - \frac{\partial \nabla^2 \langle w \rangle^s}{\partial x} \right) - \frac{\varepsilon}{\sigma^2 \mathrm{Re}} \left(\frac{\partial \langle u \rangle^s}{\partial z} - \frac{\partial \langle w \rangle^s}{\partial x} \right). \tag{3.22}$$

Exploiting the definition of the wall-normal component of the volume averaged vorticity $\langle \eta \rangle^s$ (3.21), the above equation can be rewitten as follows

$$\frac{\partial \langle \eta \rangle^s}{\partial t} = \frac{1}{\mathrm{Re}} \nabla^2 \langle \eta \rangle^s - \frac{\varepsilon}{\sigma^2 \mathrm{Re}} \langle \eta \rangle^s. \tag{3.23}$$

Note that, differently from equation (3.14), the above equation does not contain any non-linear terms. This is due to the fact that we have considered negligible inertial effects in the porous layers. Moreover, in the above equation there is a zero-order term, $\langle \eta \rangle^s \varepsilon / (\sigma^2 \mathrm{Re})$, which comes from the Darcy drag $\langle \boldsymbol{u} \rangle^s \varepsilon / (\sigma^2 \mathrm{Re})$ of equation (3.6).

As described for the Navier-Stokes equations, in order to find an equation for $\langle v \rangle^s$ we take the laplacian of the y-component of momentum equation,

$$\frac{\partial \nabla^2 \langle v \rangle^s}{\partial t} = -\varepsilon \nabla^2 \frac{\partial \langle p \rangle^f}{\partial y} + \frac{1}{\mathrm{Re}} \nabla^2 \nabla^2 \langle v \rangle^s - \frac{\varepsilon}{\sigma^2 \mathrm{Re}} \nabla^2 \langle v \rangle^s \tag{3.24}$$

Average pressure is eliminated from the previous equation by using the Poisson equation

$$\varepsilon \nabla^2 \langle p \rangle^f = 0. \tag{3.25}$$

Differently from equation (3.17), the above equation is homogeneous. Therefore, the volume-averaged pressure $\langle p \rangle^f$ is determined only by boundary conditions at the impermeable wall and by the momentum transfer condition at the interface with the fluid region. Using equation (3.25), the normal velocity equation (3.24) becomes

$$\frac{\partial \nabla^2 \langle v\rangle^s}{\partial t} = \frac{1}{\mathrm{Re}}\nabla^2\nabla^2\langle v\rangle^s - \frac{\varepsilon}{\sigma^2\mathrm{Re}}\nabla^2\langle v\rangle^s. \tag{3.26}$$

Note that in the above equation, analogously to equation (3.23), non-linear terms are missing, while is present the laplacian Darcy drag term.

Continuity equation (3.7)

$$\frac{\partial\langle u\rangle^s}{\partial x} + \frac{\partial\langle w\rangle^s}{\partial z} = -\frac{\partial\langle v\rangle^s}{\partial y}, \tag{3.27}$$

and the definition of η (3.21)

$$\frac{\partial\langle u\rangle^s}{\partial z} - \frac{\partial\langle w\rangle^s}{\partial x} = \langle\eta\rangle^s, \tag{3.28}$$

form a 4×4 system with equations (3.23) and (3.26) in the unknowns $\langle u\rangle^s$, $\langle v\rangle^s$, $\langle w\rangle^s$ and $\langle\eta\rangle^s$.

3.2.3 Boundary and interface momentum transfer conditions

Once the equations in the new variables are obtained, the next step is to express the boundary conditions (3.8) and (3.9) in the same set of variable. At the solid walls the no-slip and no-penetration conditions hold. Condition (3.8b) remains unchanged, as follows

$$\langle v\rangle^s = 0. \tag{3.29}$$

At the walls, the streamwise and spanwise velocities, $\langle u\rangle^s$ and $\langle w\rangle^s$, are zero as their derivatives in the x and z directions. Therefore, using the continuity equations (3.7) and the definition of $\langle\eta\rangle^s$ (3.21), we obtain the following conditions at the walls

$$\frac{d\langle v\rangle^s}{dy} = 0, \tag{3.30}$$

$$\langle\eta\rangle^s = 0. \tag{3.31}$$

At each interface between the fluid region and the porous layers, the momentum transfer conditions (3.9) must be satisfied. The condition (3.9b) remains unchanged

$$v = \langle v\rangle^s, \tag{3.32}$$

while the other conditions need to be transformed. We begin by subtracting the x-derivative of the (3.9c) from the z-derivative of the (3.9a). We obtain

$$\frac{\partial u}{\partial z} - \frac{\partial w}{\partial x} = \frac{\partial\langle u\rangle^s}{\partial z} - \frac{\partial\langle w\rangle^s}{\partial x}, \tag{3.33}$$

which states that the normal vorticity at the interface is continuous, i.e.

$$\eta = \langle \eta \rangle^s. \tag{3.34}$$

Adding the z-derivative of the (3.9c) to the x-derivative of the (3.9a), gives

$$\frac{\partial u}{\partial x} + \frac{\partial w}{\partial z} = \frac{\partial \langle u \rangle^s}{\partial x} + \frac{\partial \langle w \rangle^s}{\partial z}. \tag{3.35}$$

Using the continuity equations (3.5) and (3.7), we obtain

$$\frac{\partial v}{\partial y} = \frac{\partial \langle v \rangle^s}{\partial y}, \tag{3.36}$$

which states that the normal derivative of the normal velocity is continuous at the interface. Next boundary condition is derived by subtracting the x-derivative of the (3.9f) from the z-derivative of the (3.9e). We have

$$\frac{\sigma}{\varepsilon} \frac{\partial^2 \langle u \rangle^s}{\partial y \partial z} - \sigma \frac{\partial^2 u}{\partial y \partial z} - \frac{\sigma}{\varepsilon} \frac{\partial^2 \langle w \rangle^s}{\partial y \partial x} + \sigma \frac{\partial^2 w}{\partial y \partial x} = \pm \tau \frac{\partial u}{\partial z} \mp \tau \frac{\partial w}{\partial x}, \tag{3.37}$$

which can be further simplified by using the definitions of the normal vorticity to

$$\frac{\sigma}{\varepsilon} \frac{\partial \langle \eta \rangle^s}{\partial y} - \sigma \frac{\partial \eta}{\partial y} = \pm \tau \eta. \tag{3.38}$$

Adding the x-derivative of the (3.9e) to the z-derivative of the (3.9f), we obtain

$$\frac{\sigma}{\varepsilon} \frac{\partial^2 \langle u \rangle^s}{\partial y \partial x} - \sigma \frac{\partial^2 u}{\partial y \partial x} + \frac{\sigma}{\varepsilon} \frac{\partial^2 \langle w \rangle^s}{\partial y \partial z} - \sigma \frac{\partial^2 w}{\partial y \partial z} = \pm \tau \frac{\partial u}{\partial x} \pm \tau \frac{\partial w}{\partial z}. \tag{3.39}$$

Using the continuity equations (3.5) and (3.7), we obtain

$$\frac{\sigma}{\varepsilon} \frac{\partial^2 \langle v \rangle^s}{\partial y^2} - \sigma \frac{\partial^2 v}{\partial y^2} = \pm \tau \frac{\partial v}{\partial y}. \tag{3.40}$$

In order to obtain the last interface condition, we sum the second x-derivative of (3.9d) to the second z-derivative of equation (3.9d). We have

$$\frac{\partial^2 p}{\partial x^2} + \frac{\partial^2 p}{\partial z^2} = \frac{\partial^2 \langle p \rangle^f}{\partial x^2} + \frac{\partial^2 \langle p \rangle^f}{\partial z^2}. \tag{3.41}$$

Then, we exploit Poisson's equations (3.17) and (3.25), to obtain

$$\frac{\partial^2 p}{\partial y^2} - \left(\frac{\partial HU}{\partial x} + \frac{\partial HV}{\partial y} + \frac{\partial HW}{\partial z} \right) = \frac{\partial^2 \langle p \rangle^f}{\partial y^2}. \tag{3.42}$$

To eliminate pressure from the above equations, we take the y-derivatives of equation (3.15)

$$\frac{\partial^2 p}{\partial y^2} = -\frac{\partial^2 v}{\partial t \partial y} + \frac{1}{\mathrm{Re}} \nabla^2 \frac{\partial v}{\partial y} + \frac{\partial HV}{\partial y}, \tag{3.43}$$

and the y-derivatives of equation (3.24)

$$\frac{\partial^2 \langle p \rangle^f}{\partial y^2} = -\frac{1}{\varepsilon} \frac{\partial^2 \langle v \rangle^s}{\partial t \partial y} + \frac{1}{\varepsilon \mathrm{Re}} \nabla^2 \frac{\partial \langle v \rangle^s}{\partial y} - \frac{1}{\sigma^2 \mathrm{Re}} \frac{\partial \langle v \rangle^s}{\partial y}. \tag{3.44}$$

Substituting (3.43) and (3.44) in (3.42), and using (3.36), we obtain

$$\begin{aligned} \left(1 - \frac{1}{\varepsilon}\right) \frac{\partial}{\partial t} \frac{\partial v}{\partial y} - \frac{1}{\mathrm{Re}} \left[\left(1 - \frac{1}{\varepsilon}\right) \left(\frac{\partial^2}{\partial x^2} + \frac{\partial^2}{\partial z^2} \right) \frac{\partial v}{\partial y} + \frac{\partial^3 v}{\partial y^3} - \frac{1}{\varepsilon} \frac{\partial^3 \langle v \rangle^s}{\partial y^3} \right] + \\ - \frac{1}{\sigma^2 \mathrm{Re}} \frac{\partial v}{\partial y} = - \left[\frac{\partial HU}{\partial x} + \frac{\partial HW}{\partial z} \right]. \end{aligned} \tag{3.45}$$

Finally, the the six interface conditions can be summarized as follows

$$v = \langle v \rangle^s, \tag{3.46a}$$

$$\eta = \langle \eta \rangle^s, \tag{3.46b}$$

$$\frac{\partial v}{\partial y} = \frac{\partial \langle v \rangle^s}{\partial y}, \tag{3.46c}$$

$$\frac{\sigma}{\varepsilon} \frac{\partial \langle \eta \rangle^s}{\partial y} - \sigma \frac{\partial \eta}{\partial y} = \pm\, \tau \eta, \tag{3.46d}$$

$$\frac{\sigma}{\varepsilon} \frac{\partial^2 \langle v \rangle^s}{\partial y^2} - \sigma \frac{\partial^2 v}{\partial y^2} = \pm\, \tau \frac{\partial v}{\partial y}, \tag{3.46e}$$

$$\begin{aligned} \left(1 - \frac{1}{\varepsilon}\right) \frac{\partial}{\partial t} \frac{\partial v}{\partial y} - \frac{1}{\mathrm{Re}} \left[\left(1 - \frac{1}{\varepsilon}\right) \left(\frac{\partial^2}{\partial x^2} + \frac{\partial^2}{\partial z^2} \right) \frac{\partial v}{\partial y} + \frac{\partial^3 v}{\partial y^3} - \frac{1}{\varepsilon} \frac{\partial^3 \langle v \rangle^s}{\partial y^3} \right] + \\ - \frac{1}{\sigma^2 \mathrm{Re}} \frac{\partial v}{\partial y} = - \left[\frac{\partial HU}{\partial x} + \frac{\partial HW}{\partial z} \right]. \end{aligned} \tag{3.46f}$$

Chapter 4

Direct Numerical Simulation

In this chapter we describe our implementation of a DNS solver for turbulent channel flows over porous layers. The program is an extension of an existing solver for channel flows created by Quadrio [26, 36, 34]. The chapter has two main parts. In the first section we discretize the equations derived in the previous chapter, while in the second section we validate our code.

4.1 Numerical procedure

In this section we present the discretized form of the evolution equations and boundary conditions. To compute the spatial derivatives in the streamwise and spanwise directions, we use a spectral method, while we use high-order compact finite difference approximation for the derivatives in the wall-normal direction. Time integration is performed using a semi-implicit method. In particular, the nonlinear terms are advanced with a third-order Runge-Kutta scheme, whereas the other terms are advanced using an implicit second-order Crank-Nicholson scheme.

4.1.1 Spectral discretization of the evolution equations

Spectral methods are used to numerically solve differential equations. The solution of a differential equation is written as the sum of the modes of certain basis functions, for example a Fourier series, and the solution is determined by choosing the coefficients in the sum appropriately.

We can use spectral methods to solve our problem, equations (3.14), (3.18), (3.19) and (3.20), and (3.23), (3.26), (3.27) and (3.28), because the fully developed turbulent channel flow is homogeneous in the streamwise and spanwise directions, and periodic boundary conditions are used in these directions. Therefore, we write the velocity component v and the vorticity component η as a truncated Fourier expansion along the x and z coordinates. The wall-normal velocity v and vorticity η can be expressed as

$$v\left(x,y,z,t\right)=\sum_{h=-\frac{n_x}{2}}^{\frac{n_x}{2}}\sum_{l=-\frac{n_z}{2}}^{\frac{n_z}{2}}\hat{v}_{hl}\left(y,t\right)e^{\mathrm{i}\alpha x}e^{\mathrm{i}\beta z}, \tag{4.1a}$$

$$\eta\left(x,y,z,t\right)=\sum_{h=-\frac{n_x}{2}}^{\frac{n_x}{2}}\sum_{l=-\frac{n_z}{2}}^{\frac{n_z}{2}}\hat{\eta}_{hl}\left(y,t\right)e^{\mathrm{i}\alpha x}e^{\mathrm{i}\beta z}, \tag{4.1b}$$

and the wall-normal volume-averged velocity $\langle v\rangle^s$ and vorticity $\langle \eta\rangle^s$ becomes

$$\langle v\rangle^s\left(x,y,z,t\right)=\sum_{h=-\frac{n_x}{2}}^{\frac{n_x}{2}}\sum_{l=-\frac{n_z}{2}}^{\frac{n_z}{2}}\hat{v}^p_{hl}\left(y,t\right)e^{\mathrm{i}\alpha x}e^{\mathrm{i}\beta z}, \tag{4.2a}$$

$$\langle \eta\rangle^s\left(x,y,z,t\right)=\sum_{h=-\frac{n_x}{2}}^{\frac{n_x}{2}}\sum_{l=-\frac{n_z}{2}}^{\frac{n_z}{2}}\hat{\eta}^p_{hl}\left(y,t\right)e^{\mathrm{i}\alpha x}e^{\mathrm{i}\beta z}, \tag{4.2b}$$

where

$$\alpha=\frac{2\pi h}{L_x}=\alpha_0 h, \qquad \beta=\frac{2\pi l}{L_z}=\beta_0 l. \tag{4.3}$$

The fundamental wavenumbers α_0 and β_0, and the indexes h and l, correspond to the streamwise and spanwise directions, respectively. The length, L_x, and width, L_z, of the computational domain, and the associated number of modes, n_x and n_z, must be chosen in order to minimize computational errors. In particular, the computational domain must be large enough to resolve the largest scales of the turbulent flow, while the grid resolutions $\Delta_x = L_x/2n_x$ and $\Delta_z = L_z/2n_z$, must be small enough to resolve the smallest scales.

The Fourier representations of v, η, $\langle v\rangle^s$ and $\langle\eta\rangle^s$ are substituted into evolution equations (3.14) and (3.18)-(3.20), and (3.23) and (3.26)-(3.28). After a simple manipulation the evolution equations for each Fourier mode are

$$\begin{aligned}\frac{\partial}{\partial t}\left(D_2\hat{v}_{hl}-k^2\hat{v}_{hl}\right)=\frac{1}{\mathrm{Re}}\left(D_4\hat{v}_{hl}-2k^2D_2\hat{v}_{hl}+k^4\hat{v}_{hl}\right)+&\\ -k^2\widehat{HV}_{hl}-D_1\left(i\alpha\widehat{HU}_{hl}+i\beta\widehat{HW}_{hl}\right),&\end{aligned} \tag{4.4}$$

$$\frac{\partial\hat{\eta}_{hl}}{\partial t}=\frac{1}{\mathrm{Re}}\left(D_2\hat{\eta}_{hl}-k^2\hat{\eta}_{hl}\right)+i\beta\widehat{HU}_{hl}-i\alpha\widehat{HW}_{hl}, \tag{4.5}$$

$$\hat{u}_{hl}=\frac{\mathrm{i}}{k^2}\left(\alpha D_1\hat{v}_{hl}-\beta\hat{\eta}_{hl}\right), \tag{4.6}$$

$$\hat{w}_{hl}=\frac{\mathrm{i}}{k^2}\left(\beta D_1\hat{v}_{hl}+\alpha\hat{\eta}_{hl}\right), \tag{4.7}$$

while the evolution equations for the fluid motion in the porous region become

$$\frac{\partial}{\partial t}\left(D_2\hat{v}^p_{hl} - k^2\hat{v}^p_{hl}\right) = \frac{1}{\mathrm{Re}}\left(D_4\hat{v}^p_{hl} - 2k^2 D_2\hat{v}^p_{hl} + k^4\hat{v}^p_{hl}\right) - \frac{\varepsilon}{\sigma^2 Re}\left(D_2\hat{v}^p_{hl} - k^2\hat{v}^p_{hl}\right), \tag{4.8}$$

$$\frac{\partial\hat{\eta}^p_{hl}}{\partial t} = \frac{1}{Re}\left(D_2\hat{\eta}^p_{hl} - k^2\hat{\eta}^p_{hl}\right) - \frac{\varepsilon}{\sigma^2\mathrm{Re}}\hat{\eta}^p_{hl}, \tag{4.9}$$

$$\hat{u}^p_{hl} = \frac{\mathrm{i}}{k^2}\left(\alpha D_1\hat{v}^p_{hl} - \beta\hat{\eta}^p_{hl}\right), \tag{4.10}$$

$$\hat{w}^p_{hl} = \frac{\mathrm{i}}{k^2}\left(\beta D_1\hat{v}^p_{hl} + \alpha\hat{\eta}^p_{hl}\right). \tag{4.11}$$

In the above equations we have introduced the wall-normal derivative operator of order n, D_n, and the wave vector $\boldsymbol{k}$, whose magnitude is

$$k = \sqrt{\alpha^2 + \beta^2}. \tag{4.12}$$

Moreover, $\widehat{HU}_{hl}$, $\widehat{HV}_{hl}$ and $\widehat{HW}_{hl}$ are the convolution terms representing in Fourier-space the nonlinear terms (3.12), (3.16) and (3.13) of Navier-Stokes equations. The numerical evaluation of the convolution of N modes, i.e. the computation of all the so-called triadic interactions, requires a number of operations of order N^2. To reduce this computational cost, the nonlinear terms are evaluated in physical space and then transformed back to Fourier space. This procedure, when Fast Fourier Transform (FFT) algorithm is used, requires a number of operations of the order of $N \log N$. Note that aliasing errors are avoided by increasing the number of modes by a factor of at least $3/2$ before the inverse Fourier transforms.

At solid walls, the wall-normal volume-averaged velocity and vorticity satisfy no-penetration and no-slip conditions written in Fourier space as

$$\hat{v}^p_{hl} = 0, \tag{4.13a}$$

$$D_1\hat{v}^p_{hl} = 0, \tag{4.13b}$$

$$\hat{\eta}^s_{hl} = 0, \tag{4.13c}$$

while at the interface with the fluid region, momentum transfer conditions must be satisfied

$$\hat{v}_{hl} = \hat{v}^p_{hl}, \tag{4.14a}$$

$$\hat{\eta}_{hl} = \hat{\eta}^p_{hl}, \tag{4.14b}$$

$$D_1\hat{v}_{hl} = D_1\hat{v}^p_{hl}, \tag{4.14c}$$

$$\frac{\sigma}{\varepsilon}D_1\hat{\eta}^p_{hl} - \sigma D_1\hat{\eta}_{hl} = \pm\,\tau\hat{\eta}_{hl}, \tag{4.14d}$$

$$\frac{\sigma}{\varepsilon}D_2\hat{v}^p_{hl} - \sigma D_2\hat{v}_{hl} = \pm\,\tau D_1\hat{v}_{hl}, \tag{4.14e}$$

$$\begin{aligned}\left(1-\frac{1}{\varepsilon}\right)\frac{\partial}{\partial t}D_1\hat{v}_{hl}-\frac{1}{\mathrm{Re}}\left[-k^2\left(1-\frac{1}{\varepsilon}\right)D_1\hat{v}_{hl}+D_3\hat{v}_{hl}-\frac{1}{\varepsilon}D_3\hat{v}^p_{hl}\right]+\\ -\frac{1}{\sigma^2\mathrm{Re}}D_1\hat{v}_{hl}=-\left[\mathrm{i}\alpha\widehat{HU}_{hl}+\mathrm{i}\beta\widehat{HW}_{hl}\right].\end{aligned} \tag{4.14f}$$

4.1.2 Space discretization

Finite difference schemes can be explicit or implicit. Explicit schemes express the nodal derivatives as a weighted sum of the nodal values of the function, while implicit schemes equate a weighted sum of the nodal derivatives to a weighted sum of the function. Compact schemes are considered implicit schemes because they typically require the inversion of a linear system to compute a derivative. Implicit schemes are generally more accurate than explicit schemes with the same stencil width. This increase in accuracy is achieved at the cost of inverting a banded matrix to obtain the nodal derivatives. The most popular implicit schemes are the Padé schemes, which are based on Padé's approximants.

In this section, we use a finite difference fourth-order compact schemes for the discretization of the wall-normal derivatives in the evolution equations (4.4)-(4.11). The computational stencil is composed by five grid points, arbitrarily spaced but with smooth stretching [22, 27]. Note that we are able to use a fourth-order compact scheme at the cost of an explicit scheme, because of the absence of the third derivative operator, D_3, in the equations of motion. For details, the reader is referred to Thomas work on the numerical solution of the Orr-Sommerfeld equations [47].

We indicate with $d_n^j\left(i\right), i=-2,\ldots,2$ the five coefficients used to approximate the exact n-th operator D_n over five adjacent grid points, centered at y_j, as follows

$$D_n f\left(y\right)|_{y=y_j}=\sum_{i=-2}^{2}d_n^j\left(i\right)f\left(y_{j+i}\right). \tag{4.15}$$

To obtain the coefficients d_n^j of the finite difference formula (4.15), we choose a set t_m of polynomials of y of increasing degree

$$t_m\left(y\right)=y^m,\quad m=0,1,2,\ldots,8 \tag{4.16}$$

and calculate analytically their derivatives $D_4 t_m$. Then, we obtain the required coefficients imposing that the following discrete equations are satisfied,

$$d_4 t_m-d_0\left(D_4 t_m\right)=0,\quad m=0,1,2,\ldots,8. \tag{4.17}$$

Since our computational stencil contains 5 grid points, the unknown coefficients d_0 and d_4 are 10. The last condition, the tenth, is the normalization condition

$$\sum_{i=-2}^{2}d_0\left(i\right)=1. \tag{4.18}$$

Equations (4.17) and (4.18) form a 10×10 linear system for the unknown coefficients d_0 and d_4. Note that $D_4 t_m = 0$ for $m < 4$. Therefore, it is possible to split the 10×10 system into two 5×5 sub-systems, one for d_0 and one for d_4. The coefficients of the derivatives of lesser degree, d_1 and d_2, are derived similarly and determined by solving two 5×5 linear systems. All the differential operators admit a representation in which d_0 remains the same, so it can be computed just one time. The procedure outlined above should be repeated for the whole y range, from one wall to the other. This requires a negligible amount of computing time, because it has to be done only at the beginning of a computation. This technique let us obtain finite difference discretization which is uniformly fourth-order accurate. To impose the boundary conditions we need to use not centered stencils at the boundaries. To determine their coefficients, we can follow an approach similar to the one used for the centered stencil at the interior points of the domain, therefore preserving the fourth-order accuracy of the method.

We use a mesh of variable size in the wall-normal direction, with more grid points near the boundaries and the interfaces than in the center. The grid points y_j in the fluid region of the channel are constructed as follows

$$y_j = -1 + \left[\frac{\tanh\left(a \frac{2j}{n_y - 1}\right)}{\tanh(a)} + 1 \right] \quad j = -1, \ldots, n_y + 1, \tag{4.19}$$

while the grid points in the upper and lower porous layers, respectively, are constructed as follows

$$y_j^p = 1 + h_p \left[\frac{\tanh\left(a \frac{2j}{n_y^p - 1}\right)}{\tanh(a)} + 1 \right] \quad j = -1, \ldots, n_y^p + 1, \tag{4.20}$$

$$y_j^p = -1 - 2h_p + h_p \left[\frac{\tanh\left(a \frac{2j}{n_y^p - 1}\right)}{\tanh(a)} + 1 \right] \quad j = -1, \ldots, n_y^p + 1. \tag{4.21}$$

In the above expressions a is a parameter, which determines the amount of stretching of the mesh in the wall-normal direction, and n_y and n_y^p are the number of grid points in the fluid region and in the porous layers, respectively. The nodes identified by indexes -1 and $n_y + 1$ are called ghost nodes. We introduce these nodes to impose the boundary conditions (4.13a) and (4.13b) at each wall, and the momentum transfer conditions, (4.14a), (4.14c), (4.14e) and (4.14f), at each interface. Note that the use of ghost nodes implies a supplementary condition for $\hat{\eta}$ at each boundaries

$$D_4 \left(\hat{\eta}_{hl}\right)|_{y_j} = 0, \quad j = 1, n_y - 1 \tag{4.22}$$

$$D_4 \left(\hat{\eta}_{hl}^p\right)|_{y_j} = 0, \quad j = 1, n_y^p - 1 \tag{4.23}$$

These conditions are consequence of the cubic extrapolations used to obtain the values $\hat{\eta}_{hl}$ and $\hat{\eta}^p_{hl}$ at the ghost nodes.

The space discretization described above is used to discretize the evolution equations (4.4)-(4.7) in the fluid region as follows

$$\begin{aligned}\frac{\partial}{\partial t}\left(d_2^j\hat{v}_{hl} - k^2 d_0^j\hat{v}_{hl}\right) = \frac{1}{\mathrm{Re}}\left(d_4^j\hat{v}_{hl} - 2k^2 d_2^j\hat{v}_{hl} + k^4 d_0^j\hat{v}_{hl}\right) + \\ -k^2 d_0^j\widehat{HV}_{hl} - d_1^j\left(\mathrm{i}\alpha\widehat{HU}_{hl} + \mathrm{i}\beta\widehat{HW}_{hl}\right),\end{aligned} \tag{4.24}$$

$$\frac{\partial d_0^j\hat{\eta}_{hl}}{\partial t} = \frac{1}{\mathrm{Re}}\left(d_2^j\hat{\eta}_{hl} - k^2 d_0^j\hat{\eta}_{hl}\right) + \mathrm{i}d_0^j\beta\widehat{HU}_{hl} - \mathrm{i}d_0^j\alpha\widehat{HW}_{hl}, \tag{4.25}$$

$$d_0^j\hat{u}_{hl} = \frac{\mathrm{i}}{k^2}\left(\alpha d_1^j\hat{v}_{hl} - \beta d_0^j\hat{\eta}_{hl}\right), \tag{4.26}$$

$$d_0^j\hat{w}_{hl} = \frac{\mathrm{i}}{k^2}\left(\beta d_1^j\hat{v}_{hl} + \alpha d_0^j\hat{\eta}_{hl}\right), \tag{4.27}$$

where $j = 1, \dots, n_y - 1$, while the evolution equations (4.8)-(4.11) in the porous region become

$$\begin{aligned}\frac{\partial}{\partial t}\left(d_2^j\hat{v}^p_{hl} - k^2 d_0^j\hat{v}^p_{hl}\right) = \frac{1}{\mathrm{Re}}\left(d_4^j\hat{v}^p_{hl} - 2k^2 d_2^j\hat{v}^p_{hl} + k^4 d_0^j\hat{v}^p_{hl}\right) + \\ -\frac{\varepsilon}{\sigma^2\mathrm{Re}}\left(d_2^j\hat{v}^p_{hl} - k^2 d_0^j\hat{v}^p_{hl}\right),\end{aligned} \tag{4.28}$$

$$\frac{\partial d_0^j\hat{\eta}^p_{hl}}{\partial t} = \frac{1}{\mathrm{Re}}\left(d_2^j\hat{\eta}^p_{hl} - k^2 d_0^j\hat{\eta}^p_{hl}\right) - \frac{\varepsilon}{\sigma^2\mathrm{Re}} d_0^j\hat{\eta}^p_{hl}, \tag{4.29}$$

$$d_0^j\hat{u}^p_{hl} = \frac{\mathrm{i}}{k^2}\left(\alpha d_1^j\hat{v}^p_{hl} - \beta d_0^j\hat{\eta}^p_{hl}\right), \tag{4.30}$$

$$d_0^j\hat{w}^p_{hl} = \frac{\mathrm{i}}{k^2}\left(\beta d_1^j\hat{v}^p_{hl} + \alpha d_0^j\hat{\eta}^p_{hl}\right), \tag{4.31}$$

where $j = 1, \dots, n_y^p - 1$.

At the solid walls, the no-penetration and no-slip conditions (4.13) become

$$d_0^j\hat{v}^p_{hl} = 0, \tag{4.32a}$$

$$d_1^j\hat{v}^p_{hl} = 0, \tag{4.32b}$$

$$d_0^j\hat{\eta}^s_{hl} = 0, \tag{4.32c}$$

where j is equal to zero at the lower wall and $j = n_y^p$ at the upper wall. The momentum transfer conditions (4.14) become

$$d_0^j\hat{v}_{hl} = d_0^{j^p}\hat{v}^p_{hl}, \tag{4.33a}$$

$$d_0^j\hat{\eta}_{hl} = d_0^{j^p}\hat{\eta}^p_{hl}, \tag{4.33b}$$

$$d_1^j\hat{v}_{hl} = d_1^{j^p}\hat{v}^p_{hl}, \tag{4.33c}$$

$$\frac{\sigma}{\varepsilon}d_1^{j^p}\hat{\eta}^p_{hl} - \sigma d_1^j\hat{\eta}_{hl} = \pm\,\tau d_0^j\hat{\eta}_{hl}, \tag{4.33d}$$

$$\frac{\sigma}{\varepsilon}d_2^{j^p}\hat{v}^p_{hl} - \sigma d_2^j\hat{v}_{hl} = \pm\,\tau d_1^j\hat{v}_{hl}, \tag{4.33e}$$

$$\begin{aligned}\left(1-\frac{1}{\varepsilon}\right)\frac{\partial}{\partial t}d_1^j\hat{v}_{hl}-\frac{1}{\mathrm{Re}}\left[-k^2\left(1-\frac{1}{\varepsilon}\right)d_1^j\hat{v}_{hl}+d_3^j\hat{v}_{hl}-\frac{1}{\varepsilon}d_3^{j^p}\hat{v}^p_{hl}\right]+\\ -\frac{1}{\sigma^2\mathrm{Re}}d_1^j\hat{v}_{hl}=-d_0^j\left[\mathrm{i}\alpha\widehat{HU}_{hl}+\mathrm{i}\beta\widehat{HW}_{hl}\right],\end{aligned} \tag{4.33f}$$

where $j=0$ and $j^p=ny_p$ at the lower interface, while $j=n_y$ and $j^p=0$ at the upper interface. Moreover, the conditions (4.22) for the ghost nodes become

$$d_4^j\hat{v}_{hl}=0, \tag{4.34}$$

$$d_4^{j^p}\hat{v}_{hl}=0, \tag{4.35}$$

where $j^p=1$ at the lower solid wall, $j^p=n_y^p-1$ and $j=1$ at the lower interface, $j=n_y-1$ and $j^p=1$ at the upper interface, and $j^p=n_y^p-1$ at the upper solid wall.

4.1.3 Time discretization

To integrate in time the evolutions equations (4.24)-(4.31), we adopt a semi-implicit method. The nonlinear terms are advanced with a third-order Runge-Kutta scheme, whereas we use an implicit second-order Crank-Nicholson scheme for the others terms [29, 44, 13].

Before time integration, the evolution equations in the fluid region (4.4)-(4.7) are fully coupled. In the porous regions, however, equations (4.8) and (4.9) are uncoupled from equations (4.10) and (4.11). When nonlinear terms in equations (4.4) and (4.5) are treated explicitly, the equations for $\hat{v}$ (4.4) and $\hat{\eta}$ (4.5) uncouple from the one for $\hat{u}$ (4.6) and $\hat{w}$ (4.7). At this point, the full set of equations (4.4)-(4.11) can be integrated in two steps. First, we compute $\hat{v}$ and $\hat{\eta}$ integrating equations (4.4) and (4.5), and $\hat{v}^p$ and $\hat{\eta}^p$ integrating equations (4.8) and (4.9). Subsequently, we compute $\hat{u}$ and $\hat{w}$ using equations (4.6) and (4.7), and $\hat{u}^p$ and $\hat{w}^p$ using equations (4.10) and (4.11).

After time discretization, the evolution equations (4.24) and (4.25) can be rewritten as follows

$$\begin{aligned}&\left[\frac{\lambda_s}{\Delta t}\left(d_2^j\hat{v}-k^2d_0^j\hat{v}\right)-\frac{1}{\mathrm{Re}}\left(d_4^j\hat{v}-2k^2d_2^j\hat{v}+k^4d_0^j\hat{v}\right)\right]^{n_{s+1}}=\\ &=\left[\frac{\lambda_s}{\Delta t}\left(d_2^j\hat{v}-k^2d_0^j\hat{v}\right)+\frac{1}{\mathrm{Re}}\left(d_4^j\hat{v}-2k^2d_2^j\hat{v}+k^4d_0^j\hat{v}\right)\right]^{n_s}+\\ &\qquad+\theta_s\left[-k^2d_0^j\widehat{HV}-d_1^j\left(\mathrm{i}\alpha\widehat{HU}+\mathrm{i}\beta\widehat{HW}\right)\right]^{n_s}+\\ &\qquad+\xi_s\left[-k^2d_0^j\widehat{HV}-d_1^j\left(\mathrm{i}\alpha\widehat{HU}+\mathrm{i}\beta\widehat{HW}\right)\right]^{n_{s-1}},\end{aligned} \tag{4.36}$$

$$\begin{aligned}\left[\frac{\lambda_s}{\Delta t}d_0^j\hat{\eta}-\frac{1}{\mathrm{Re}}\left(d_2^j\hat{\eta}-k^2d_0^j\hat{\eta}\right)\right]^{n_{s+1}}=\left[\frac{\lambda_s}{\Delta t}d_0^j\hat{\eta}+\frac{1}{\mathrm{Re}}\left(d_2^j\hat{\eta}-k^2d_0^j\hat{\eta}\right)\right]^{n_s}+\\ +\theta_s\left[\mathrm{i}\beta d_0^j\widehat{HU}-\mathrm{i}\alpha d_0^j\widehat{HW}\right]^{n_s}+\xi_s\left[\mathrm{i}\beta d_0^j\widehat{HU}-\mathrm{i}\alpha d_0^j\widehat{HW}\right]^{n_{s-1}},\end{aligned} \tag{4.37}$$

while equations (4.28) and (4.29) become

$$
\begin{aligned}
&\left[\frac{\lambda_s}{\Delta t}\left(d_2^j\hat{v}^p - k^2 d_0^j\hat{v}^p\right) - \frac{1}{\mathrm{Re}}\left(d_4^j\hat{v}^p - 2k^2 d_2^j\hat{v}^p + k^4 d_0^j\hat{v}^p\right)\right]^{n_{s+1}} + \\
&\qquad + \left[\frac{\varepsilon}{\sigma^2\mathrm{Re}}\left(d_2^j\hat{v}^p - k^2 d_0^j\hat{v}^p\right)\right]^{n_{s+1}} = \\
&= \left[\frac{\lambda_s}{\Delta t}\left(d_2^j\hat{v}^p - k^2 d_0^j\hat{v}^p\right) + \frac{1}{Re}\left(d_4^j\hat{v}^p - 2k^2 d_2^j\hat{v}^p + k^4 d_0^j\hat{v}^p\right)\right]^{n_s} + \\
&\qquad - \left[\frac{\varepsilon}{\sigma^2\mathrm{Re}}\left(d_2^j\hat{v}^p - k^2 d_0^j\hat{v}^p\right)\right]^{n_s},
\end{aligned}
\tag{4.38}
$$

$$
\begin{aligned}
&\left[\frac{\lambda_s}{\Delta t}d_0^j\hat{\eta}^p - \frac{1}{\mathrm{Re}}\left(d_2^j\hat{\eta}^p - k^2 d_0^j\hat{\eta}^p - \frac{\varepsilon}{\sigma^2}d_0^j\hat{\eta}^p\right)\right]^{n_{s+1}} = \\
&= \left[\frac{\lambda_s}{\Delta t}d_0^j\hat{\eta}^p + \frac{1}{\mathrm{Re}}\left(d_2^j\hat{\eta}^p - k^2 d_0^j\hat{\eta}^p - \frac{\varepsilon}{\sigma^2}d_0^j\hat{\eta}^p\right)\right]^{n_s},
\end{aligned}
\tag{4.39}
$$

where Δt is the time-step, n_s the index of the discretized time and λ_s, θ_s and ξ_s are three coefficients of the combined third-order Runge-Kutta and Cranck-Nicholson scheme, whose values are reported in table 4.1. The subscript s indicates the substeps used in the combined Runge-Kutta and Cranck-Nicholson scheme to advance the integration from time istant t_n to the time istant $t_{n+1} = t_n + \Delta t$. In the first substep $s = 1$, we integrate equations (4.36)-(4.39) from $t_{n_1} = t_n$ to $t_{n_2} = t_1 + 2/\lambda_1 \Delta t$. In the second substep $s = 2$, we integrate equations (4.36)-(4.39) from t_{n_2} to $t_{n_3} = t_{n_2} + 2/\lambda_2 \Delta t$. Finally, in the third substep $s = 3$, we integrate equations (4.36)-(4.39) from t_{n_3} to $t_{n_4} = t_{n_3} + 2/\lambda_3 \Delta t = t_{n+1}$. Note that, in the first substep $\xi_1 = 0$ so we do not need to define n_0.

The boundary conditions (4.13) and momentum transfer conditions (4.14), except (4.14f), remain unchanged after time discretization. The condition (4.14f),

substep	λ_s	θ_s	ξ_s
1	120/32	2	0
2	120/8	50/8	-34/8
3	120/20	90/20	-50/20

Table 4.1: Coefficients for time integrations of evolution equations (4.36), (4.37), (4.38) and (4.39) with an implicit second-order Crank-Nicholson and a third-order Runge-Kutta schemes.

which is time-dependent, becomes

$$\begin{aligned}
&\left[\left(1-\frac{1}{\epsilon}\right)\frac{\lambda_s}{\Delta t}D_1\hat{v}_{hl}+\frac{k^2}{Re}\left(1-\frac{1}{\epsilon}\right)D_1\hat{v}_{hl}-\frac{1}{\sigma^2 Re}D_1\hat{v}_{hl}\right]^{n_{s+1}}=\\
&\left[\left(1-\frac{1}{\epsilon}\right)\frac{\lambda_s}{\Delta t}D_1\hat{v}_{hl}-\frac{k^2}{Re}\left(1-\frac{1}{\epsilon}\right)D_1\hat{v}_{hl}+\frac{1}{\sigma^2 Re}D_1\hat{v}_{hl}\right]^{n_s}+\\
&+\theta_s\left[\frac{1}{Re}\left(D_3\hat{v}_{hl}-\frac{1}{\epsilon}D_3\hat{v}^p_{hl}\right)-\left(\mathrm{i}\alpha\widehat{HU}_{hl}+\mathrm{i}\beta\widehat{HW}_{hl}\right)\right]^{n_s}+\\
&+\xi_s\left[\frac{1}{Re}\left(D_3\hat{v}_{hl}-\frac{1}{\epsilon}D_3\hat{v}^p_{hl}\right)-\left(\mathrm{i}\alpha\widehat{HU}_{hl}+\mathrm{i}\beta\widehat{HW}_{hl}\right)\right]^{n_{s-1}}.
\end{aligned} \tag{4.40}$$

In our numerical simulations, the time step Δt is an important parameter, because the time-integration scheme described above is not unconditionally stable. At each time step, a suitable Δt is computed imposing the following CFL condition

$$\Delta t=\frac{\max\limits_{\Omega}(\mathrm{CFL})}{\max\limits_{\Omega}\left(\frac{u}{\Delta x}\right)+\max\limits_{\Omega}\left(\frac{v}{\Delta y}\right)+\max\limits_{\Omega}\left(\frac{w}{\Delta z}\right)}, \tag{4.41}$$

where Ω is the computational domain.

4.1.4 Mean flow in the homogeneous directions

The equations (4.6) and (4.7) are singular when $k^2 = 0$. In order to compute the velocity components corresponding to the mode $k=\sqrt{\alpha^2+\beta^2}=0$, $(\alpha=0,\beta=0)$, we have to introduce the plane-average values of the velocity $\tilde{u}$ and $\tilde{w}$, as follows

$$\tilde{u}(y,t)=\frac{1}{L_x}\frac{1}{L_z}\int_0^{L_x}\int_0^{L_z}u(x,y,z,t)\,dx\,dz, \tag{4.42}$$

$$\tilde{w}(y,t)=\frac{1}{L_x}\frac{1}{L_z}\int_0^{L_x}\int_0^{L_z}w(x,y,z,t)\,dx\,dz. \tag{4.43}$$

The plane-averaged velocities $\tilde{u}$ and $\tilde{w}$ are functions of the wall-normal coordinate and time only, and they are the Fourier modes for $k = 0$. The temporal average of $\tilde{u}$ and $\tilde{w}$ are the streamwise and spanwise mean velocities.

The calculation of $\tilde{u}$ and $\tilde{w}$ requires two additional equations that can be obtained by applying the plane-average operator, used in (4.43) and (4.43), to the x and z components of the momentum equations (3.4) and (3.6). The evolution equations for the plane-averaged velocities in the fluid region are

$$\frac{\partial\tilde{u}}{\partial t}=\frac{1}{\mathrm{Re}}D_2\tilde{u}-D_1\widetilde{uv}+\tilde{f}_x, \tag{4.44}$$

$$\frac{\partial\tilde{w}}{\partial t}=\frac{1}{\mathrm{Re}}D_2\tilde{w}-D_1\widetilde{vw}+\tilde{f}_z, \tag{4.45}$$

while their counterpart in the the porous region are

$$\frac{\partial \tilde{u}^p}{\partial t} = \frac{1}{\mathrm{Re}} D_2 \tilde{u}^p - \frac{\varepsilon}{\sigma^2 Re} \tilde{u}^p + \varepsilon \tilde{f}_x, \tag{4.46}$$

$$\frac{\partial \tilde{w}^p}{\partial t} = \frac{1}{\mathrm{Re}} D_2 \tilde{w}^p - \frac{\varepsilon}{\sigma^2 Re} \tilde{w}^p + \varepsilon \tilde{f}_z, \tag{4.47}$$

where $\tilde{f}_x$ and $\tilde{f}_z$ are the forcing terms and correspond to the mean pressure gradients. The discretized version of equations (4.44) and (4.45) are

$$\begin{aligned}\left[\frac{\lambda_s}{\Delta t} d_0^j \tilde{u} - \frac{1}{\mathrm{Re}} d_2^j \tilde{u}\right]^{n_s+1} &= \left[\frac{\lambda_s}{\Delta t} d_0^j \tilde{u} + \frac{1}{\mathrm{Re}} d_2^j \tilde{u}\right]^{n_s} + \\ &-\theta_s \left[d_1^j \widetilde{uv}\right]^{n_s} - \xi_s \left[d_1^j \widetilde{uv}\right]^{n_s-1} + \tilde{f}_x,\end{aligned} \tag{4.48}$$

$$\begin{aligned}\left[\frac{\lambda_s}{\Delta t} d_0^j \tilde{w} - \frac{1}{\mathrm{Re}} d_2^j \tilde{w}\right]^{n_s+1} &= \left[\frac{\lambda_s}{\Delta t} d_0^j \tilde{w} + \frac{1}{\mathrm{Re}} d_2^j \tilde{w}\right]^{n_s} + \\ &-\theta_s \left[d_1^j \widetilde{vw}\right]^{n_s} - \xi_s \left[d_1^j \widetilde{vw}\right]^{n_s-1} + \tilde{f}_z,\end{aligned} \tag{4.49}$$

while the discretized version of equations (4.46) and (4.47) are

$$\begin{aligned}\left[\frac{\lambda_s}{\Delta t} d_0^j \tilde{u}^p - \frac{1}{\mathrm{Re}} d_2^j \tilde{u}^p + \frac{\varepsilon}{\sigma^2 \mathrm{Re}} d_0^j \tilde{u}^p\right]^{n_s+1} &= \left[\frac{\lambda_s}{\Delta t} d_0^j \tilde{u}^p + \frac{1}{\mathrm{Re}} d_2^j \tilde{u}^p - \frac{\varepsilon}{\sigma^2 \mathrm{Re}} d_0^j \tilde{u}^p\right]^{n_s} + \\ &+\varepsilon \tilde{f}_x,\end{aligned} \tag{4.50}$$

$$\begin{aligned}\left[\frac{\lambda_s}{\Delta t} d_0^j \tilde{w}^p - \frac{1}{\mathrm{Re}} d_2^j \tilde{w}^p + \frac{\varepsilon}{\sigma^2 \mathrm{Re}} d_0^j \tilde{w}^p\right]^{n_s+1} &= \left[\frac{\lambda_s}{\Delta t} d_0^j \tilde{w}^p + \frac{1}{\mathrm{Re}} d_2^j \tilde{w}^p - \frac{\varepsilon}{\sigma^2 \mathrm{Re}} d_0^j \tilde{w}^p\right]^{n_s} + \\ &+\varepsilon \tilde{f}_z.\end{aligned} \tag{4.51}$$

The flow rates in the spanwise and streamwise directions per unit lengths are

$$Q_x = \int_{-1-2h_1}^{-1} \tilde{u}^p \, dy + \int_{-1}^{1} \tilde{u} \, dy + \int_{1}^{1+2h_2} \tilde{u}^p \, dy, \tag{4.52}$$

$$Q_z = \int_{-1-2h_1}^{-1} \tilde{w}^p \, dy + \int_{-1}^{1} \tilde{w} \, dy + \int_{1}^{1+2h_2} \tilde{w}^p \, dy. \tag{4.53}$$

In general, in the case of a turbulent flow, when one of the pressure gradients, $\tilde{f}_x$ or $\tilde{f}_z$, is constant, the flow rate in the same direction oscillates in time around a constant value, while, when one of the flow rates, Q_x or Q_z, is constant, the pressure gradient in the same direction oscillates around a constant value. If we want to perform a simulation at constant flow rate, $\overline{Q}_x$, we need to determine the appropriate forcing term at every time step. However this can be avoided with the following procedure. We first solve the equations (4.48) and (4.50) with zero forcing terms, $f_x = 0$, and we compute the flow rate $Q_x|_{f_x=0}$. Then, we solve the same equations (4.48) and (4.48), but with the RHS composed only by unit forcing terms, $f_x = 1$, and we compute the flow rate $Q_x|_{f_x=1}$. Finally, we combine the two solutions as follows

$$\tilde{u} = \tilde{u}|_{f_x=0} + \frac{\bar{Q}_x - Q_x|_{f_x=0}}{Q_x|_{f_x=1}} \tilde{u}|_{f_x=1}, \tag{4.54}$$

$$\tilde{u}^p = \tilde{u}^p|_{f_x=0} + \frac{\bar{Q}_x - Q_x|_{f_x=0}}{Q_x|_{f_x=1}} \tilde{u}^p|_{f_x=1}, \tag{4.55}$$

where $\bar{Q}_x$ is the imposed flow rate.

4.1.5 Numerical implementation

The program is written in `CPL`, a programming language created by Paolo Luchini. The `CPL` compiler preprocesses the source code to generate an `ANSI-C` source, which is then compiled by any `ANSI-C` compliant compiler. The invocation of a `make`-like command makes this procedure automatic. Figure 4.1 shows a flowchart of the DNS algorithm.

4.2 Code validation

In this section we validate our program. In order to do that, we first define the kinetic energy of the disturbances, and then we compare the computed growth rate of this quantity, with the one predicted by the linear stability analysis.

The kinetic energy of the disturbance per unit volume is defined as follows

$$E(t) = \sum_{\alpha,\beta} \frac{1}{2} \int_{h_l}^{h_u} |\hat{u}|^2 + |\hat{v}|^2 + |\hat{w}|^2 \, dy. \tag{4.56}$$

When we consider wavelike velocity perturbation of the following form

$$\hat{\boldsymbol{u}}(x, y, z, t) = \tilde{\boldsymbol{u}}(y) \, e^{\mathrm{i}(\alpha x + \beta z - \alpha c t)}, \tag{4.57}$$

where $c = c_r + \mathrm{i} c_i$ is the complex streamwise phase speed, and α and β are the streamwise and spanwise wavenumbers, the temporal linear stability theory predict that the energy of the disturbances has an exponential growth, as follows

$$e^{2\alpha c_i t}. \tag{4.58}$$

Tilton [48, 50] was the first to perform the linear stability analysis for a channel flow over permeable walls and Scarselli [41] further develops this work. For further details, the reader is referred to their works.

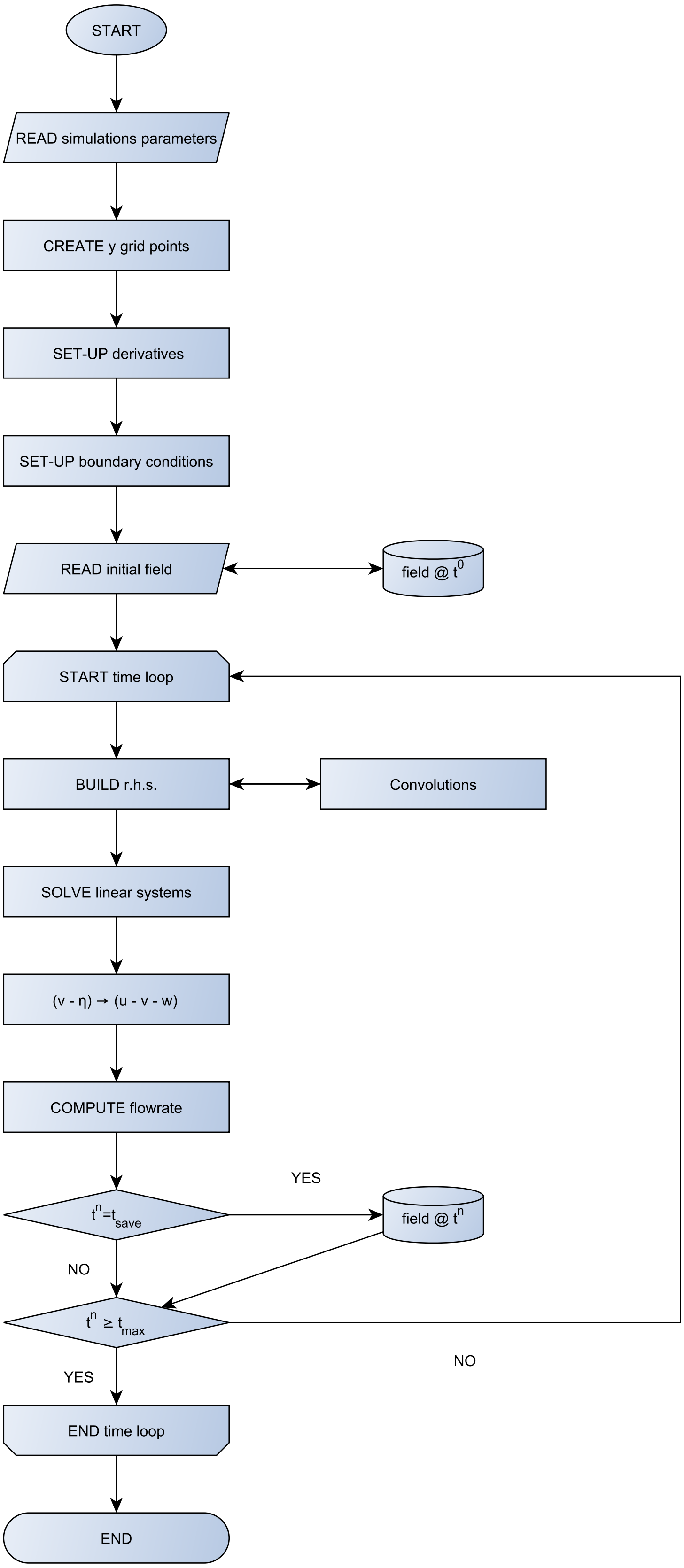

FIGURE 4.1: Flowchart representing the DNS algorithm.

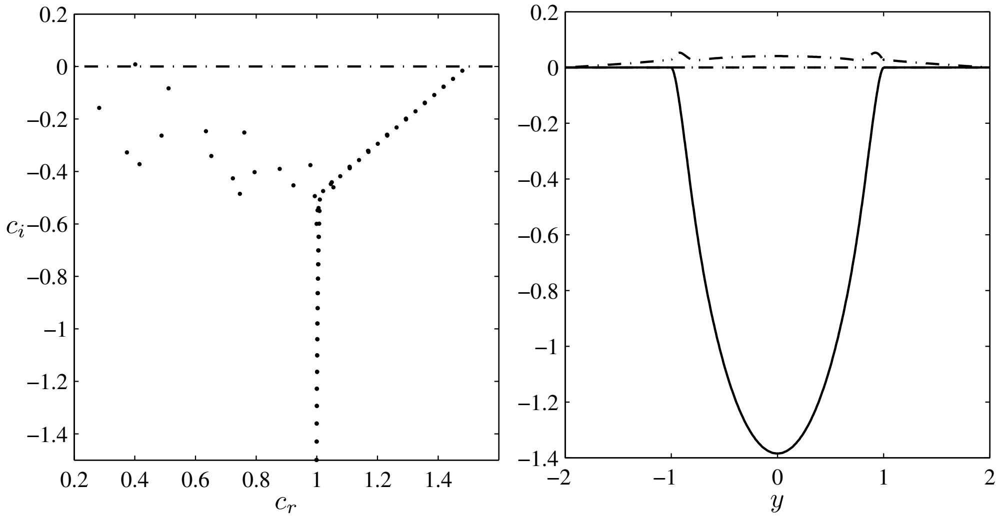

(a) (b)

FIGURE 4.2: Eigenvalues (a) and eigenfunction (b) of mode $\alpha = 1$ and $\beta = 0$ for parameters Re $= 3100$, half-height of the porous layer $h_p = 0.5$, permeability $\sigma = 0.004$, porosity $\epsilon = 0.6$ and momentum transfer coefficient $\tau = 0$. In sub-figure (b) the continuos and dash-dotted lines are used for the real and imaginary parts of v, while the dashed and dotted lines are used for the real and imaginary parts of η

In order to verify that our program works properly, we compare the initial growth rate of perturbation's kinetic energy (4.56) obtained by our calculations, with the one predicted by the linear stability analysis (4.58). In particular, we consider an unstable case, $c_i > 0$, and in that case the most unstable eigenvalue is the one dominating the energy growth rate.

We consider a flow at Re $= 3100$, with the half-height of the porous layers $h_p = 0.5$, permeability $\sigma = 0.004$, porosity $\epsilon = 0.6$ and momentum transfer coefficient $\tau = 0$. Note that this case is one of the cases studied in the next chapter. For mode $\alpha = 1$ and $\beta = 0$, the linear stability analylis provides the eigenvalues plotted in figure 4.2(a). The value of the unstable eigenvalue is $c = 0.336 + 0.00227i$. The numerical simulation starts form the laminar solution, plotted in figure 4.3(a), with the eigenfunction, plotted in figure 4.2(b), as perturbation on mode $\alpha = 1$ and $\beta = 0$.

The computed energy growth rate is shown in figure 4.3(b) with a solid line, compared with the one predicted by equation (4.58) plotted with dashed line. Note that, we have to compare only the rate of the two curves, not their values. We can see that the computed energy growth rate is very similar to the one predicted by the linear stability analysis. We want to verify that linearity is preserved varying the simulations parameters, such as the number of modes in the streamwise and spanwise directions, the number of grid nodes in the wall-

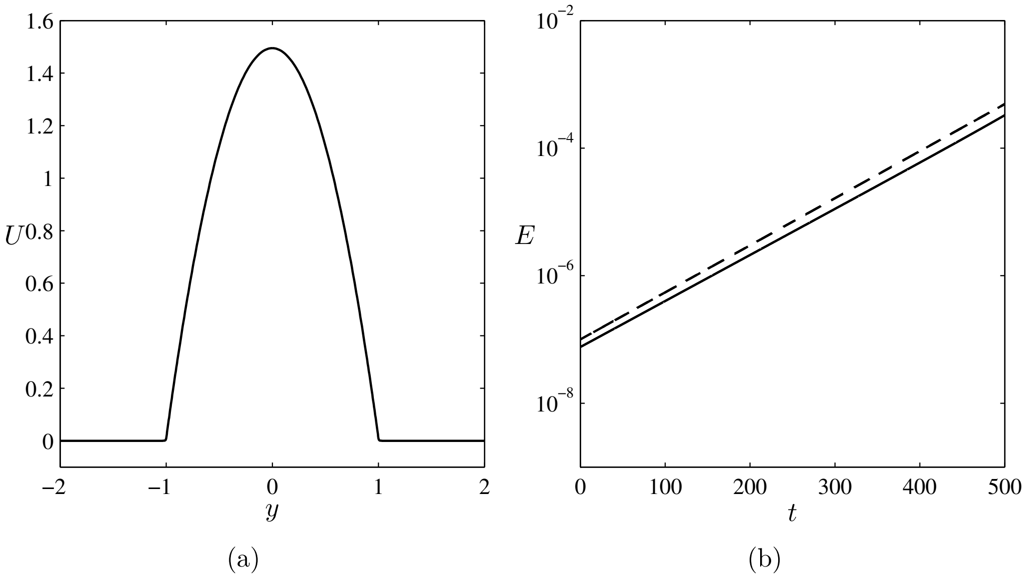

(a) (b)

FIGURE 4.3: Laminar solution (a) and energy growth of disturbances (b) for a channel flow over porous walls at Re = 3100. The porous layers have half-height $h_p = 0.5$, permeability $\sigma = 0.004$, porosity $\epsilon = 0.6$ and momentum transfer coefficient $\tau = 0$. In sub-figure (b) the dashed line is the energy growth rate used as reference, while the solid line represents the computed energy growth.

normal direction, the time step, and the initial amplitude of the perturbation. Figure 4.4 shows the energy growth rates for the different cases. We note that, the differences in all the cases are negligible. Only figure 4.4(b) shows a deviation from the linear behaviours for large values of energy. In this case, the perturbation is too big to neglect the nonlinear terms, so the linear analysis is no more valid.

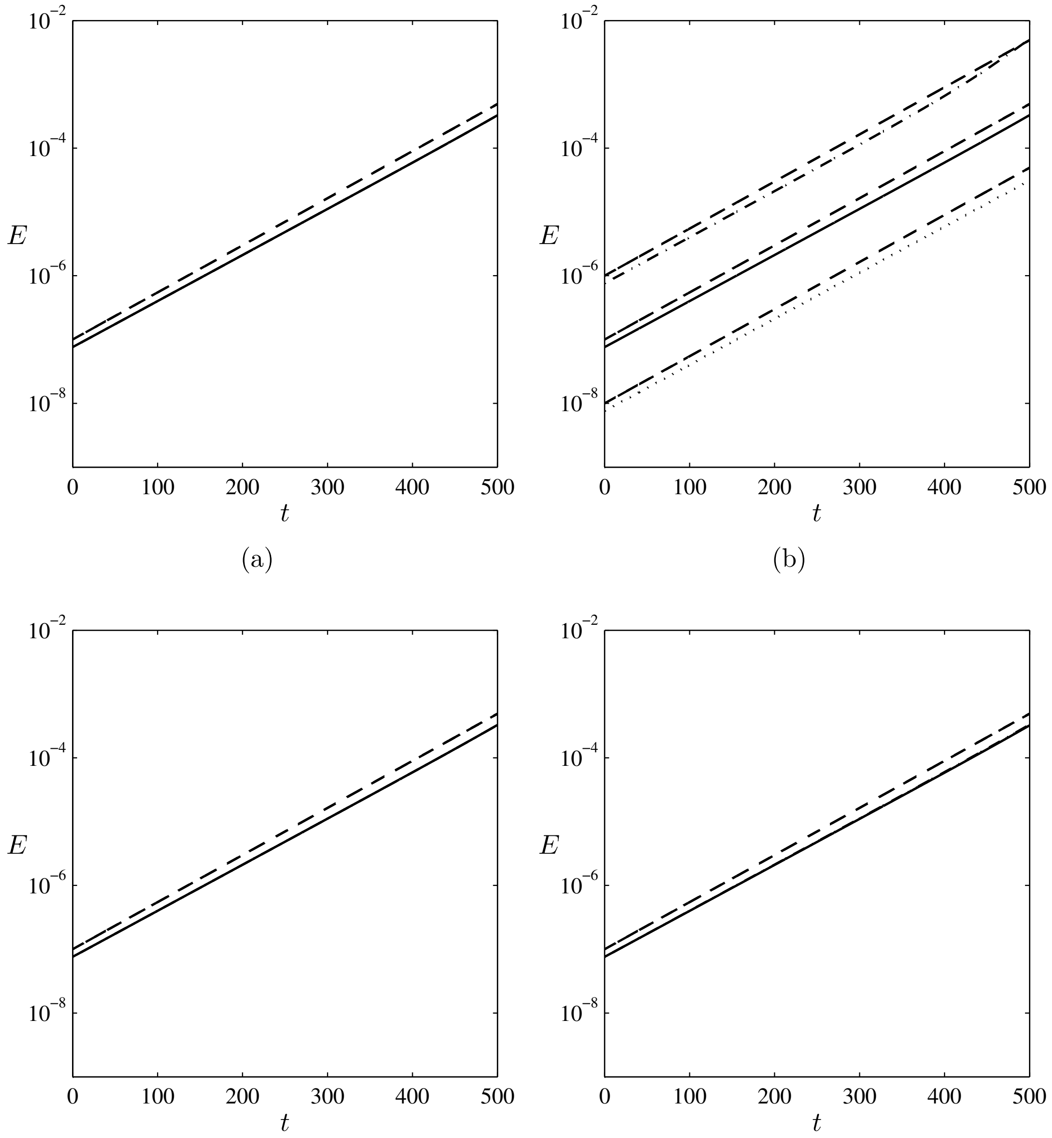

(a)

(b)

(c)

(d)

FIGURE 4.4: Energy growth of perturbation of mode $\alpha = 1$ and $\beta = 0$, of a channel flow at $\mathrm{Re} = 3100$ over porous walls of half-height $h_p = 0.5$, permeability $\sigma = 0.004$, porosity $\epsilon = 0.6$ and momentum transfer coefficient $\tau = 0$. The dash-dotted lines represent the predicted growth rate. The figures differ for the parameters used in the simulations. In sub-figure (a) we use different Δt: dash-dotted line $\Delta t = 0.02$, solid line $\Delta t = 0.04$ and dotted line $\Delta t = 0.06$. In sub-figure (b) we use perturbation with different initial amplitude. The different scale factors are: dash-dotted line $10^{-3.5}$, solid line 10^{-4} and dotted line $10^{-4.5}$. In sub-figure (c) we use different number of modes: solid line $n_x = n_z = 4$, dash-dotted line $n_x = n_z = 8$ and dotted line $n_x = n_z = 16$. In sub-figure (d) we use different number of grid points in the wall normal direction: dash-dotted line $n_y = 150$, solid line $n_y = 200$ and dotted line $n_y = 250$.

Chapter 5

Results

In this chapter, we present the results obtained by the direct numerical simulations of channel flows over two identical porous walls. We considered two cases, one at medium Reynolds number $\mathrm{Re} = 3100$ and one at very low Reynolds number $\mathrm{Re} = 950$. In the first case we study how the porous walls affect turbulence statistics, while in the second case we investigate if the porous wall can sustain turbulent flows at low Reynolds number.

5.1 Turbulent channel flow over a porous wall

We consider a turbulent channel flow, at a bulk Reynolds number of 3100, over two identical porous walls, whose half-heights are $h_p = 0.5$. The permeability of the porous layers is $\sigma = 0.004$, the porosity is $\varepsilon = 0.6$, and the coefficient τ of the momentum transfer conditions is set equal to zero. The computation is carried out on a grid of $128 \times (128 + 128 + 128) \times 128$ points, in the x, y and z directions respectively, on a computational domain of $2\pi \times (1 + 2 + 1) \times \pi$. The resolution of the numerical simulation is $\Delta x^+ \approx 10$ in wall units in the streamwise direction, $\Delta z^+ \approx 5$ in the spanwise direction, and with a minimum Δy^+ in the wall-normal direction which is less than 1.

The wall units, indicated by the superscript " $^+$ ", are measured in terms of the dimensionless viscous length δ_ν, which is defined as follows

$$\delta_\nu = \frac{1}{u_\tau \mathrm{Re}}, \tag{5.1}$$

where u_τ is the dimensionless friction velocity. Note that we use the viscous length and the friction velocity as reference length scale and velocity scale, respectively, in the near-wall regions. For a turbulent channel flow with solid walls, the friction velocity is defined as follows

$$u_\tau = \sqrt{\frac{1}{\mathrm{Re}} \left. \frac{d\overline{u}}{dy} \right|_{y=-1}}, \tag{5.2}$$

where $\overline{u}$ is the mean velocity, $y = -1$ is the location of the wall, and the " $^-$ " indicates the average over t and over the homogeneous directions, x and z. In the case of a turbulent channel flow over porous walls, the definition (5.2) must be modified to account for the slip velocity at the interface as follows (Breugem and Boersma [7])

$$u_\tau = \sqrt{\frac{1}{\mathrm{Re}} \frac{d\overline{u}}{dy}\bigg|_{y=-1} - \overline{u'v'}\Big|_{y=-1}}, \tag{5.3}$$

where $\overline{u'v'}$ is one of the components of the Reynolds stresses and the superscript " $'$ " indicates the perturbation from the average. The Reynolds number based on the friction velocity u_τ is called friction Reynolds number Re_τ, and is defined as $\mathrm{Re}_\tau = u_\tau \mathrm{Re}$. In our case, the friction Reynolds number is $\mathrm{Re}_\tau = 200$.

We start the comparison between the turbulent channel flows with porous or impermeable walls by analyzing their mean properties. Figure 5.1 shows the x-component $\overline{u}$ of the mean velocity profile. The other two components of the mean velocity, $\overline{v}$ and $\overline{w}$, are equal to zero. As a reference, in the same figure we plot the mean velocity profile of a channel flows over impermeable walls with a dashed line. For both cases the maximum velocity is reached at the centerline and is $\overline{u}_c = 1.16$.

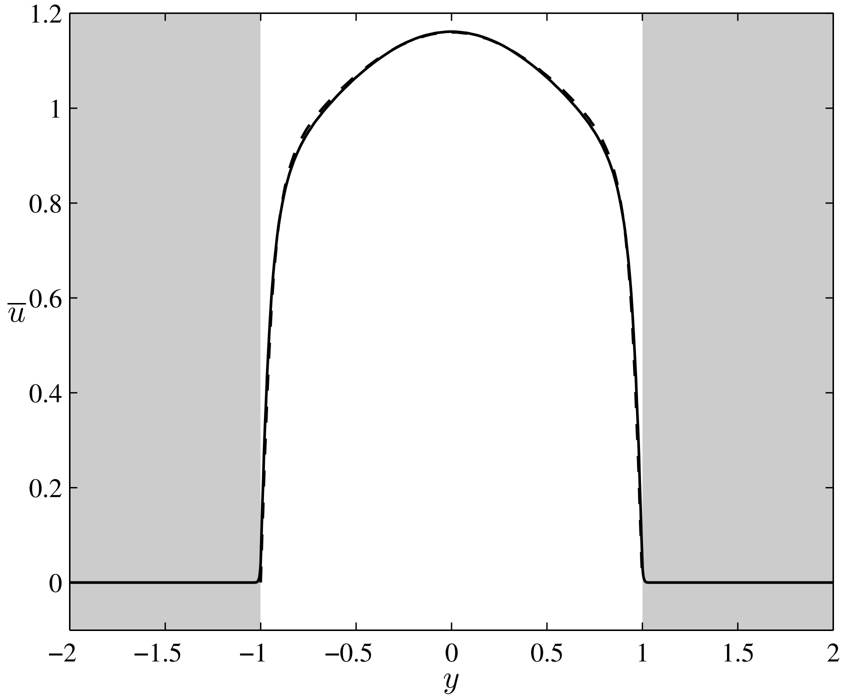

FIGURE 5.1: Mean velocity profile of turbulent channel flow at $\mathrm{Re} = 3100$ over porous walls. The half-heights of the porous layers are $h_p = 0.5$, the permeability is $\sigma = 0.004$ and the porosity is $\varepsilon = 0.6$. The solid and dashed line indicate the velocity profiles of channel flows over porous and impermeable walls, respectively.

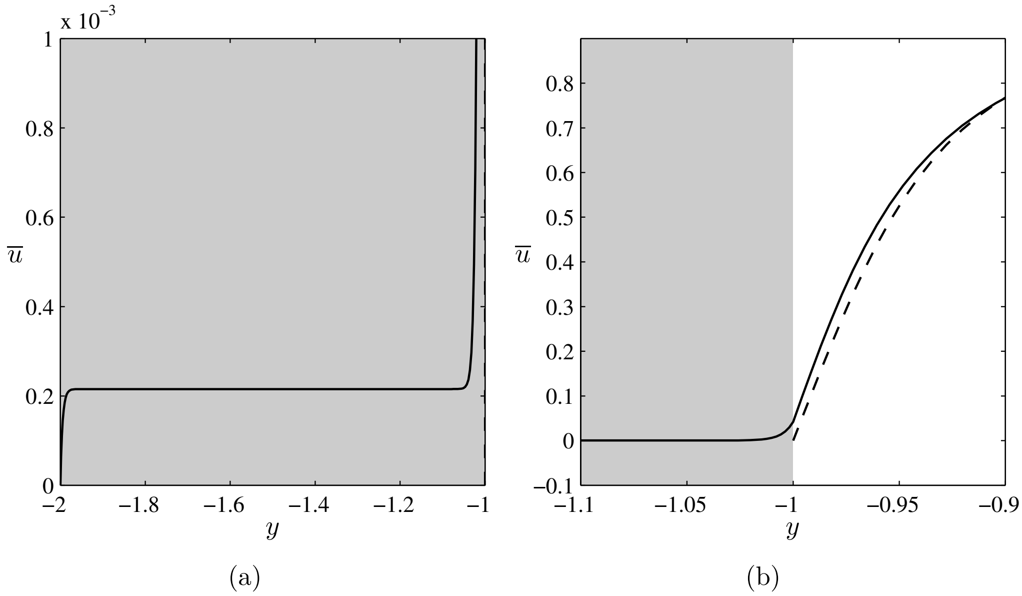

(a) (b)

FIGURE 5.2: Zoomed views of the mean velocity profile in the porous layer (a) and at the interface with the fluid region (b) for a turbulent flow at Re = 3100. The half-heights of the porous layers are $h_p = 0.5$, the permeability is $\sigma = 0.004$ and the porosity is $\varepsilon = 0.6$. The dashed line indicates the velocity profile of a channel flow over impermeable walls.

We can observe a few differences at the interface between the fluid region and the porous layers, where there is a slip velocity of about $\overline{u}_i = 0.0417$. We show zoomed views of the mean velocity profiles at the interface and in the porous layer in figure 5.2. In the porous layers, figure 5.2(a), the velocity is zero at the impermeable wall and rises to a constant value through a small boundary layer. Inside the porous layer the velocity is constant and equals the Darcy velocity, whose magnitude is $\overline{u}_D = 0.000215$. As we approach the interface, figure 5.2(b), the fluid velocity increases from the Darcy velocity $\overline{u}_D$ to the interface velocity $\overline{u}_i$, and this is achieved in the so called Brinkman layer whose height is 0.0201. At the interface, the mean velocity profile has a y-derivative which equals 13.3, while in a channel with impermeable walls the y-derivative is 12.1. As shown by the value of the y-derivative, the friction velocity in the porous case (0.0667) is greater than in the case of impermeable walls (0.0627).

Figure 5.3 shows the mean velocity profiles as $\Delta\overline{u}^+ = \overline{u}^+ - \overline{u}_i^+$ versus the logarithm of the distance from the interface $\tilde{y} = y - 1$ expressed in wall-units. We draw the velocity profiles with this downward shift, as done by Hahn *et al.* [15], to remove the upward shift due to the slip velocity at the permeable wall. Note that after the downward shift, the mean velocity profiles pass for the point $\tilde{y}^+ = 1, \overline{u}^+ = 1$. For the channel flow, we can usually identify three regions. The region where $\tilde{y}^+ < 5$ is called viscous sublayer and the variation of $\overline{u}^+$ with $\tilde{y}^+$ is

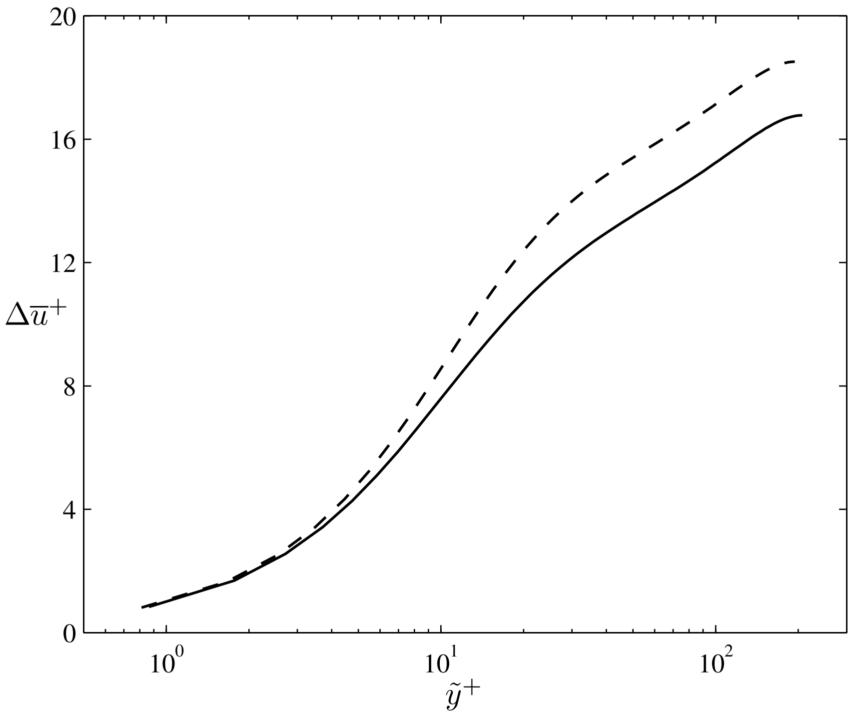

FIGURE 5.3: Mean velocity profile of turbulent channel flow at Re = 3100 in wall units. The curves are shifted downwards by $\overline{U}_i$. The half-heights of the porous layers are $h_p = 0.5$, the permeability is $\sigma = 0.004$ and the porosity is $\varepsilon = 0.6$. The solid and dashed line indicate the velocity profiles of channel flows over porous and impermeable walls, respectively.

approximately linear, i.e.

$$\overline{u}^+ = \tilde{y}^+. \tag{5.4}$$

The region where $\tilde{y}^+ > 30$ is called log-law region where the variation of $\overline{u}^+$ versus $\tilde{y}^+$ is logarithmic, i.e.

$$\overline{u}^+ = \frac{1}{k}\log\tilde{y}^+ + B^+, \tag{5.5}$$

where k (Von Karman constant) and B^+ are two constants. This relationship is called logarithmic law. The values of k and B^+ for smooth walls are usually assumed to be $k = 0.41$ and $B^+ = 5$. However, for the Reynolds number that we are considering, a better fit with experimental and numerical simulations is obtained with $k = 0.41$ and $B^+ = 5.5$. Finally, the region between 5 and 30 wall units is called buffer layer and neither laws hold. We note that the three regions are still present in the simulation of the channel flow over porous walls. The main differences between the two turbulent flows are present in the logarithmic region, where the curve of the porous case is lower than the case with solid walls, and this is generally representative of a greater friction.

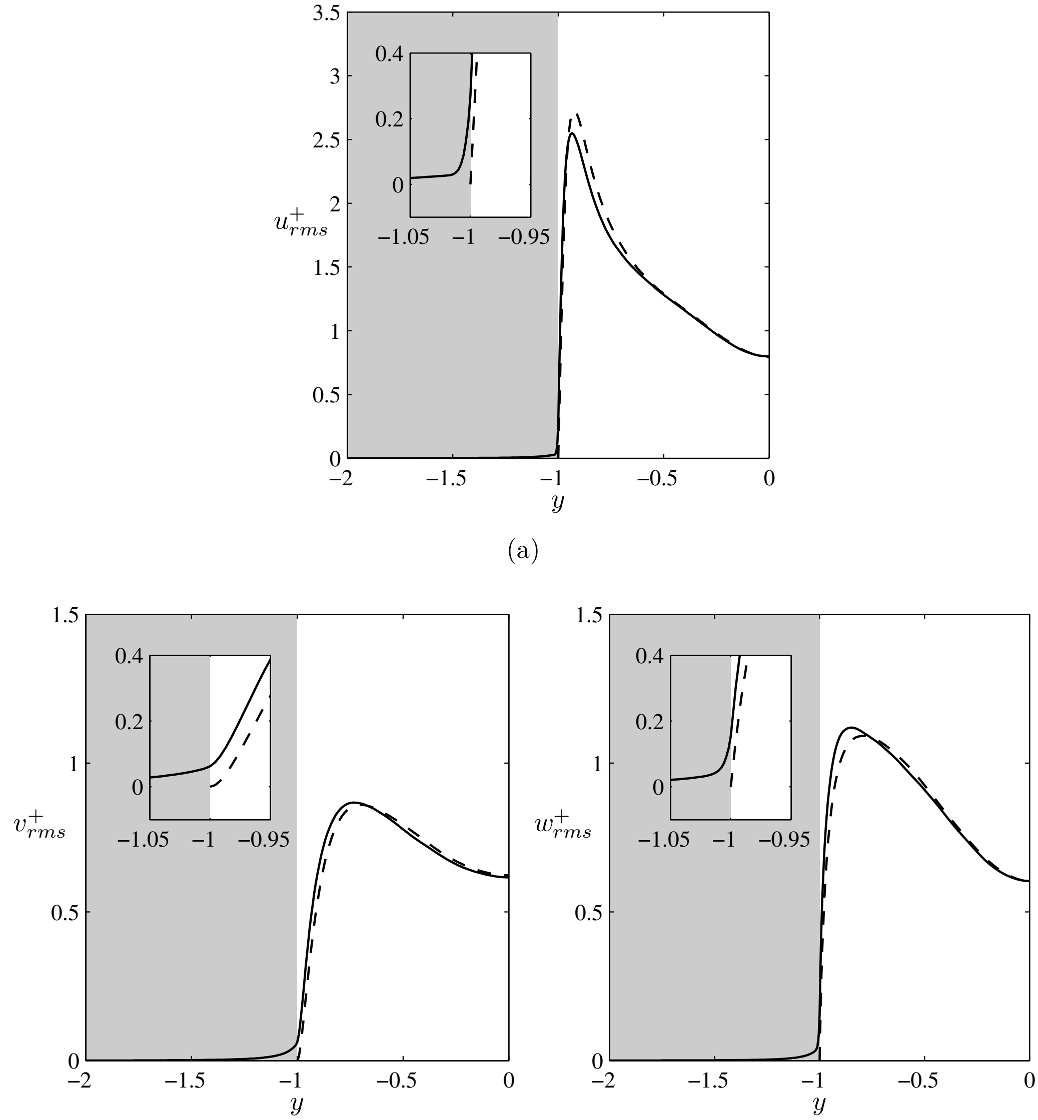

(a)

(b)

(c)

FIGURE 5.4: Rms velocity made dimensionless with the friction velocity, for a turbulent flow at Re = 3100. The half-heights of the porous layers are $h_p = 0.5$, the permeability is $\sigma = 0.004$ and the porosity is $\varepsilon = 0.6$. The solid and dashed line indicate the flow over porous and impermeable walls, respectively.

We continue our comparison between the turbulent channel flows with porous or impermeable walls by analyzing the turbulence intensities. For both flows, the root mean square (rms) velocities, made dimensionless with the friction velocity, are defined as follows,

$$u^+_{rms} = \frac{\sqrt{\overline{u'u'}}}{u_\tau}, \quad v^+_{rms} = \frac{\sqrt{\overline{v'v'}}}{u_\tau}, \quad w^+_{rms} = \frac{\sqrt{\overline{w'w'}}}{u_\tau}. \tag{5.6}$$

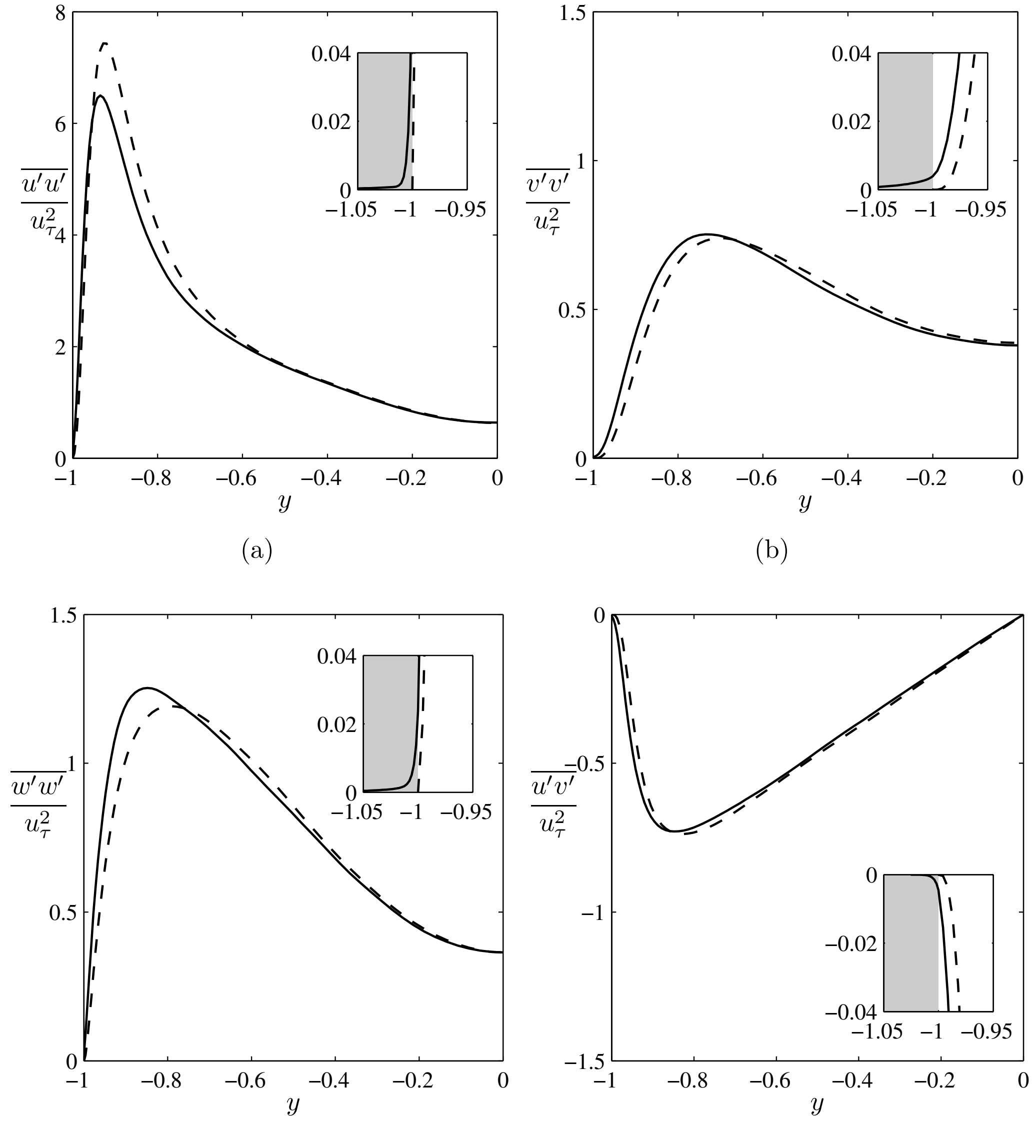

(a) (b)

(c) (d)

FIGURE 5.5: Reynolds stresses for a turbulent flow at Re = 3100. The half-heights of the porous layers are $h_p = 0.5$, the permeability is $\sigma = 0.004$ and the porosity is $\varepsilon = 0.6$. The solid and dashed line are used for the flow over porous and impermeable walls, respectively.

Figure 5.4 shows the rms velocities of a turbulent channel flow over porous walls, compared with the ones of a channel flow over impermeable walls, and we note a changing in all the rms velocities, especially near the centerline and at the interface with the fluid region. All the rms velocities are not null at the interface, but they rapidly decrease inside the porous layer. The greatest difference can be noticed in the wall-normal and spanwise rms velocities, whose peaks and the values of the rms velocities at the centerline are greater in the porous case, indicating greater fluctuations, than in the impermeable case. Therefore, we conclude that the porous walls affects the turbulence intensities mainly by increasing the wall-normal and spanwise fluctuations. Moreover, the permeability of the wall enhances all the turbulence fluctuations near the interface.

We continue our comparison between the turbulent channel flows with porous or impermeable walls by analyzing the total shear stress and the components of the Reynolds stress tensor. The Reynolds stress tensor is a symmetric tensor defined as follows

$$\begin{bmatrix} \overline{u'u'} & \overline{u'v'} & \overline{u'w'} \\ \overline{u'v'} & \overline{v'v'} & \overline{v'w'} \\ \overline{u'w'} & \overline{v'w'} & \overline{w'w'} \end{bmatrix}. \tag{5.7}$$

The diagonal components, $\overline{u'u'}$, $\overline{v'v'}$ and $\overline{w'w'}$, are called normal stresses, while the off-diagonal components, $\overline{u'v'}$, $\overline{u'w'}$ and $\overline{v'w'}$, are called shear stresses. Due to the symmetry of the flow, the Reynolds stresses $\overline{u'w'}$ and $\overline{v'w'}$ equal zero, $\overline{u'v'}$ is an odd function of y, and $\overline{u'u'}$, $\overline{v'v'}$ and $\overline{w'w'}$ are even functions of y. Figure 5.5 shows the Reynolds stresses of the turbulent channel flow over porous walls. As in

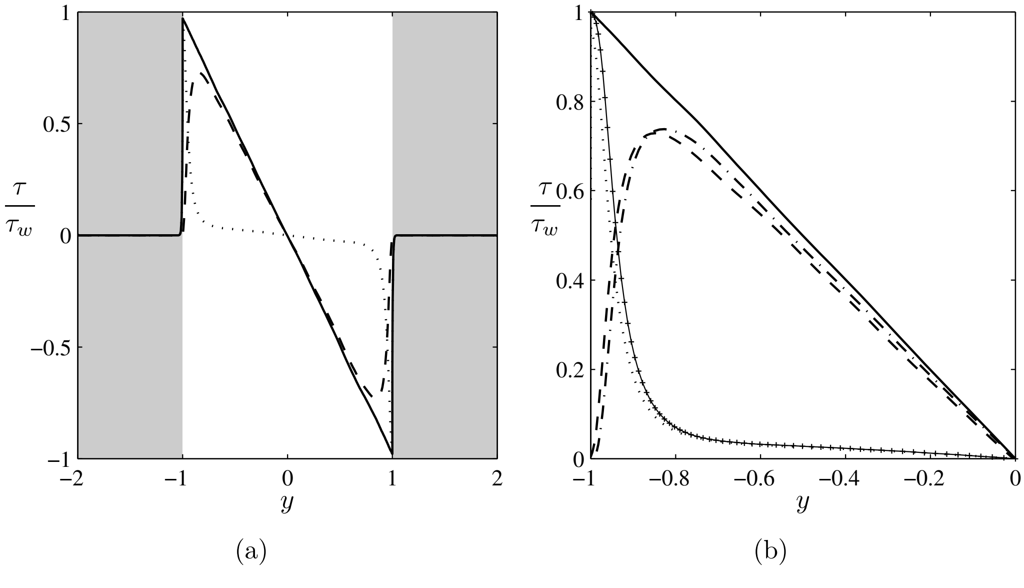

(a) (b)

FIGURE 5.6: The solid line represents the total shear stress, decomposed in the viscous stress, plotted with a dotted line, and the Reynolds shear stress, plotted with a dashed line. The half-heights of the porous layers are $h_p = 0.5$, the permeability is $\sigma = 0.004$, the porosity is $\varepsilon = 0.6$ and the Reynolds number is $\mathrm{Re} = 3100$. In figure (b) the dashed and dotted lines represent the shear and viscous stresses for the porous case, respectively, while the dash-dotted and crossed lines represent the shear and viscous stresses, respectively, for the case with solid walls.

the case for the rms velocities, we observe an increase in the peaks of the normal stresses in the wall-normal and spanwise directions, while there is a decrease of the normal stress in the streamwise direction. Moreover, all the peaks are shifted towards the interface, and the stresses are non zero at the interface.

We can define the total shear stress τ as the sum of the Reynolds shear stress $\overline{u'v'}$ with the viscous stress. So, we have

$$\tau = \frac{1}{\mathrm{Re}}\frac{d\overline{u}}{dy} - \overline{u'v'}. \tag{5.8}$$

Figure 5.6 shows the total shear stress and its decomposition in viscous and Reynolds stress. With respect to the channel flow over impermeable walls, we note that at the interface with the porous layer the Reynolds stress $\overline{u'v'}$ does not vanish, and the viscous stress does not reach unity, but their sum is one.

5.1.1 The effects of the porous half-height h_p

h_p	n_y^p	u_τ
0.10	64	0.0669
0.25	96	0.0668
0.50	128	0.0667
1.00	164	0.0666
2.00	192	0.0660

Table 5.1: Number of grid points n_y^p in the porous layers and friction velocity u_τ obtained from the simulations of turbulent channel flows over porous walls at Re = 3100. The half-height of the porous layers h_p is varied between 0.10 and 2. The permeability of the porous layers is $\sigma = 0.004$ and the porosity is $\varepsilon = 0.6$.

We present a parametric study where we varied the half-height of the porous layers h_p. The purpose of this study is to understand which is the height of the porous layers that affects the most turbulence statistics. We consider a turbulent flow at Reynolds number Re = 3100, and the porous layers have permeability $\sigma = 0.004$, porosity $\varepsilon = 0.6$, and the momentum transfer coefficient τ is set equal to zero. We consider five cases, where the half-height of the porous layer h_p ranges from 0.10 to 2, $h_p = 0.10, 0.25, 0.50, 1, 2$.

To resolve accurately the flow in the porous region, we set a different number of nodes in the wall-normal direction for each simulation, increasing the number with the height of the porous layers, in order to maintain the same numerical resolution. In table 5.1, we report the number of grid points for each simulation, together with the friction velocity u_τ. We note that the friction velocity increases as the height of the porous layers decreases.

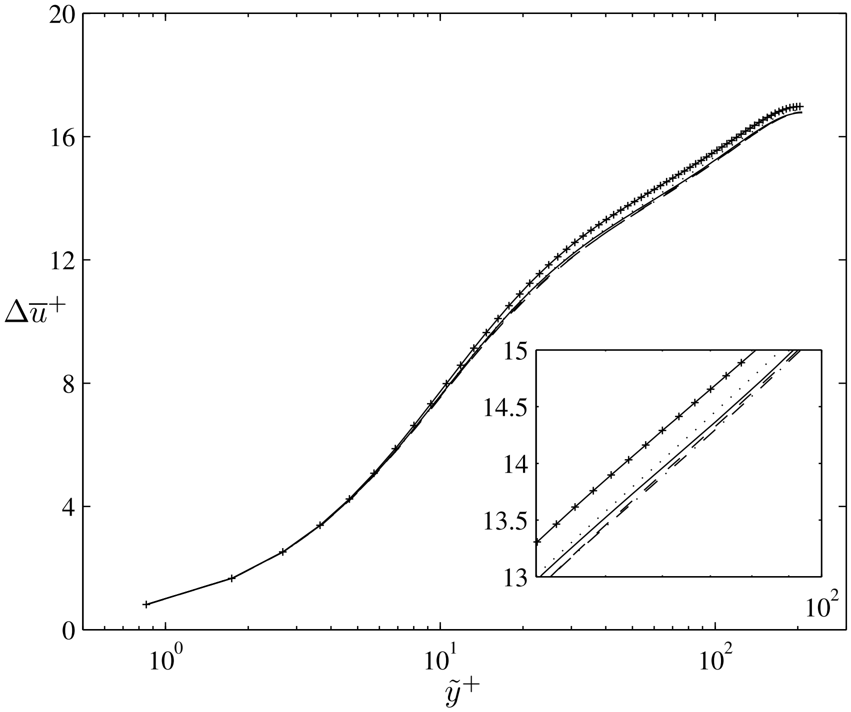

FIGURE 5.7: Mean velocity profiles of turbulent channel flows, made dimensionless with the friction velocity, for different half-heights of the porous layers h_p. The curves are shifted downwards by $\overline{U}_i$. The case with $h_p = 0.10$ is plotted with dash-dotted line, $h_p = 0.25$ with dashed line, $h_p = 0.5$ with solid line, $h_p = 1$ with dotted line and $h_p = 2$ with crossed line. The permeability of the porous layers is $\sigma = 0.004$, the porosity is $\varepsilon = 0.6$ and the Reynolds number is $\mathrm{Re} = 3100$,.

In figure 5.7, we show the mean velocity profiles, made dimensionless by the friction velocity, as $\Delta\overline{u}^+ = \overline{u}^+ - \overline{u}_i^+$. We note that the differences between the various cases are quite small. We observe that all the curves are close to each other and ordered with h_p, the lower corresponding to lower h_p. Note that the curves are shifted downwards, and the downward shift is greater for higher h_p.

Figure 5.8 shows the Reynolds stresses at different heights of the porous layers. Only small differences are noticeable. The normal stress $\overline{u'u'}$ and the shear stress $\overline{u'v'}$ seem not affected by the height of the porous layer, even if the peak of the normal stress has a little increase and the peak of the shear stress has a little decrease for the higher porous layers. The other two normal stresses, $\overline{v'v'}$ and $\overline{w'w'}$, instead, change with h_p. In both cases, the peaks are lower for the higher heights of the porous layers, and are shifted towards the centerline.

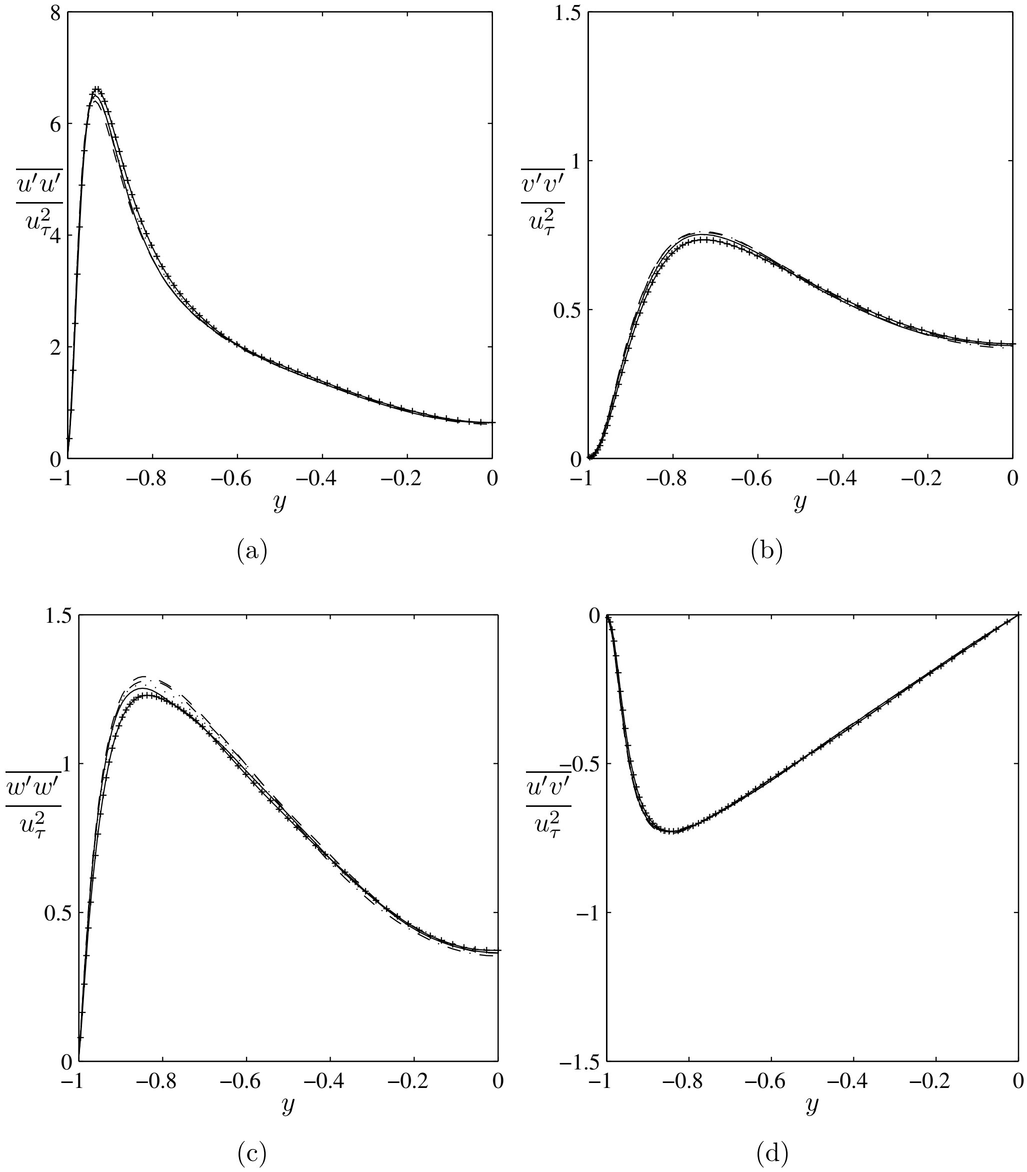

FIGURE 5.8: Reynolds stresses for different heights of the porous layers for a turbulent channel flows over porous walls at Re = 3100. The case with $h_p = 0.10$ is plotted with dash-dotted line, $h_p = 0.25$ with dashed line, $h_p = 0.5$ with solid line, $h_p = 1$ with dotted line and $h_p = 2$ with crossed line. The permeability of the porous layers is $\sigma = 0.004$ and the porosity is $\varepsilon = 0.6$.

5.1.2 The effects of the momentum transfer coefficient τ

We now investigate the effects of the momentum transfer coefficient τ on the turbulence statistics. We consider only the cases with the minimum and maximum half-heights of the porous layers, $h_p = 0.10$ and $h_p = 2.00$, because we expect that

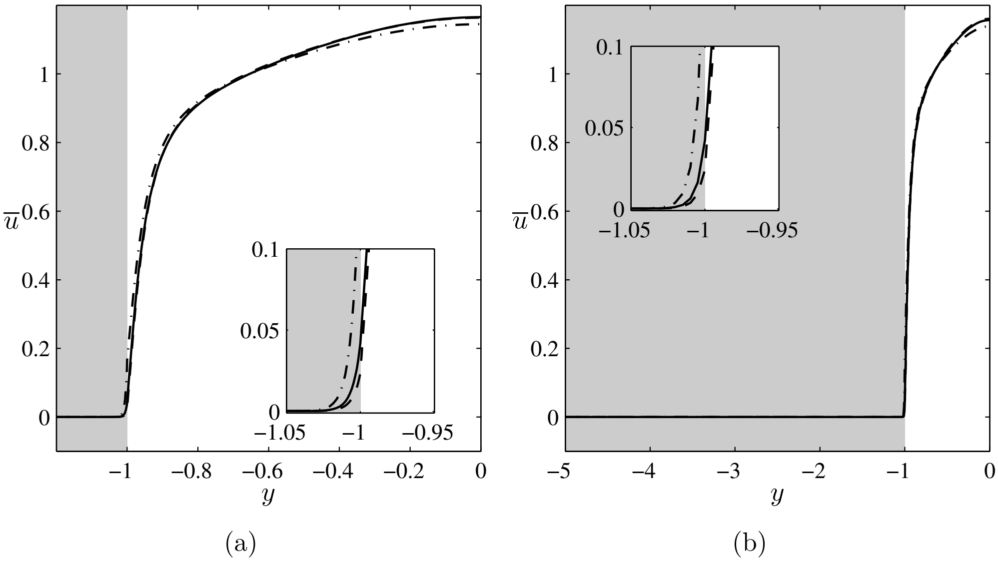

(a)

(b)

FIGURE 5.9: Mean velocity profiles of turbulent channel flow over porous walls, made dimensionless with the friction velocity, with varying momentum transfer coefficient τ. The Reynolds number is $\mathrm{Re} = 3100$ and the porous layers have permeability $\sigma = 0.004$, porosity $\varepsilon = 0.6$. The half-height of the porous layer h_p equals 0.10 in figure (a) and equals 2.00 in figure (b). The solid lines are the profile for $\tau = 0$, the dashed line are used for $\tau = -1$, and the dash-dotted lines are used for $\tau = 1$.

the turbulence statistics of the others cases will fall within these two. We study only three values of τ, -1, 0 and 1, because the momentum transfer coefficient τ of most of the porous media falls in this range. Note that the case $\tau = 0$ is used

h_p	τ	n_y^p	$\overline{u}_i^+$	u_τ
0.10	-1	64	0.355	0.0668
0.10	0	64	0.631	0.0668
0.10	1	64	2.601	0.0626
2.00	-1	192	0.359	0.0666
2.00	0	192	0.630	0.0660
2.00	1	192	2.99	0.0579

TABLE 5.2: Number of grid points n_y^p in the porous layers, interface velocity expressed in wall units $\overline{u}_i^+$, and friction velocity u_τ obtained from the simulations of turbulent channel flows over porous walls at $\mathrm{Re} = 3100$. The simulations differ for the half-height of the porous layers, which is $h_p = 0.10$ or $h_p = 2$, and for the momentum transfer coefficient τ which is varied between -1 and 1.

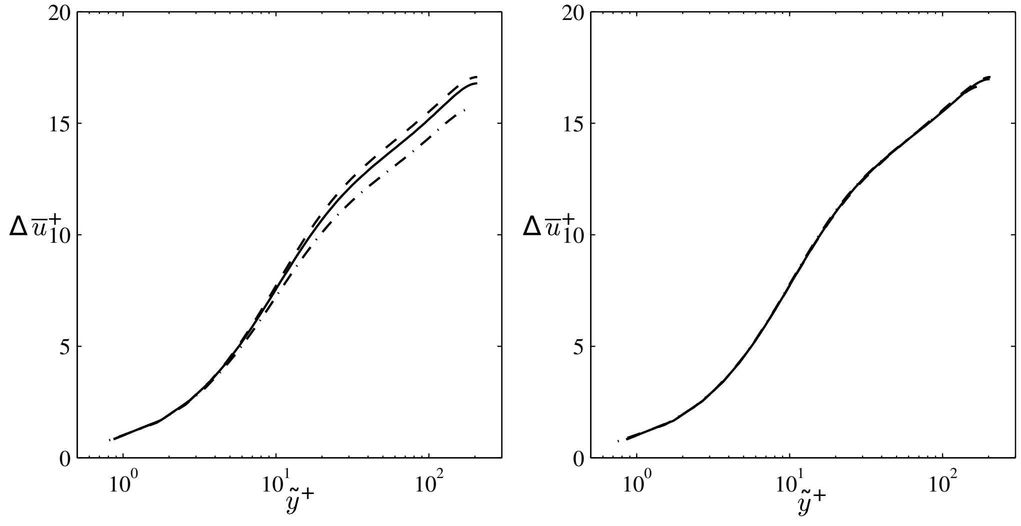

(a)

(b)

FIGURE 5.10: Mean velocity profiles of turbulent channel flows, made dimensionless with the friction velocity, with varying momentum transfer coefficient τ. The Reynolds number is Re $= 3100$ and the porous layers have permeability $\sigma = 0.004$, porosity $\varepsilon = 0.6$. The half-height of the porous layer h_p equals 0.10 in figure (a) and equals 2.00 in figure (b). The solid lines are the profile for $\tau = 0$, the dashed line are used for $\tau = -1$, and the dash-dotted lines are used for $\tau = 1$.

as a reference case. We keep unchanged the other parameters of the porous layers as in the previous simulations. In particular, the permeability σ equals 0.004 and the porosity ε equals 0.6. The turbulent flow is simulated at Re $= 3100$.

Figure 5.9 shows the mean velocity profiles for the three momentum transfer coefficients considered. In figure 5.9(a) is plotted the velocity profile for the flow over a porous layer whose height is $h_p = 0.10$, while figure 5.9(b) shows the profile when $h_p = 2.00$. The case with the positive τ is drawn with a dash-dotted line, while the case with the negative τ is drawn with dashed line. The effects of the momentum transfer coefficient τ on the mean velocity profile are quite evident. In both figures, the positive τ induces a decrease of the velocity at the centerline, while increases significantly the velocity at the interface between the porous layers and the fluid region. Also the derivatives of the mean velocity profile at the interface are quite different. We report the interface velocities in wall units and the friction velocities for the various cases in table 5.2. Note that the velocities at the interface with the fluid region increase significantly as τ increases from -1 to 1. Apparently, this increase is not linear with the linear variation of the momentum transfer coefficient. Consistently, the friction velocity u_τ is greater when τ is negative than when τ is positive.

Figure 5.10 shows the mean velocities profiles, in wall units, on a logarithmic

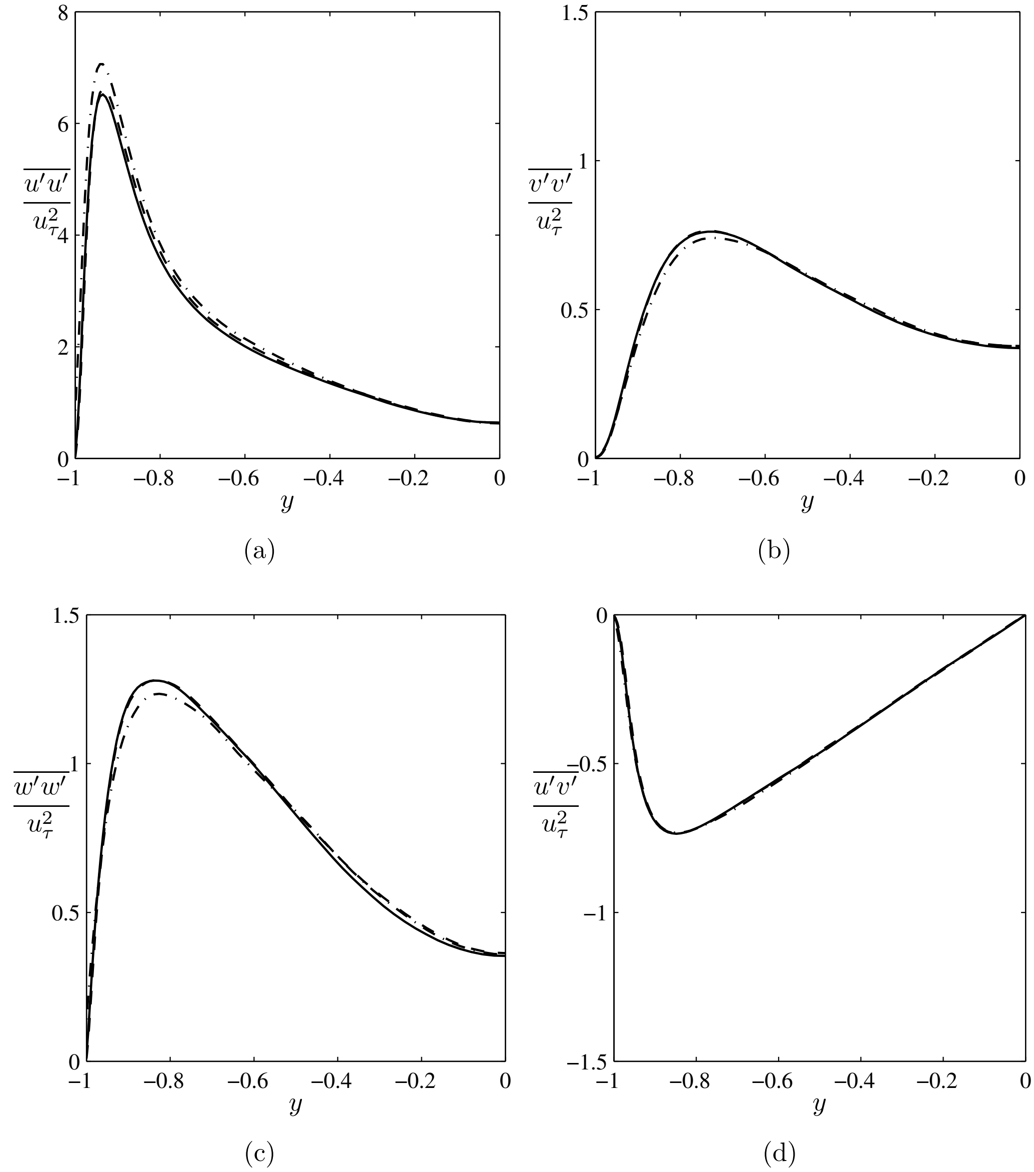

(a) (b)

(c) (d)

FIGURE 5.11: Reynolds stresses with varying momentum transfer coefficient τ. The half-height of the porous layer h_p equals 0.10. The solid lines are the profile for $\tau = 0$, the dashed line are used for $\tau = -1$, and the dash-dotted lines are used for $\tau = 1$.

scale. Note that we plot $\Delta\overline{u}^+ = \overline{u}^+ - \overline{u}_i^+$, to compensate for the effects of the slip velocity. For low height of the porous layers, the positive τ lowers the velocity profile in the logarithmic region, while the negative τ raise it (figure 5.10(a)). We observe that the effect of the momentum transfer coefficient seems reducing when the height of the porous layers h_p increase (figure 5.10(b)).

Figure 5.11 and 5.12 show how the Reynolds stresses are affected by the

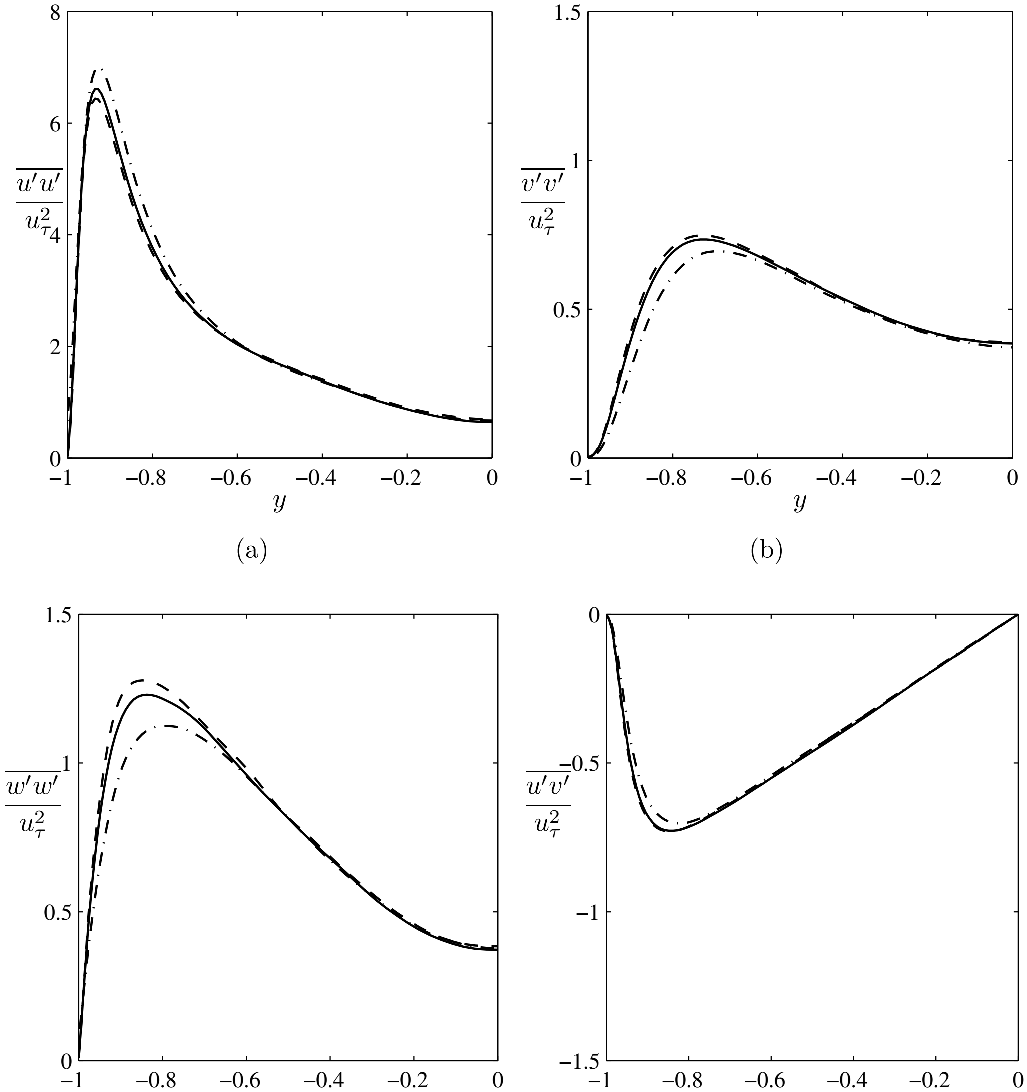

(a) (b)

(c) (d)

FIGURE 5.12: Reynolds stresses with varying momentum transfer coefficient τ. The half-height of the porous layer h_p equals 2.00. The solid lines are the profile for $\tau = 0$, the dashed line are used for $\tau = -1$, and the dash-dotted lines are used for $\tau = 1$.

momentum coefficient τ. In particular in figure 5.11 we plot the Reynolds stresses for the smallest porous height $h_p = 0.10$, while in figure 5.12 we plot the Reynolds stresses for the largest porous height $h_p = 2.00$. We observe that the positive τ induces an increase of the Reynolds stress $\overline{u'u'}$, while reduces the Reynolds stresses $\overline{v'v'}$, $\overline{w'w'}$ and $\overline{u'v'}$. The negative τ has an opposite but weaker effect.

5.2 Very low Reynolds number turbulent flow

We consider a turbulent channel flow, at a bulk Reynolds number of 950, over two identical porous walls, whose heights are $h_p = 1$. The permeability of the porous layers is $\sigma = 0.01$, the porosity is $\varepsilon = 0.6$, and the coefficient of the momentum transfer conditions is set equal to zero $\tau = 0$. The computation is carried out on a grid of $128 \times (128 + 128 + 128) \times 128$ points, in the x, y and z direction respectively, on a computational domain of $2\pi/0.4 \times (2 + 2 + 2) \times 2\pi/0.8$. The resolution of the numerical simulation is $\Delta x^+ \approx 8$ in the streamwise direction, $\Delta z^+ \approx 4$ in the spanwise direction, and with a minimum Δy^+ in the wall-normal direction which is less than 0.5. The friction Reynolds number is $\mathrm{Re}_\tau = 65$. To the best of our knowledge, the lowest friction Reynolds number at which a turbulent channel flow has been simulated is $\mathrm{Re}_\tau = 70$ [51]. The authors reported that, a big computational domain is needed to simulate accurately very low Reynolds number flows. We use a computational domain twice as large as the one used in the previous simulations. Note that, the effects of the size of the computational domain should be investigated further.

We start analyzing the mean properties of the turbulent channel flows with porous walls at low Reynolds number. Figure 5.13(a) shows the x-component of the mean velocity profile $\overline{u}$ compared with the laminar profile U at the same

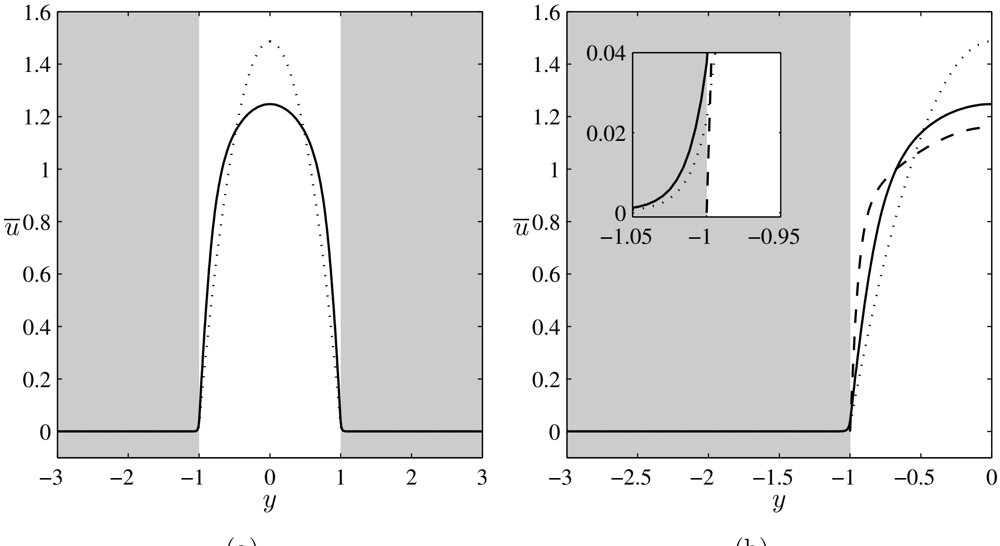

(a) (b)

FIGURE 5.13: Mean velocity profiles of channel flows at Re = 950. The half-heights of the porous layers are $h_p = 1$, the permeability is $\sigma = 0.01$, the porosity is $\varepsilon = 0.6$. The solid and dotted line are the velocity profiles of turbulent and laminar channel flows over porous walls, respectively. In figure (b) the dashed line is the mean velocity profile of a turbulent channel flow over impermeable walls at Re = 3100.

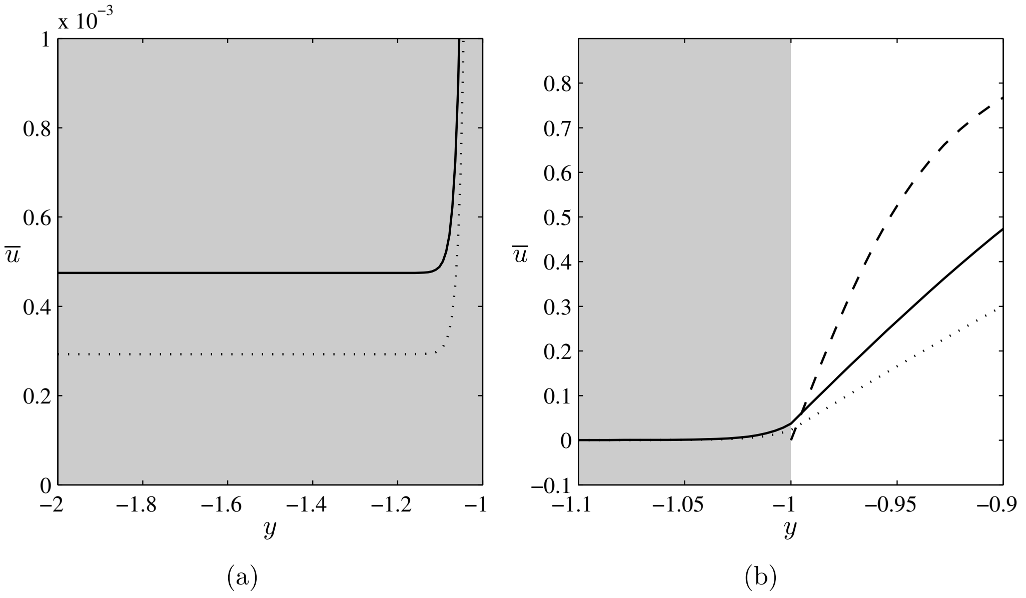

(a) (b)

FIGURE 5.14: Zoomed views of the mean velocity profile in the porous layer (a) and at the interface with the fluid region (b). The half-heights of the porous layers are $h_p = 1$, the permeability is $\sigma = 0.01$, the porosity is $\varepsilon = 0.6$. The solid and dotted lines are the turbulent and laminar velocity profiles of the flow at Re = 950, while the dashed line is the velocity profile of a channel flow over impermeable walls at Re = 3100.

Reynolds number. The other two components of the mean velocity, $\overline{v}$ and $\overline{w}$, are equal to zero, as in the case at Re = 3100 discussed in section 5.1. We can observe that, in the fluid region, the two profiles are quite different, especially at the centerline where the turbulent profile has a lower maximum velocity $\overline{u}_c = 1.25$ than the laminar case where $U_c = 1.49$. Figure 5.13(b) shows the same velocity profiles and also a mean velocity profile of a turbulent channel flow over impermeable walls at Re = 3100, drawn with a dashed line. We notice that, all three profiles are significantly different. In the inset figure in figure 5.13(b), we show the mean velocity profiles at the interface. Turbulence, apparently, increases the velocity at the interface. In the laminar solution the interface velocity is

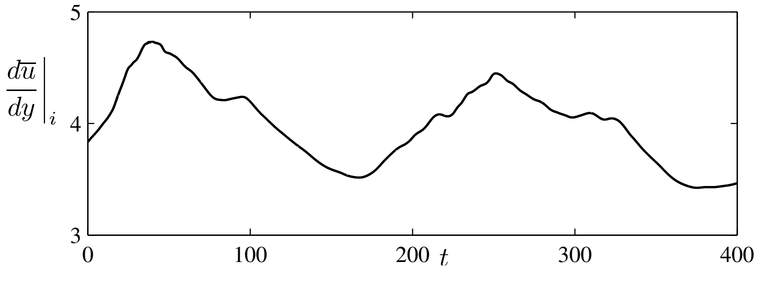

FIGURE 5.15: Time history of the y-derivative of the mean velocity profile $\overline{u}$.

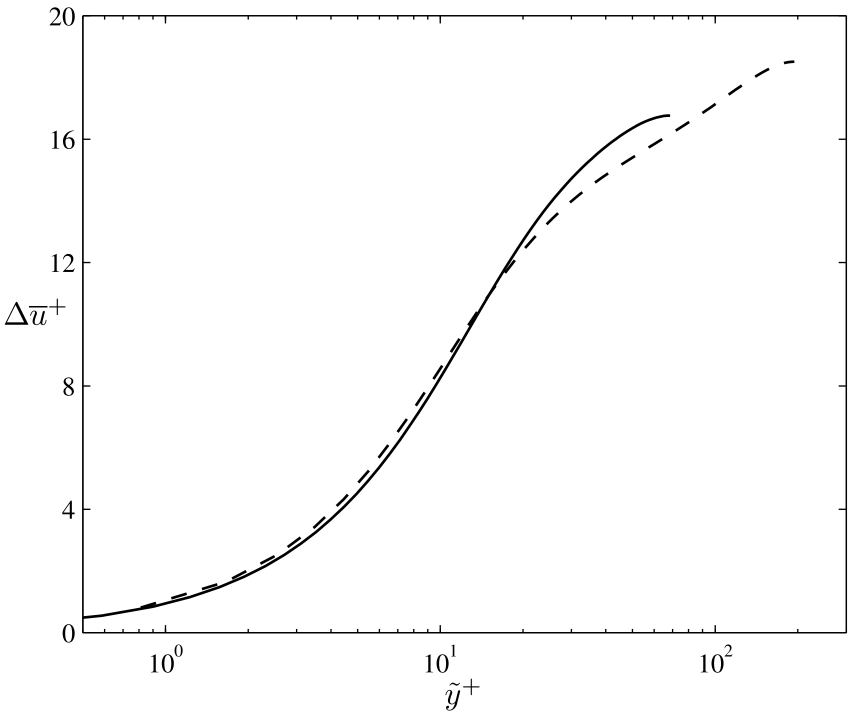

FIGURE 5.16: Mean velocity profiles of turbulent channel flow made dimensionless with the friction velocity. The solid line is the velocity profile of a turbulent flow over porous wall at Re = 950, while the dashed line is the velocity profile of a turbulent channel flow over impermeable walls at Re = 3100.

$U_i = 0.0230$, while in the turbulent simulation the mean value is $\overline{u}_i = 0.0381$.

In figure 5.14(a) we show the velocity profile inside the porous layer. As already noticed, the velocity at the interface is clearly not zero. Moreover, the Darcy velocity $\overline{u}_D$, in the turbulent case, is greater than the laminar one, changing from 0.000293 in the laminar case to 0.000475 in the turbulent case. This increase is caused by the fact that we are running simulations at constant flow rate. In fact, the pressure gradient needed to maintain the flow rate constant is different in the laminar and turbulent cases, and is generally greater in the turbulent case. We also notice that the Brinkman layer is slightly thicker in the turbulent case, passing from 0.0458 (laminar) to 0.0517 (turbulent). This becomes clearer when we look at the interface region between the porous layer and the fluid region, figure 5.14(b). At the interface with the fluid region, the value of the y-derivative of the velocity profile passes from 2.93 in the laminar case to 4.84 in the turbulent case. Figure 5.15 shows the time fluctuations of the y-derivative of the mean velocity profile. The increase in the y-derivative reflects in the increase of the friction velocity u_τ, which increases from 0.0555 (laminar) to 0.0722 (turbulent).

Figure 5.16 shows the mean velocity profiles corrected by a factor $\overline{u}_i^+$, $\Delta\overline{u}^+ = \overline{u}^+ - \overline{u}_i^+$, versus the logarithm of the distance from the interface $\tilde{y} = y - 1$ expressed

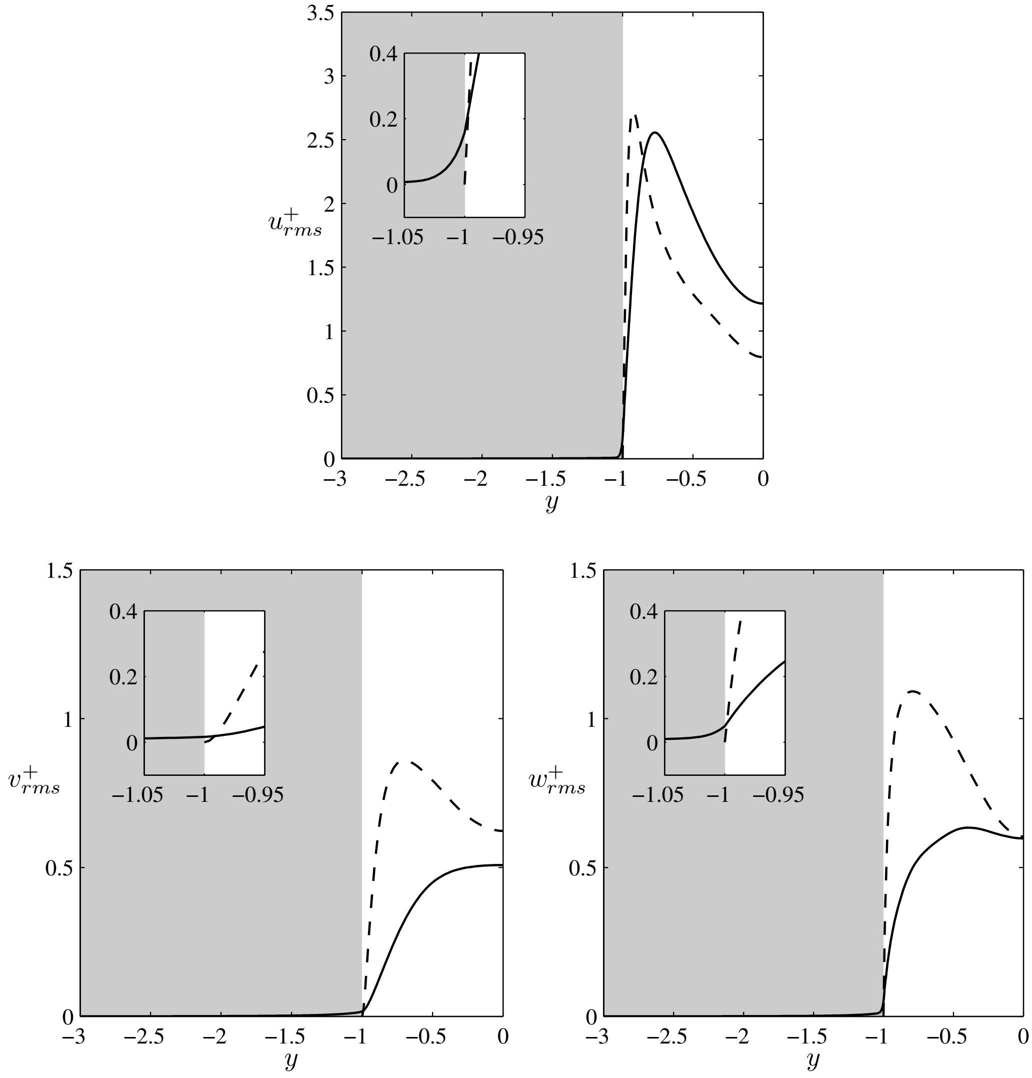

FIGURE 5.17: Rms velocities made dimensionless with the friction velocity. The solid and dashed line are used for the flow over porous and impermeable walls, respectively. For the flow over porous layers, the half-heights of the porous layers are $h_p = 1$, the permeability is $\sigma = 0.01$, the porosity is $\varepsilon = 0.6$.

in wall-units. In this figure is also plotted with a dashed line the curve for the channel flow over impermeable walls at Re = 3100. We note that the viscous layer ($\tilde{y}^+ < 5$) is still present in the case at Reynolds number 950. However, at Re = 950, the mean velocity distribution does not have a clear logarithmic region ($\tilde{y}^+ > 30$).

We continue the analysis of the turbulent channel flows with porous walls at low Reynolds number by analyzing the turbulence intensities. Figure 5.17 shows the rms velocities of the flow at Re = 950, compared with the ones of a turbulent

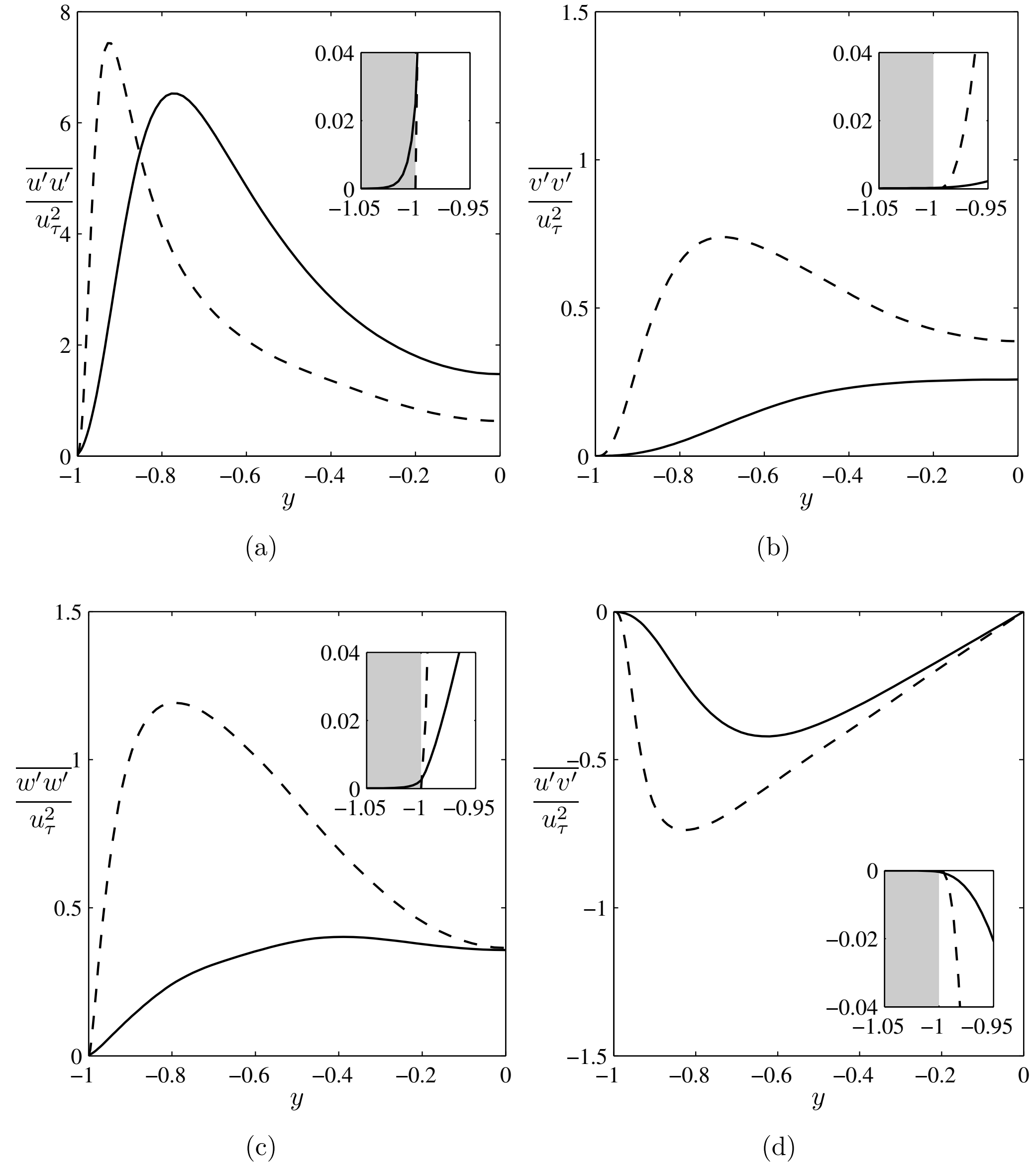

(a) (b)

(c) (d)

FIGURE 5.18: Reynolds stresses. The solid line is used for the flow over porous walls at Re = 950, while the dashed line is used for the flow over impermeable walls at Re = 3100. For the flow over porous layers, the half-heights of the porous layers are $h_p = 1$, the permeability is $\sigma = 0.01$, the porosity is $\varepsilon = 0.6$.

channel flow over impermeable walls at Re = 3100. We observe that the rms velocities at Re = 950 are smaller than in the case at Re = 3100. In particular, the wall-normal v^+_{rms} and the spanwise w^+_{rms} rms velocities, reach their maximum near the centerline, while the streamwise rms velocity u^+_{rms} has a peak near the interface, which is shifted towards the centerline in comparison to the Re = 3100

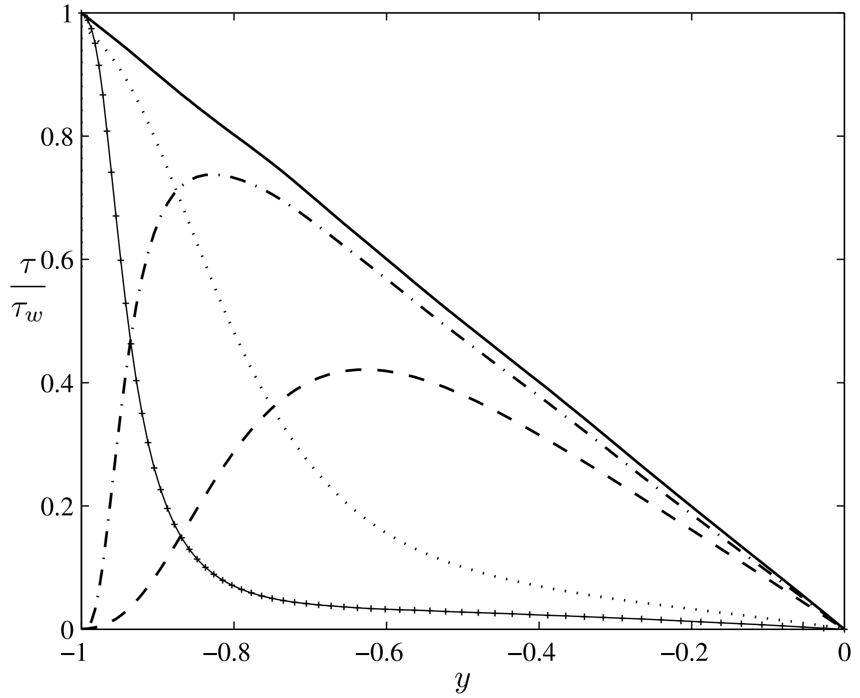

FIGURE 5.19: The solid line represents the total shear stress, decomposed in the viscous stress and in the Reynolds shear stress. The dashed and dotted lines represent the shear and viscous stresses for the porous case, respectively, while the dash-dotted and crossed lines represent the shear and viscous stresses, respectively, for the case with solid walls.

case.

Figure 5.18 shows the Reynolds stresses of the turbulent channel flow over porous walls at Re = 950, made dimensionless with the friction velocity. We note that the Reynolds stresses are very different from the ones at at Re = 3100 with impermeable walls. All the Reynolds stresses at Re = 950 are smaller and the peak values are shifted towards the centerline than in the case at Re = 3100. The wall-normal $\overline{v'v'}$ and spanwise $\overline{w'w'}$ Reynolds stresses seems to be the most affected at at Re = 950, while the streamwise normal stress $\overline{u'u'}$ seems to be less sensitive. However, we notice that at the centerline, the normal Reynolds stress $\overline{u'u'}$ at Re = 950 are twice as big as at Re = 3100. Contrary to the case at at Re = 3100, the wall-normal Reynolds stress at Re = 950 is lower and reaches the maximum value at the centerline. The spanwise and shear Reynolds stresses at Re = 950 are everywhere smaller than the case at Re = 3100, but at the centerline where they are nearly the same. The decomposition of the total shear stress in the Reynolds shear stress and in the viscous stress is shown in figure 5.19. With respect to the channel flow over impermeable walls at Re = 3100, we note that at Re = 950 the Reynolds shear stress is always smaller, but it is

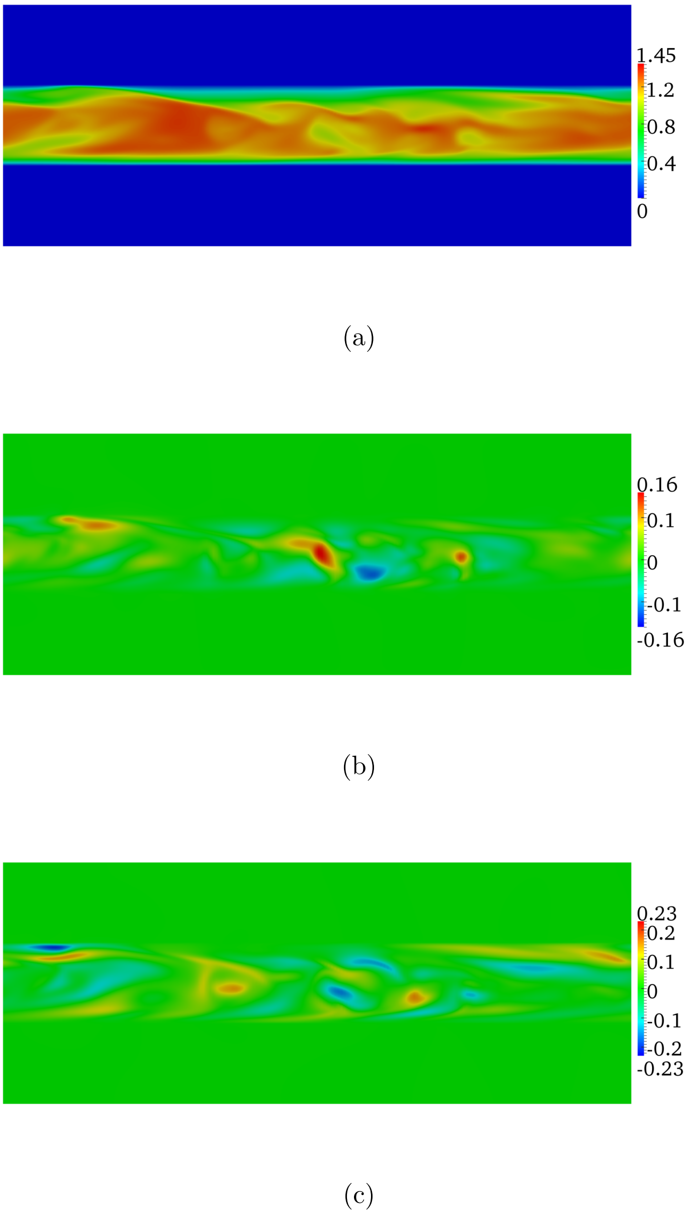

FIGURE 5.20: Slice in the x-y plane of the computational domain. The three velocity components u, v and w are shown in subfigures (a), (b) and (c), respectively.

compensated by the overall increase in the viscous stress.

We now show some flow visualization of the turbulent channel flow over porous walls at $\mathrm{Re} = 950$. Figures 5.20(a)-5.20(c) show the three velocity components u, v and w on a slice in the x-y plane, respectively. The maximum of the streamwise velocity u is located at around the centerline, and u becomes very small at the interface with the porous layers. The other two velocity components v and

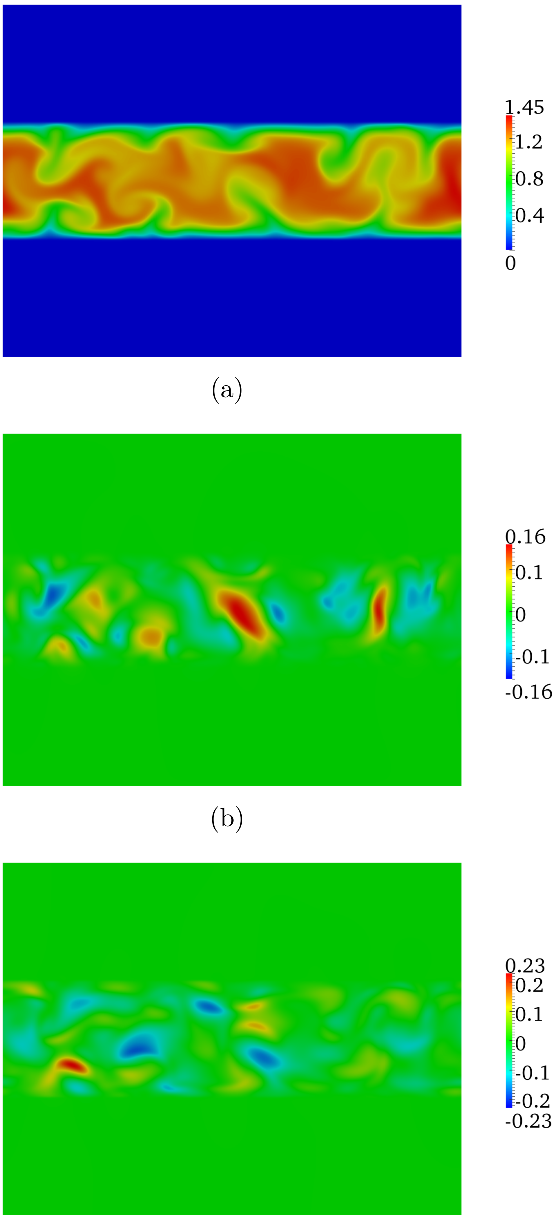

(a)

(b)

(c)

FIGURE 5.21: Slice in the y-z plane of the computational domain. The three velocity components u, v and w are shown in subfigures (a), (b) and (c), respectively.

w are also greater in absolute value near the centerline, and very small in the porous layers. However, there are some intermittent strong fluctuations at small distances from the interface with the porous layers. Figures 5.21(a)-5.21(c) show the three velocity components u, v and w on a slice in the y-z plane, respectively. We note that streamwise velocity u seems to show an alternance of low-speed and high-speed streaks near the porous walls. Correspondently, the maximum

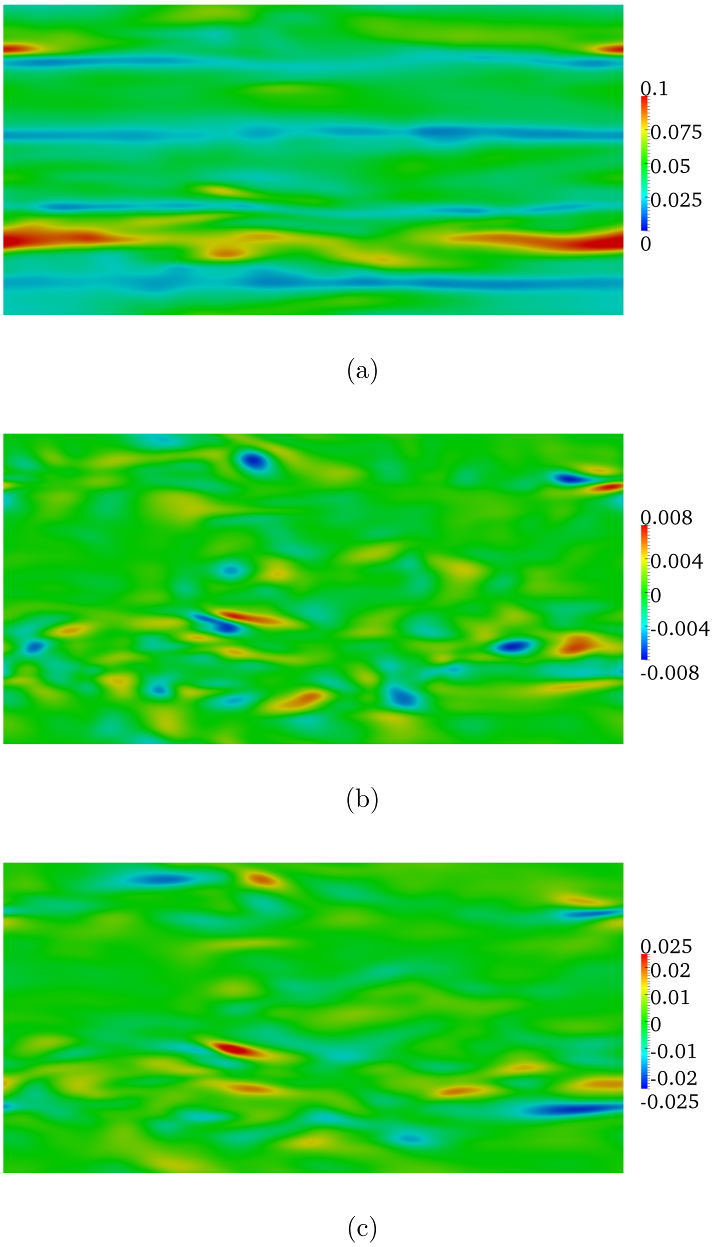

(a)

(b)

(c)

FIGURE 5.22: Slice in the x-z plane of the computational domain at the interface with the porous layer. The three velocity components u, v and w are shown in subfigures (a), (b) and (c), respectively.

wall-normal and spanwise velocity are reached between the streaks. To better visualize the streaks, we cut the computational domain in the x-z plane, at an appropriate distance from the interface with the porous layer. Figure 5.22(a) clearly shows an alternance of streak lines at high and low speed. Note that around these streaks, the other two velocity components, v and w, have their

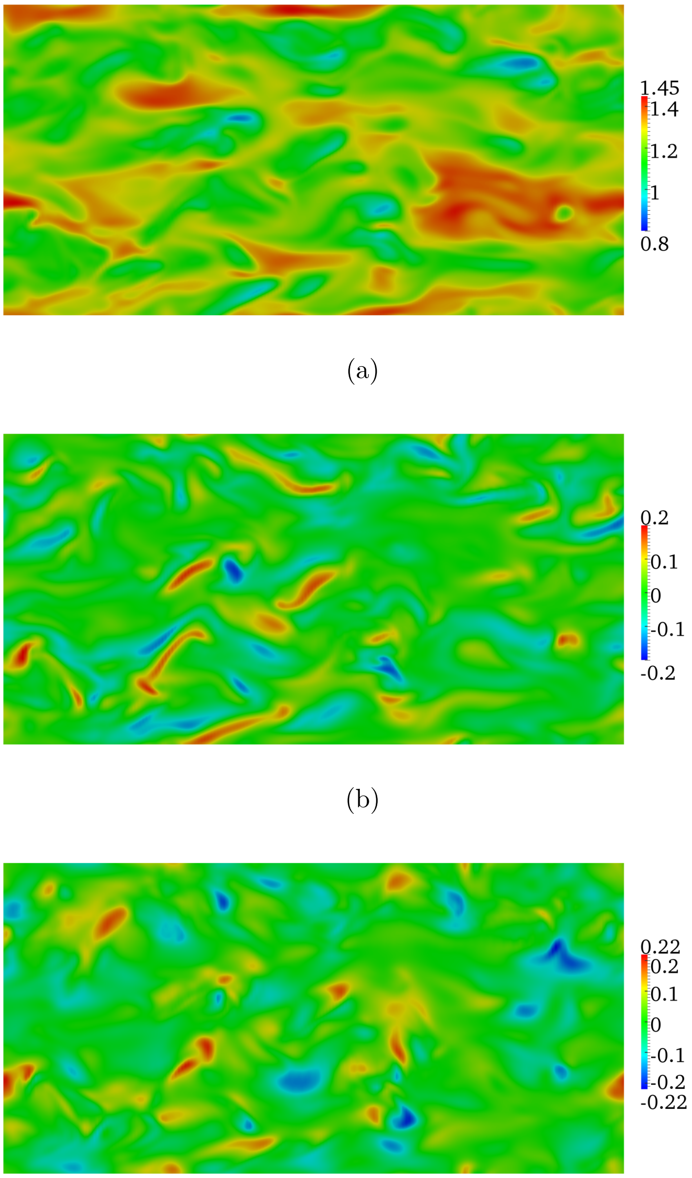

(a)

(b)

(c)

FIGURE 5.23: Slice in the x-z plane of the computational domain at the centerline. The three velocity components u, v and w are shown in subfigures (a), (b) and (c), respectively.

largest fluctuations, as shown in figures 5.22(b) and 5.22(c). At the centerline, as shown in figure 5.23, we notice strong fluctuations in all the velocity components.

Although the concept of a vortex is an essential tool in the comprehension of turbulent flows, it is still very difficult to find a universal definition for a vortex [16]. In this thesis, we use the definition of vortex given by Jeong and Hussain

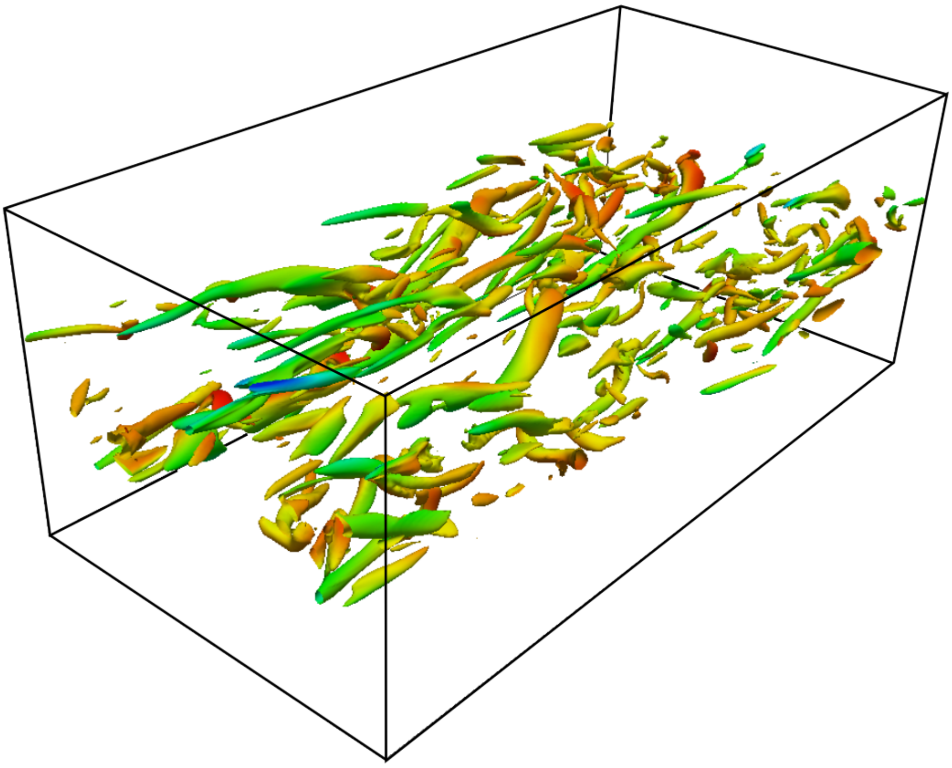

FIGURE 5.24: Isosurfaces of $\lambda_2 = -0.25$ in the computational domain, coloured with the magnitude of velocity.

[17], the so-called λ_2 criterion. The velocity gradient $\boldsymbol{\nabla} u$ is decomposed as follows

$$\boldsymbol{\nabla} u = \boldsymbol{S} + \boldsymbol{\Omega}, \tag{5.9}$$

where $\boldsymbol{S}$ is the rate of strain tensor $\boldsymbol{S} = 1/2 \left[\boldsymbol{\nabla} u + (\boldsymbol{\nabla} u)^T\right]$ and $\boldsymbol{\Omega}$ is the vorticity tensor $\boldsymbol{\Omega} = 1/2 \left[\boldsymbol{\nabla} u - (\boldsymbol{\nabla} u)^T\right]$. $\boldsymbol{S}$ and $\boldsymbol{\Omega}$ are the symmetric and anti-symmetric parts of the velocity gradient tensor, respectively. According to the λ_2 criterion, vortices are regions where

$$\lambda_2 \left(\boldsymbol{S}^2 + \boldsymbol{\Omega}^2\right) < 0, \tag{5.10}$$

where λ_2 represents the intermediate eigenvalue. In figure 5.24 we show the isosurfaces of $\lambda_2 = -0.25$.

Chapter 6

Conclusions and future work

In this thesis we have presented some results from DNSs of turbulent channel flows over porous walls. We have solved the flow inside the porous layers with the Volume-Averaging Naviers-Stokes equations, and the flow inside the fluid region with the Navier-Stokes equations. We have coupled the flow in the porous layer with the flow in the fluid region with the momentum transfer conditions. We have analyzed two cases, at different Reynolds numbers: moderate, $\mathrm{Re}_\tau = 200$, and very low, $\mathrm{Re}_\tau = 65$.

The simulations at $\mathrm{Re}_\tau = 200$ showed that the porous walls modify all the turbulence statistics of the flow. In particular, the mean velocity profile is modified by the presence of a slip velocity at the interface between the porous layer and the fluid region, and by the increase of the friction velocity. The rms velocities and the Reynolds stresses are also modified, especially near the interface. The components in the wall-normal and spanwise directions are magnified, while the streamwise component is reduced, with respect to the ones of a turbulent channel flows over impermeable walls. We observed that all the components of the rms velocities and the Reynolds stresses are non-zero at the interface between the porous layers and the fluid region. A parametric study showed that the height of the porous layers has only small effects on the statistics of the turbulent flow. However, the coefficient τ of the momentum transfer conditions have great impact on the turbulent flow. A positive τ increases substantially the slip velocity of the mean velocity profile, and reduces the wall-normal and spanwise fluctuations. On the contrary, a negative τ has less impact, it slightly decreases the slip velocity of the mean velocity profile, and increases the wall-normal and spanwise fluctuations.

We have been able to perform a turbulent simulation at $\mathrm{Re}_\tau = 65$, discovering that the porous walls can sustain turbulent flows even at low Reynolds number. At this Reynolds number, the mean velocity profile does not present the expected logarithmic region, showing that the log-law apparently has a significant Reynolds number dependence at low/very-low Reynolds numbers. Also the rms velocities and the Reynolds stresses show great differences with respect to the ones of a turbulent channel flows over impermeable walls at higher Reynolds numbers, especially for the components in the wall-normal and spanwise directions. Moreover, the Reynolds shear stress is strongly reduced, while the viscous stress is enhanced, with respect to the case with impermeable walls.

This study considered a turbulent flow over porous walls with small wall permeability, and showed that the wall porosity modifies the turbulence statistics. These results could have profound implications on the research devoted to flow control using wall transpiration. In fact, the model of the porous media may be considered as a first step towards a more realistic model of a wall transpiration actuator. The latter are used to inhibit transition to turbulence, such as in the asymptotic suction boundary layer (ASBL). In experiments, suction has been implemented using spanwise slots, discrete holes, and wholly porous materials. The application of suction through discrete holes have the advantage that a skin with discrete holes can continue to act as a continuous structural member, however, the discrete holes generally lead to three-dimensional effects which can provoke early transition. Recent experimental studies used wholly porous materials, because they can provide a uniform suction velocity without provoking three-dimensional effects, and can be cheaply manufactured.

After our turbulent simulation at very low Reynolds number, future works should better study the turbulent flows at very low Reynolds numbers, in order to investigate the mechanisms that are able to sustain the turbulent flow. Moreover, future works should verify the existence of low Reynolds numbers flow which fluctuates between a turbulent and laminar regimes.

The volume-averaged equations used to solve the flow in the porous layer, and the momentum transfer conditions used to couple the flow in the fluid region and in the porous layers, were simplified by neglecting inertial effects. These assumptions are valid only when the slip velocity at the solid walls is small. When inertial effects are not important in the porous regions, the momentum equation does not contain the Forchheimer drag term. While the Forchheimer drag may be negligible in the porous regions, inertial effects may still be important near the interfaces. Moreover, the assumption of neglecting the inertial effects at the interface limits strongly the amount of permeability of the porous wall. So, a possible development of this work is to modify the momentum transfer conditions in order to include the inertial effects at the interface between the porous layer and the fluid region.

Bibliography

[1] B. Alazmi and K. Vafai. Analysis of fluid flow and heat transfer interfacial conditions between a porous medium and a fluid layer. *International Journal of Heat and Mass Transfer*, 44(9):1735–1749, 2001.

[2] J. Bear. *Dynamics of fluids in porous media.* Dover publications, 1988.

[3] G.S. Beavers and D.D. Joseph. Boundary conditions at a naturally permeable wall. *J. Fluid Mech*, 30(1):197–207, 1967.

[4] G.S. Beavers, E.M. Sparrow, and R.A. Magnuson. Experiments on coupled parallel flows in a channel and a bounding porous medium. *Journal of Basic Engineering*, 92:843, 1970.

[5] GS Beavers, EM Sparrow, and DE Rodenz. Influence of bed size on the flow characteristics and porosity of randomly packed beds of spheres. *Journal of Applied Mechanics*, 40:655, 1973.

[6] W. P. Breugem. *The influence of wall permeability on laminar and turbulent flows.* PhD thesis, Delft University of Technology, 2005.

[7] WP Breugem and BJ Boersma. Direct numerical simulations of turbulent flow over a permeable wall using a direct and a continuum approach. *Physics of fluids*, 17:025103, 2005.

[8] WP Breugem, BJ Boersma, and RE Uittenbogaard. The laminar boundary layer over a permeable wall. *Transport in porous media*, 59(3):267–300, 2005.

[9] WP Breugem, BJ Boersma, and RE Uittenbogaard. The influence of wall permeability on turbulent channel flow. *Journal of Fluid Mechanics*, 562(1):35–72, 2006.

[10] X. Chen, P. Yu, SH Winoto, and H.T. Low. A numerical method for forced convection in porous and homogeneous fluid domains coupled at interface by stress jump. *International journal for numerical methods in fluids*, 56(9):1705–1729, 2008.

[11] VAF Costa, LA Oliveira, and BR Baliga. Implementation of the stress jump condition in a control-volume finite-element method for the simulation of laminar coupled flows in adjacent open and porous domains. *Numerical Heat Transfer, Part B: Fundamentals*, 53(5):383–411, 2008.

[12] H. Darcy. Les fontaines publiques de la ville de dijon, 1856. *Dalmont, Paris*, 70.

[13] K Djidjeli, WG Price, P Temarel, and EH Twizell. Partially implicit schemes for the numerical solutions of some non-linear differential equations. *Applied mathematics and computation*, 96(2):177–207, 1998.

[14] T. Giorgi. Derivation of the forchheimer law via matched asymptotic expansions. *Transport in porous media*, 29(2):191–206, 1997.

[15] Seonghyeon Hahn, Jongdoo Je, and Haecheon Choi. Direct numerical simulation of turbulent channel flow with permeable walls. *Journal of Fluid Mechanics*, 450:259–286, 2002.

[16] George Haller. An objective definition of a vortex. *Journal of Fluid Mechanics*, 525(1):1–26, 2005.

[17] Jinhee Jeong and Fazle Hussain. On the identification of a vortex. *Journal of Fluid Mechanics*, 285(69):69–94, 1995.

[18] DD Joseph, DA Nield, and G. Papanicolaou. *Nonlinear equation governing flow in a saturated porous medium.* Defense Technical Information Center, 1981.

[19] J. Kim, P. Moin, and R. Moser. Turbulence statistics in fully developed channel flow at low reynolds number. *Journal of Fluid Mechanics*, 177(1):133–166, 1987.

[20] AV Kuznetsov. Analytical investigation of the fluid flow in the interface region between a porous medium and a clear fluid in channels partially filled with a porous medium. *Applied scientific research*, 56(1):53–67, 1996.

[21] JL Lage. The fundamental theory of flow through permeable media from darcy to turbulence. *Transport phenomena in porous media*, pages 1–30, 1998.

[22] Sanjiva K Lele. Compact finite difference schemes with spectral-like resolution. *Journal of Computational Physics*, 103(1):16–42, 1992.

[23] M. Lesieur and O. Metais. New trends in large-eddy simulations of turbulence. *Annual Review of Fluid Mechanics*, 28(1):45–82, 1996.

[24] F. Liu, BM Chen, and L. Wang. Experimental and numerical estimation of slip coefficient in a partially porous cavity. *Experimental Thermal and Fluid Science*, 2012.

[25] Qianlong Liu and Andrea Prosperetti. Pressure-driven flow in a channel with porous walls. *Journal of Fluid Mechanics*, 679(1):77–100, 2011.

[26] Paolo Luchini and Maurizio Quadrio. A low-cost parallel implementation of direct numerical simulation of wall turbulence. *Journal of Computational Physics*, 211(2):551–571, 2006.

[27] Krishnan Mahesh. A family of high order finite difference schemes with good spectral resolution. *Journal of Computational Physics*, 145(1):332–358, 1998.

[28] P. Moin and K. Mahesh. Direct numerical simulation: a tool in turbulence research. *Annual Review of Fluid Mechanics*, 30(1):539–578, 1998.

[29] R.D. Moser, J. Kim, and N.N. Mansour. Direct numerical simulation of turbulent channel flow up to re= 590. *Physics of fluids*, 11:943, 1999.

[30] G. Neale and W. Nader. Practical significance of brinkman's extension of darcy's law: coupled parallel flows within a channel and a bounding porous medium. *The Canadian Journal of Chemical Engineering*, 52(4):475–478, 1974.

[31] J.A. Ochoa-Tapia and S. Whitaker. Momentum transfer at the boundary between a porous medium and a homogeneous fluid—i. theoretical development. *International Journal of Heat and Mass Transfer*, 38(14):2635–2646, 1995.

[32] J.A. Ochoa-Tapia and S. Whitaker. Momentum transfer at the boundary between a porous medium and a homogeneous fluid—ii. comparison with experiment. *International Journal of Heat and Mass Transfer*, 38(14):2647–2655, 1995.

[33] JA Ochoa-Tapia and S. Whitaker. Momentum jump condition at the boundary between a porous medium and a homogeneous fluid: inertial effects. *Journal of Porous Media*, 1:201–218, 1998.

[34] Davide Pirro and Maurizio Quadrio. Direct numerical simulation of turbulent taylor–couette flow. *European Journal of Mechanics-B/Fluids*, 27(5):552–566, 2008.

[35] Stephen B Pope. *Turbulent flows*. Cambridge university press, 2000.

[36] Maurizio Quadrio and Paolo Luchini. Direct numerical simulation of the turbulent flow in a pipe with annular cross section. *European Journal of Mechanics-B/Fluids*, 21(4):413–427, 2002.

[37] M. Quintard and S. Whitaker. Transport in ordered and disordered porous media i: The cellular average and the use of weighting functions. *Transport in Porous Media*, 14(2):163–177, 1994.

[38] M. Quintard and S. Whitaker. Transport in ordered and disordered porous media ii: Generalized volume averaging. *Transport in porous media*, 14(2):179–206, 1994.

[39] S. Richardson. A model for the boundary condition of a porous material. part 2. *J. Fluid Mech*, 49(2):327–336, 1971.

[40] P.G. Saffman. On the boundary condition at the surface of a porous medium. *Stud. Appl. Math*, 50(2):93–101, 1971.

[41] D. Scarselli. Non-modal stability of laminar channel flows over porous walls, 2013.

[42] U. Shavit, R. Rosenzweig, and S. Assouline. Free flow at the interface of porous surfaces: a generalization of the taylor brush configuration. *Transport in porous media*, 54(3):345–360, 2004.

[43] J.C. Slattery. *Momentum, energy, and mass transfer in continua*. RE Krieger Publishing Company, 1978.

[44] Philippe R Spalart, Robert D Moser, and Michael M Rogers. Spectral methods for the navier-stokes equations with one infinite and two periodic directions. *Journal of Computational Physics*, 96(2):297–324, 1991.

[45] H. Tan and K.M. Pillai. Finite element implementation of stress-jump and stress-continuity conditions at porous-medium, clear-fluid interface. *Computers & Fluids*, 38(6):1118–1131, 2009.

[46] GI Taylor. A model for the boundary condition of a porous material. part 1. *Journal of Fluid Mechanics*, 49(02):319–326, 1971.

[47] LH Thomas. The stability of plane poiseuille flow. *Physical Review*, 91(4):780, 1953.

[48] N. Tilton. *The Effects of Wall Permeability on the Linear Stability of Channel Flows and the Asymptotic Suction Boundary Layer*. PhD thesis, McGill University, 2009.

[49] N. Tilton and L. Cortelezzi. The destabilizing effects of wall permeability in channel flows: A linear stability analysis. *Physics of Fluids*, 18(5):051702–051702, 2006.

[50] N. Tilton and L. Cortelezzi. Linear stability analysis of pressure-driven flows in channels with porous walls. *Journal of Fluid Mechanics*, 604:411–446, 2008.

[51] Takahiro Tsukahara, Yohji Seki, Hiroshi Kawamura, and Daisuke Tochio. Dns of turbulent channel flow at very low reynolds numbers. In *Proc. 4th Intl Symp. on Turbulence and Shear Flow Phenomena*, pages 935–940, 2005.

[52] F.J. Valdés-Parada, B. Goyeau, and J.A. Ochoa-Tapia. Jump momentum boundary condition at a fluid–porous dividing surface: Derivation of the closure problem. *Chemical engineering science*, 62(15):4025–4039, 2007.

[53] Claus Wagner and Rainer Friedrich. Dns of turbulent flow along passively permeable walls. *International journal of heat and fluid flow*, 21(5):489–498, 2000.

[54] S. Whitaker. Advances in theory of fluid motion in porous media. *Industrial & Engineering Chemistry*, 61(12):14–28, 1969.

[55] S. Whitaker. Flow in porous media i: A theoretical derivation of darcy's law. *Transport in porous media*, 1(1):3–25, 1986.

[56] S. Whitaker. The forchheimer equation: a theoretical development. *Transport in Porous media*, 25(1):27–61, 1996.

[57] D.C. Wilcox. *Turbulence modeling for CFD*, volume 3. DCW industries La Cañada, CA, 2006.

[58] P. Yu, TS Lee, Y. Zeng, and HT Low. A numerical method for flows in porous and homogenous fluid domains coupled at the interface by stress jump. *International journal for numerical methods in fluids*, 53(11):1755–1775, 2007.

[59] Quan Zhang and Andrea Prosperetti. Pressure-driven flow in a two-dimensional channel with porous walls. *Journal of Fluid Mechanics*, 631:1, 2009.